Copper-Ion Based Electron Spin Resonance Sheds light on Protein-DNA Interaction

by

Ming Ji

B.S., Nanjing University, CHINA, 2003

M.S., Nanjing University, CHINA, 2006

Submitted to the Graduate Faculty of the Kenneth P. Dietrich

School of Arts and Sciences in partial fulfillment

of the requirements for the degree of

Doctor of Philosophy

University of Pittsburgh

2013

UNIVERSITY OF PITTSBURGH

DIETRICH OF ARTS AND SCIENCES

This dissertation was presented

by

Ming Ji

It was defended on

December 13, 2013

and approved by

David Waldeck, Ph.D., Professor, Department of Chemistry, Faculty of Arts and Sciences

Steve Weber, Ph.D., Professor, Department of Chemistry, Faculty of Arts and Sciences

Pei Tang, Ph.D., Professor, Department of Anesthesiology, Faculty of Arts and Sciences

Dissertation Advisor: Sunil Saxena, Ph.D., Professor, Department of Chemistry, Faculty of Arts and Sciences

Copper-Ion Based Electron Spin Resonance Sheds light on Protein-DNA Interaction

Ming Ji, Ph.D.

University of Pittsburgh, 2013

This thesis focuses on Cu^{2+}-based electron spin resonance (ESR) spectroscopy and its application in biophysics. First, we review the use of paramagnetic metal ions like Cu^{2+}, to measure distance constraints in protein by double electron electron resonance (DEER) spectroscopy. Although lower sensitivity and orientational selectivity complicate data collection and analysis, the simple sample preparation process and limited spatial flexibility makes Cu^{2+} an attractive probe.

We then use Cu^{2+} as spin probe to develop insights into the molecular determinants of catalysis in type II restriction endonuclease EcoRI. We show that Cu^{2+} does not catalyze the DNA cleavage by EcoRI. More strikingly, it inhibits the Mg^{2+}-dependent DNA cleavage. We perform X-band (~9.5 GHz) ESR spectroscopy as well as biochemical studies to understand the functional difference between Cu^{2+} and Mg^{2+}. These results reveal a hitherto unknown metal ion binding site. Molecular dynamics (MD) simulations reveal that the Cu^{2+}-H114 coordination disrupts a critical protein-DNA interaction, which is essential for catalysis. This structural change may lead to inhibition of Mg^{2+}-dependent cleavage. We also propose an electrostatic basis for the positive cooperativity of Mg^{2+} binding to the EcoRI-DNA complex. Such cooperativity helps EcoRI inactivate DNA by double-strand cuts instead of single-strand nicks.

Next, we use W-band (~95 GHz) ENDOR as well as X-band electron spin echo envelope modulation (ESEEM) spectroscopy to further refine the Cu^{2+} coordination environment in the EcoRI-DNA complex. The existence of equatorially coordinated water molecules is confirmed by the ENDOR results. Simulations of the X-band ESEEM spectra at different magnetic fields

indicate that the Cu^{2+}-H114 coordination is similar in the two Cu^{2+} sites. However, the relative orientation between the histidine imidazole ring and the Cu^{2+} center is possibly different.

Lastly, we apply Double Quantum Coherence (DQC) spectroscopy to measure the Cu^{2+}-Cu^{2+} distance in the EcoRI-DNA complex. The DQC signal has contributions from nuclear hyperfine and quadrupole interactions. The effect of such interactions swamps the modulation due to the electron-electron dipolar interactions and makes it difficult to measure the interspin distance. We show a simple method to reduce these electron-nuclei interactions and resolve the dipolar interaction between two Cu^{2+} centers with high sensitivity.

TABLE OF CONTENTS

LIST OF TABLES

LIST OF FIGURES

$K_{A,Cu^{2+}}$ (max) = 9.3(± 0.3)×10^9 M^{-1}. For the promiscuous H114Y that shows better binding affinity than wild type EcoRI [140], $K_{A,0}$ = 1.7 (± 0.1)×10^{10} M^{-1} and $K_{A,\ Cu^{2+}}$(max) = 7.3(± 2.1)×10^{10} M^{-1}. Fit to the Hill equation $K_{A,\ Cu^{2+}} = K_{A,\ Cu^{2+}\ (max)}\ [Cu^{2+}]^n\ /(K_{D\ 0.5,\ Cu^{2+}} + [Cu^{2+}]^n)$ gives Hill coefficient n = 1.0 ± 0.15 and $K_{D\ 0.5,\ Cu^{2+}}$ = 5.1 ± 0.8 μM. Inset shows the hyperbolic binding isotherm of wild type EcoRI for [Cu^{2+}] from 0 to 100 μM. (b) Representative ITC titration of $CuCl_2$ (1 mM) into sample cell (15°C) containing EcoRI (9 μM) and DNA (20 μM). Top panel shows heat signals obtained for 125 injections (2.5 μL each). Lower panel shows integrated heat signal normalized to moles of Cu^{2+} injected (after subtraction of heats of dilution of Cu^{2+}) per mole of EcoRI–DNA complex. The stoichiometry value n = 2.0 ± 0.3 and K_D value of 14 ± 6 μM (means ± std. dev. of at least 3 determinations at 10°C, 15°C, 21°C) did not vary with temperature or buffer identity (imidazole or TRIS; see Methods for buffer compositions). 65

PREFACE

First of all, I really appreciate my supervisor, Professor Sunil Saxena, for his patience, for being inspirational, and for teaching me the importance of using curiosity as the driving force behind research. It has been a great honor for me to work under his guidance.

I would like to thank my committees: Professor David Waldeck, Steve Weber, Pei Tang for being my dissertation committee. I am deeply grateful for their time and suggestions for my thesis. I want to thank Professor David Waldeck and Steve Weber for serving on my comprehensive exam committee. I am grateful to Professor Sean Garrett-Roe for being my proposal mentor. I thank Professor Steve Weber and Lillian Chong for being my proposal committee. Their time and advice were greatly appreciated.

I also want to thank my great collaborator Professor Linda Jen-Jacobson for her generous help and insightful advice. She was always willing to take time for adding new ideas to our project. I thank Dr. Preeti Mehta and Dr. Jacque Townsend from Professor Jen-Jacobson's group who provide the wonderful protein-DNA sample for our ESR experiments.

Also, it was a pleasure to work with Professor Daniel Lambrecht, Dr. Ozan Karalti and Eric Berquist. They helped me in the theoretical calculations of ESR parameters and simulations of spectra.

I would like to thank all my past and present group members, Dr. Soraya Pornsuwan, Dr. Katherine Stone, Dr. Sharon Ruthstein, Dr. Sangmi Jun, Dr. Zhongyu Yang, Dr. Byong-kyu Shin, Dr. Jessica Sarver, Gayathri Rajapackse, Marshall McGoff, Timothy Cunningham, Ishara Silva, and

Matthew Lawless for making me feel at home in US from time to time. I would especially like to thank Dr. Zhongyu Yang for all of his help in teaching me basic ESR theory and programming. It was a really pleasure to working with him on the EcoRI project. I also like to express my sincere gratitude to Dr. Jessica Sarver, who taught me a lot in the molecular dynamics simulations and committed her time to correct my English. I thank Dr. Sharon Ruthstein and Dr. Byong-kyu Shin for all of their patient help in trouble shooting my theoretical and experimental problems and teaching me basic ESR theory. I am also appreciative to Matthew Lawless, who spends a lot of time on correcting English in my thesis.

I would like to extend my gratitude to all my friends in Pittsburgh, who help me survive my foreign life in US. I want to thank the chemistry staff for all their help in making things easier for my research.

Finally I want to thank my family for their support. I want to thank them for always encouraging me when I had a hard time in my research during the past six years. I appreciate everything they did to help me finish my thesis.

1.0 INTRODUCTION

Electron Spin Resonance (ESR), also known as Electron Paramagnetic Resonance (EPR), has become an important biophysical tool to detect the structure and conformational dynamics of molecules as well as the coordination environments of paramagnetic metal ions in proteins.[1-15] One of the most important application of ESR spectroscopy involves the use of certain types of spin labels to correlate conformational motions in proteins with their functions. ESR spectroscopy has no limitation on the molecular size of analysis and does not require crystallization of samples. At the same time, the spin labels used in ESR are small and therefore only cause minimum perturbation.[6,16] In this thesis, we apply Cu^{2+} as a spin probe to measure protein structure and function by using different ESR techniques.

Specifically, in Chapter 2, we summarize the application of paramagnetic metal ions in pulsed ESR distance distribution measurements. In Chapter 3, we use continuous-wave (CW)-ESR and pulsed ESR methods, such as electron spin echo envelope modulation (ESEEM), hyperfine sublevel correlation spectroscopy (HYSCORE), double electron-electron resonance (DEER) and molecular dynamics (MD) simulations to identify the Cu^{2+} binding site and the determinants of chemical reactivity in the restriction endonucleases EcoRI-DNA complex. In Chapter 4, we apply high field ESR spectroscopy, electron nuclear double resonance (ENDOR) and ESEEM to clarify some details of the Cu^{2+} coordination environment in the EcoRI-DNA

complex. Furthermore, in Chapter 5, we develop a simple double quantum coherence (DQC) method to measure the Cu^{2+}-based nanoscale distances in proteins.

Since the focus of this thesis is the clarification of Cu^{2+}-coordination environment in a protein-DNA complex as well as the application of Cu^{2+} as spin probe in ESR spectroscopy at X-band (9.5 GHz) and W-band (94 GHz), the following sections provide a general overview of the Cu^{2+} complex in proteins, and the basic concepts of ESR techniques used in this thesis.

1.1 ESR INTERACTIONS IN A COPPER COMPLEX

There are three different types of Cu^{2+} sites in proteins, as shown in Figure 1-1. Figure 1-1a shows the structure of type I Cu^{2+} complex, which has three ligands coordinated to Cu^{2+} in a trigonal plane and another axially coordinated ligand Figure 1-1b shows the type II Cu^{2+} complex structure, which has four ligands equatorially bound to Cu^{2+}. In addition, there may exist up to two ligands, X5 and X6 as shown in Figure 1-1b, that axially coordinate to Cu^{2+} center. Figure 1-1c illustrates the structure of type III Cu^{2+} complex, which has binuclear centers consisting of two Cu^{2+} ions connected by a ligand X1. Each Cu^{2+} coordinates to three histidine residues. In proteins, atoms that bind to Cu^{2+} in these three types of complexes are generally nitrogen, oxygen, and sometimes sulfur. Considering the focus of this thesis, the following discussions are mainly based on the type II Cu^{2+} complex.

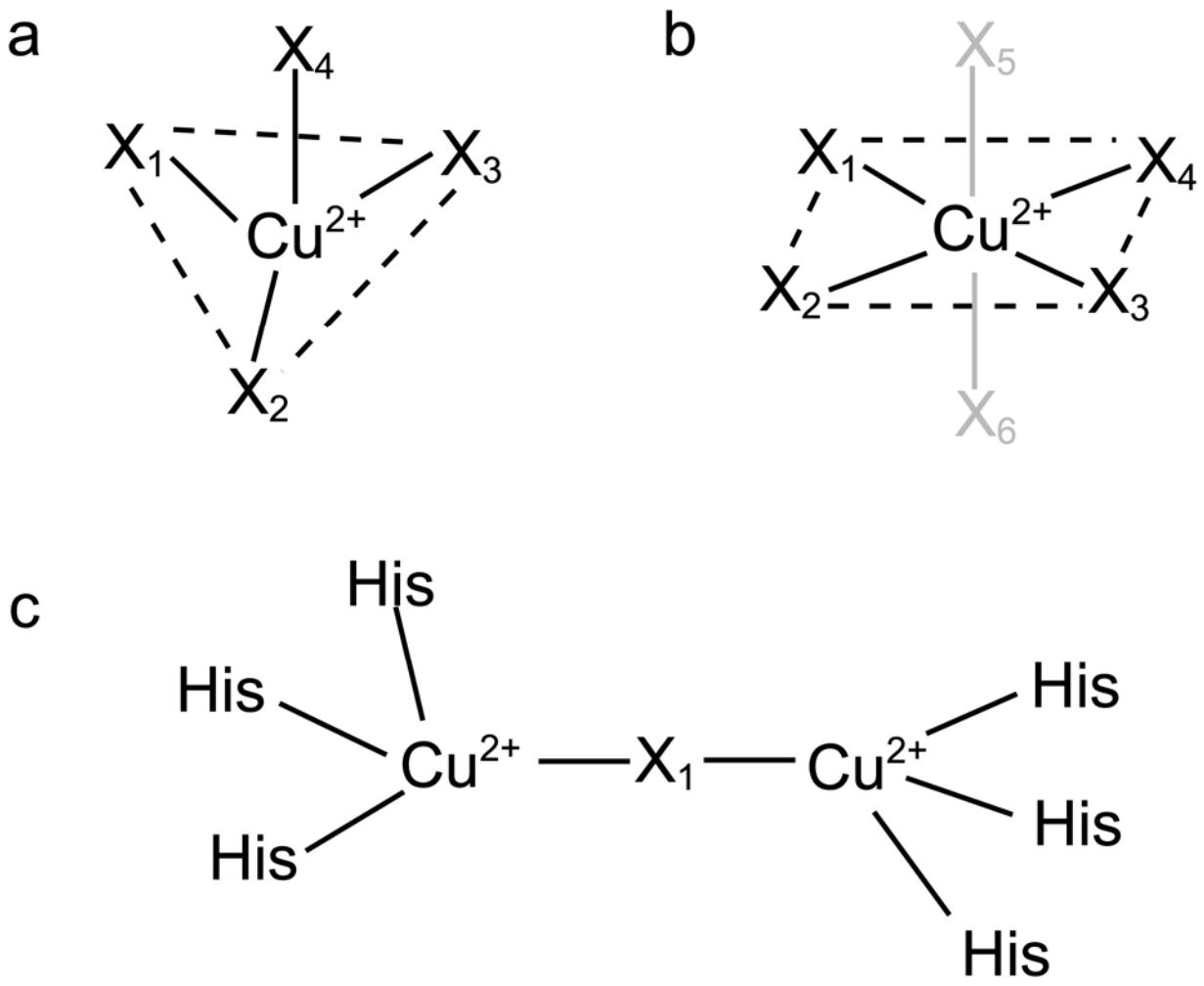

Figure 1-1. Three different types of Cu^{2+} complexes in proteins. (a) Type I Cu^{2+} complex; (b) Type II Cu^{2+} complex; (c) type II Cu^{2+} complex. X represents different ligands in the complex.

The electron spin of Cu^{2+} interacts with the magnetic field and the surrounding nuclear spins, such as the Cu^{2+} nucleus, ^{14}N and ^{1}H. The spin Hamiltonian is:

$$\begin{aligned}\hat{H} &= \hat{H}_{ez} + \hat{H}_{nz} + \hat{H}_{hf} + \hat{H}_{nq} \\ &= \beta_e \vec{B} \cdot \vec{\vec{g}} \cdot \vec{S} - \beta_n \sum_{i=1}^{k} \left(\vec{B} \cdot \vec{\vec{g}}_{in} \cdot \vec{I}_i \right) + \sum_{i=1}^{k} \vec{S} \cdot \vec{\vec{A}}_i \cdot \vec{I}_i + \sum_{i=1}^{k} \vec{I}_i \cdot \vec{\vec{Q}}_i \cdot \vec{I}_i \end{aligned} \tag{1-1}$$

The four terms in the equation are the electron Zeeman ($\hat{H}_{ez}$) interaction, the nuclear Zeeman interaction ($\hat{H}_{nz}$), the electron-nuclear hyperfine interaction ($\hat{H}_{hf}$) and the nuclear quadrupole interaction ($\hat{H}_{nq}$), respectively. In the equation, β_e is the Bohr magneton, β_n is the nuclear magneton, $\vec{B}$ is the external magnetic field, $\vec{\vec{g}}$ and $\vec{\vec{g}}_{in}$ are the *g*-tensor of electron spin and the *i*th nuclear spin, $\vec{\vec{A}}_i$ is the hyperfine tensor between electron spin and nuclear spin. $\vec{\vec{Q}}_i$ is the nuclear quadrupole interaction. The nuclear quadrupole interaction only exists when the nuclear spin > 1/2. $\vec{S}$ and $\vec{I}_i$ are the electron and nuclear spin angular momentum operators, respectively.

1.2 CW-ESR SPECTRUM OF COPPER ION AT LOW TEMPERATURE

Figure 1-2 shows a representative coordination sphere of a type II Cu^{2+} complex in a protein-DNA complex. One nitrogen from a histidine imidazole, two carboxylate oxygen from glutamic acids and one oxygen from a water molecule form the equatorial coordination plane. Two oxygens from water molecules axially coordinate to the Cu^{2+} center.

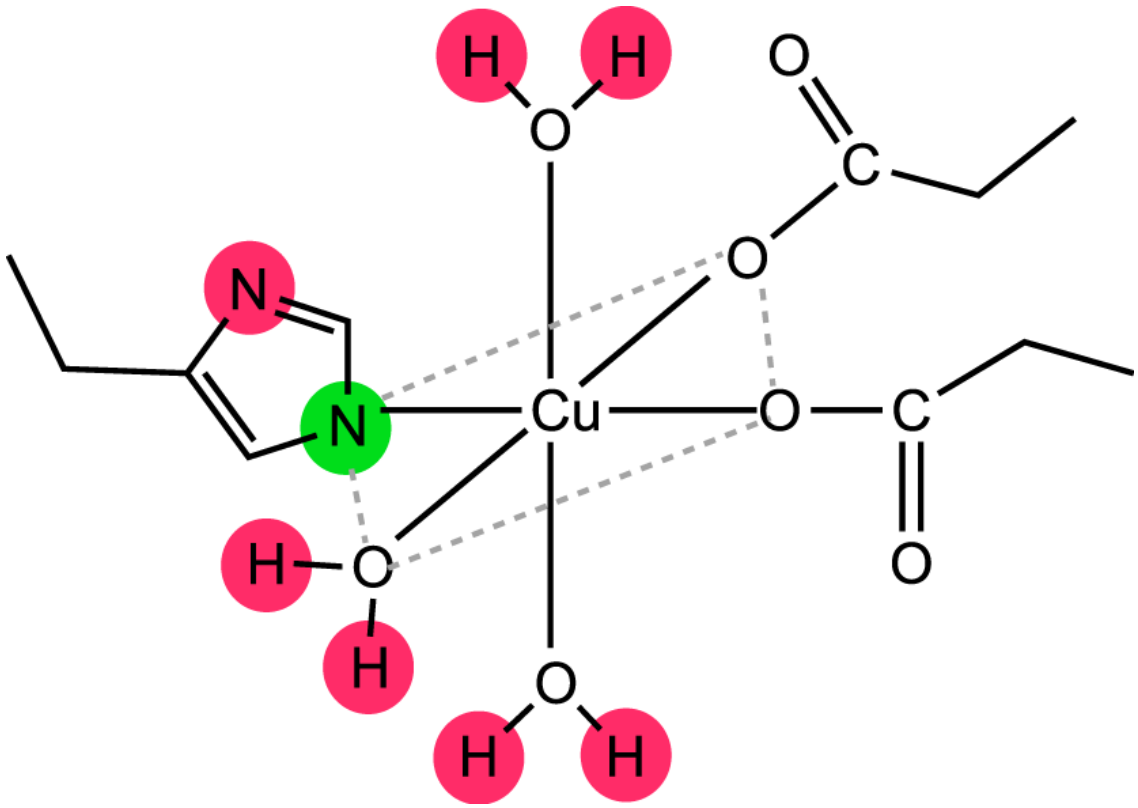

Figure 1-2. Coordination sphere of a type II Cu^{2+} complex. One nitrogen from a histidine imidazole, two carboxylate oxygens from glutamic acids and one oxygen from a water molecule form the equatorial coordination plane, shown by the grey dashed line. Two water molecules axially coordinate to the Cu^{2+} center. The directly Cu^{2+}-coordinated atom is shown by the green color. The non-coordinating atoms with $I \neq 0$ are shown by the red color (^{1}H and ^{14}N).

The hyperfine interaction between the electron spin and distant nuclei, such as ^{1}H and remote ^{14}N (not directly coordinated to Cu^{2+}, red color in Figure 1-2) usually has a magnitude of less than 15 MHz. The nuclear quadrupole interactions of Cu^{2+} and ^{14}N nuclei are usually less than 6 MHz. These interactions are too small to be resolved in the CW-ESR spectrum. The nuclear Zeeman interaction of the Cu^{2+} nucleus has a magnitude of ~4 MHz, which is negligible in the detection. The hyperfine interaction between the electron spin and directly coordinated ^{14}N, which has a magnitude ~40 MHz, may sometimes be resolved in the CW-ESR spectrum at X-band (9.5 GHz) (green color in Figure 1-2), especially at low frequencies. On the other hand, the hyperfine interaction between electron spin and Cu^{2+} nuclei (magnitude ~450 MHz) is the major interaction that can be detected in the CW-ESR. Therefore, the spin Hamiltonian in equation 1-1 can be simplified to:

$$\hat{H} = \hat{H}_{ez} + \hat{H}_{hf} = \beta_e \vec{B} \cdot \vec{g} \cdot \hat{S} + \hat{S} \cdot \vec{A} \cdot \hat{I} \tag{1-2}$$

where $\vec{A}$ is the electron spin-Cu^{2+} nucleus hyperfine interaction tensor, $\hat{I}$ is the Cu^{2+} nuclear spin angular momentum operator.

When the rotational motion of a molecule in solution is faster than the ESR timescale, the anisotropy in the *g* and *A*-tensors are averaged out. Under this condition, with the high field approximation, equation 1-2 can be re-written as:

$$\hat{H} = \hat{H}_{ez} + \hat{H}_{hf} = g_{iso}\beta_e B_0 \hat{S}_z + A_{iso} S_z I_z \tag{1-3}$$

In equation 1-3, the z axis is defined as the direction of the external magnetic field B_0, as shown in Figure 1-3. $\hat{S}_z$ and $\hat{I}_z$ are the electron and Cu^{2+} nuclear spin angular momentum operators along the z directions, respectively.

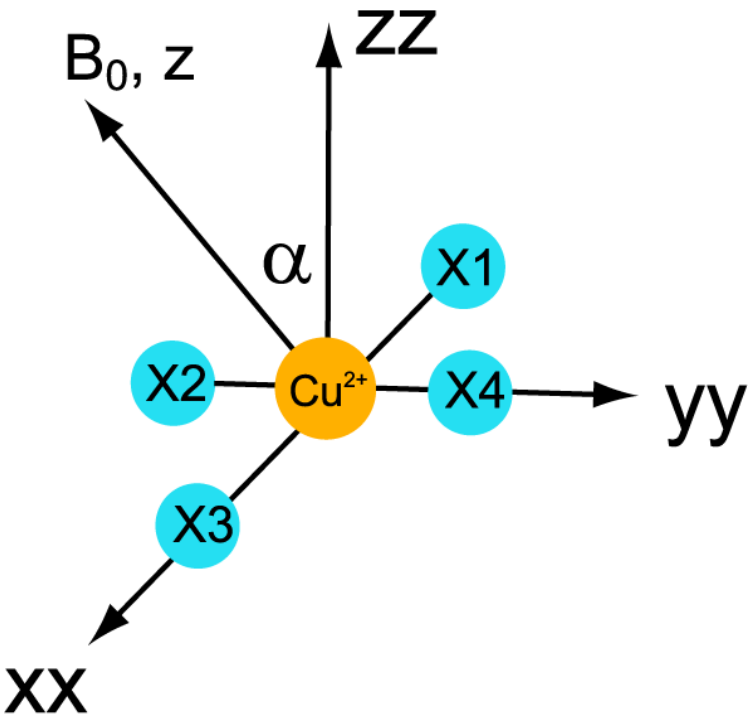

Figure 1-3. The lab frame z-axis direction is defined as the direction of external magnetic field B_0. The molecular frame directions of a type II Cu^{2+} complex are defined by *g*-tensor orientations. X represents different ligands in the complex.

The g_{iso} and A_{iso} can be calculated by:

$$g_{iso} = \frac{1}{3}(g_{xx} + g_{yy} + g_{zz}) \tag{1-4}$$

$$A_{iso} = \frac{1}{3}(A_{xx} + A_{yy} + A_{zz}) \tag{1-5}$$

where g_{xx}, g_{yy}, g_{zz}, A_{xx}, A_{yy} and A_{zz} describe the principal components of the *g*-tensor and *A*-tensor, respectively. For a typical type II Cu^{2+} complex, $g_{xx}=g_{yy}=g_{\perp}$, with a typical value at ~2.06, and g_{zz} is denoted as $g_{\parallel}$, with a typical value at ~2.28. Likewise, $A_{xx}=A_{yy}= A_{\perp}$, with a typical value ~20 G, and A_{zz} is denoted as $A_{\parallel}$, with a typical value ~160 G.[17] Figure 1-3 shows the orientation of the *g*-tensor frame, which is also defined as the molecular frame. The zz direction of the molecular frame in the type II Cu^{2+} complex is perpendicular to equatorial coordination plane. Usually the hyperfine tensor has the same principal axis as the *g*-tensor.[18]

For I=3/2 of Cu^{2+} (both naturally abundant isotopes ^{63}Cu and ^{65}Cu have the same nuclear spin), the interaction between the electron spin and Cu^{2+} nucleus leads to four possible ESR transitions in the CW-ESR spectrum as shown in the energy diagram in Figure 1-4.

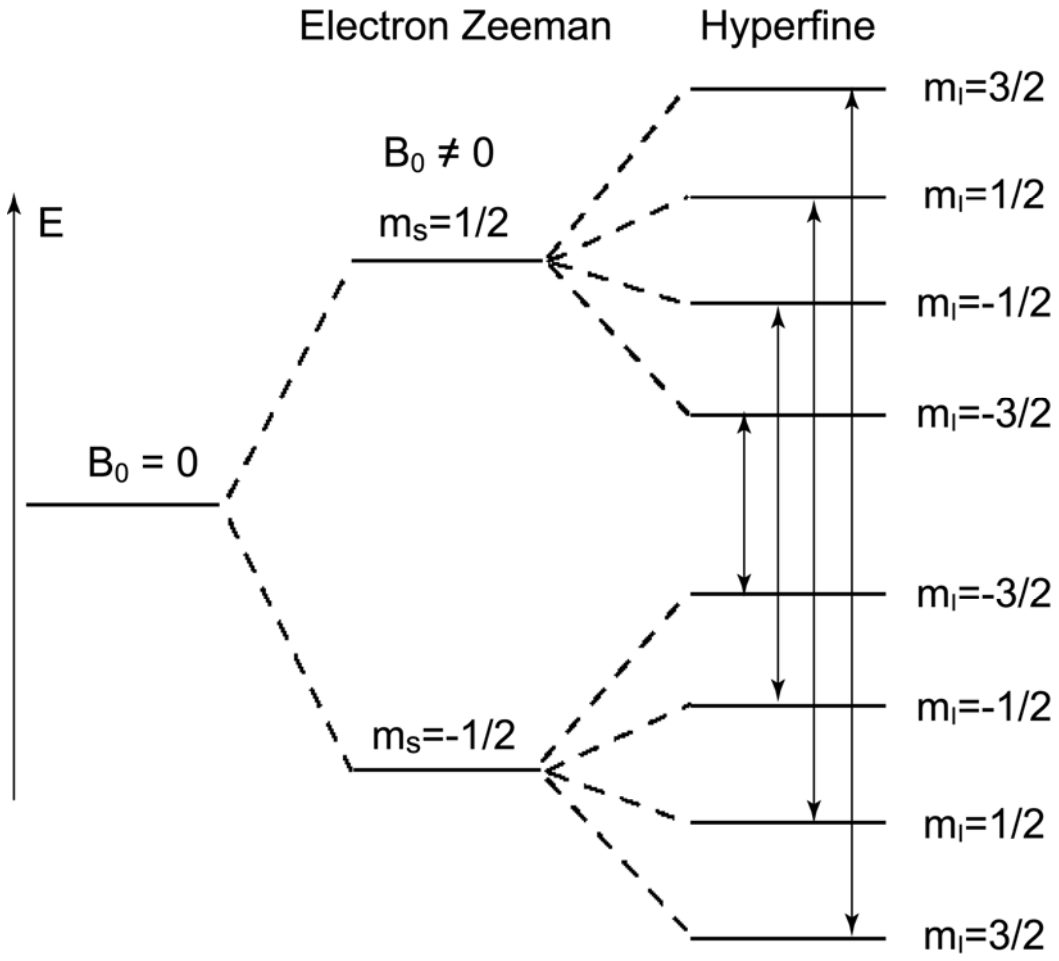

Figure 1-4 Cu^{2+} energy level diagram with isotropic *g* and *A* values. In the absence of an external magnetic field ($B_0 = 0$), the electron spin energy levels are degenerate. After applying a magnetic field ($B_0 \neq 0$), the electron Zeeman effect causes a splitting of the energy levels. Because of the hyperfine interaction between the electron spin and Cu^{2+} nucleus, the energy levels are further split. The allowed ESR transitions are shown by the vertical arrows in the diagram.

At low temperature, the rotational motion of the molecule is slower than the ESR time scale. The *g* and hyperfine interaction *A* values become orientational dependent.

For the type II Cu^{2+} complex, the *g* and hyperfine *A* values at certain orientation are given by positive square root of:[19]

$$g^2 = g_{\perp}^2 \sin^2 \alpha + g_{\parallel}^2 \cos^2 \alpha \tag{1-6}$$

$$A^2 = A_{\perp}^2 \sin^2 \alpha + A_{\parallel}^2 \cos^2 \alpha \tag{1-7}$$

where α is the angle between external magnetic field B_0 and the zz direction of the principal axis system as shown in Figure 1-3. Clearly, when the orientation between the external magnetic field and principal axis system is different, the *g* and *A* values are different. The difference in energy between two m_s manifolds depends on the *g* and *A* values (e.g. for m_s = -1/2, m_I = 3/2 and m_s = 1/2, m_I = 3/2, $\Delta E = h\nu = g\beta_e B + 3A$). Since in CW-ESR experiment the frequency ν is kept constant, the resonance magnetic field *B* changes when the *g* and hyperfine *A* values are different. Based on this, the different relative orientations between the external magnetic field and the molecule cause the resonance magnetic field to change. Therefore, the Cu^{2+} CW-ESR spectrum at low temperature becomes the superposition of different splittings with different orientations. Figure 1-5a shows a representative type II Cu^{2+} CW-ESR spectrum. The dashed and solid lines indicate the splittings with different *g* and *A* values. Since g_{xx} and g_{yy} are identical in the type II Cu^{2+} complex, any orientations in the equatorial coordination plane have the same *g* value. Thus the CW spectrum intensity at the $g_{\perp}$ region is higher than the other regions.

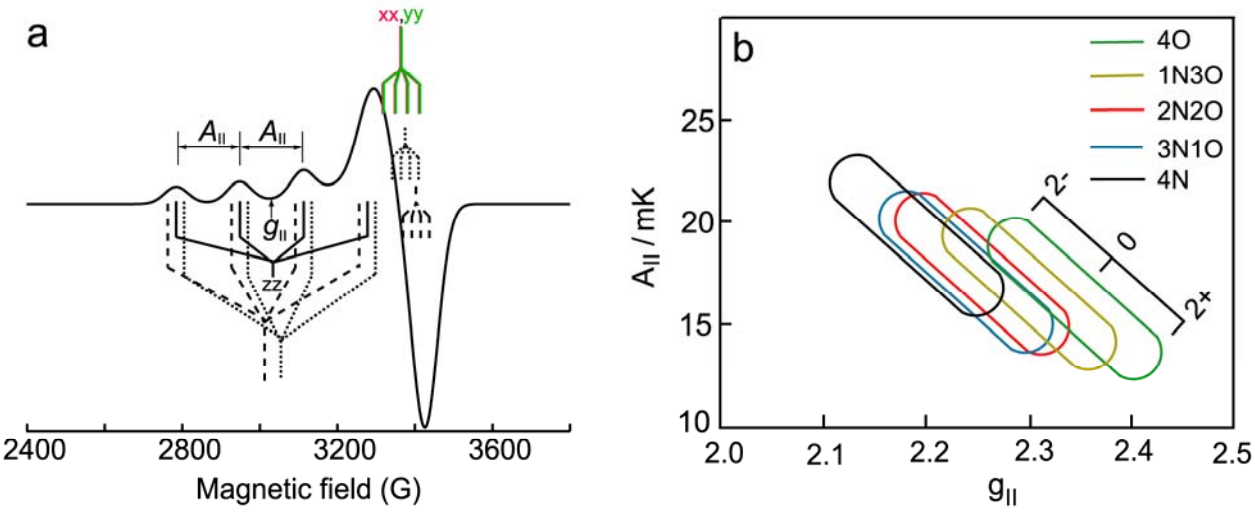

Figure 1-5. (a) Typical type II Cu^{2+} X-band CW-ESR spectrum at low temperature. The splitting due to $A_{\parallel}$ and the magnetic field position corresponding to $g_{\parallel}$ are shown on the spectrum. The dashed and dotted lines indicate the splittings when the external magnetic field is along the other directions; (b) The range of $A_{\parallel}$ and $g_{\parallel}$ values for different equatorial coordinated atoms in the type II Cu^{2+} complex. The plot is regenerated from ref. 20.

Figure 1-5a shows the magnetic field position corresponding to the $g_{\parallel}$ value and the splitting caused by the $A_{\parallel}$. The $g_{\parallel}$ and hyperfine $A_{\parallel}$ values obtained from the CW-ESR spectrum can help identify some structural information of the type II Cu^{2+} complex. The hyperfine interaction between electron spin and nuclear spin includes the isotropic or Fermi contact interaction and the dipolar interaction:

$$\hat{H}_{hf} = \hat{H}_{F} + \hat{H}_{dip} = a_{iso}\vec{S}\cdot\vec{I} - \frac{\mu_0}{4\pi\hbar} g_e g_n \beta_e \beta_n \left[\frac{\hat{S}\cdot\hat{I}}{r^3} - \frac{3(\hat{S}\cdot\vec{r})(\hat{I}\cdot\vec{r})}{r^5} \right] \qquad (1\text{-}8)$$

where

$$a_{iso} = \frac{2\mu_0}{3\hbar} g_e g_n \beta_e \beta_n \left|\psi_0(0)\right|^2 \qquad (1\text{-}9)$$

μ_0 is the permeability of vacuum, $\hbar$ is the reduced Planck constant, β_e is the Bohr magneton, β_n is the nuclear magneton, g_e and g_n are the g-values of the electron spin and nuclear spin that are coupled, $\vec{r}$ is the vector connecting the two spins. $\left|\psi_0(0)\right|^2$ is the electron spin density at the nucleus.

Based on equation (1-9), the Fermi contact is affected by the electron spin density at the nucleus. In turn, this electron density is affected by the electronegativity of the equatorially coordinated atoms. The increase of equatorially coordinated oxygen atoms leads to a decrease of the magnitude of the Fermi contact because the electronagtivity of oxygen reduces the electron spin density at the central Cu^{2+} ion. At the same time, the g-tensor of Cu^{2+} electron spin depends on the spin-orbit coupling, which is also affected by the equatorially coordinated atoms.[21] Peisach and Blumberg showed that the values of $g_{\parallel}$ and $A_{\parallel}$ were useful diagnostics of the number of equatorial coordinated nitrogen, oxygen and sulfur atoms (Figure 1-5b).[20]

While the $A_{\parallel}$ and $g_{\parallel}$ values are useful, the overlap in multiple $A_{\parallel}$ and $g_{\parallel}$ values may sometimes lead to ambiguities in assignments. Therefore, several echo-based pulsed ESR

techniques have been developed to measure hyperfine and nuclear quadrupole couplings of distant nuclei, which can provide detailed structural information on the identities of coordinating ligands.

1.3 PULSED ESR TECHNIQUES TO INVESTIGATE ELECTRON SPIN COUPLED NUCLEI

• *Electron spin echo envelope modulation (ESEEM)*

The ESEEM spectrum at X-band (~9.5 GHz) detects the hyperfine and quadrupole interactions of nuclear spins that are within ~10 Å of the Cu^{2+} center,[22,23] as shown by the atoms highlighted by red in Figure 1-2. However, at X-band, directly coordinated atoms have hyperfine values that are too large to be detected. Figure 1-6a presents the pulse sequence of three-pulse ESEEM. A stimulated echo is generated after three $\pi/2$ pulses. In the pulse sequence, the time interval τ between the first and second pulses is kept constant, and time delay T between the second and third pulses is incremented.

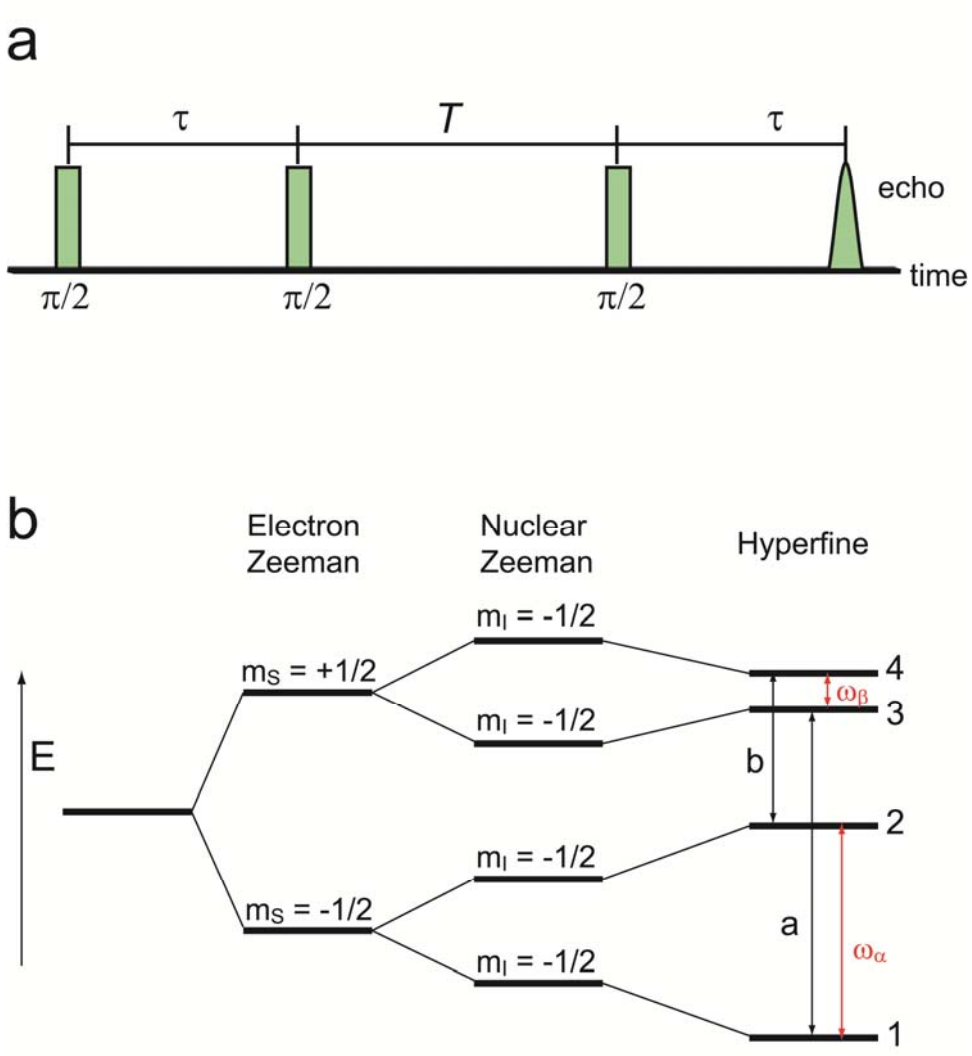

Figure 1-6. (a) Three-pulse ESEEM pulse sequence. (b) Energy diagram of a S=1/2 and I=1/2 system. The black arrows indicate the ESR transitions. The red arrows indicate the nuclear transitions in two electron spin manifolds.

The time domain signal of three-pulse ESEEM of a S = 1/2 and I = 1/2 system can be expressed as following:

$$V_{3p}(t,T) = 1 - \frac{k}{4}\left\{(1-\cos\omega_\alpha\tau)\left[1-\cos\omega_\beta(T+\tau)\right] + (1-\cos\omega_\beta\tau)\left[1-\cos\omega_\alpha(T+\tau)\right]\right\} \quad (1\text{-}10)$$

where k is the modulation depth parameter, τ and T are the separation among pulses shown in Figure 1-6a. ω_α and ω_β are the two nuclear transition frequencies in the two electron spin manifolds, as shown in Figure 1-6b. After Fourier transformation of the time domain data, we can obtain the nuclear transition frequencies (ω_α and ω_β), which are given by:[22,24]

$$\omega_\alpha = [(\omega_I - A/2)^2 + B^2/4]^{1/2};\ \omega_\beta = [(\omega_I + A/2)^2 + B^2/4]^{1/2} \quad (1\text{-}11)$$

where $A = A_{zz}$, $B = \sqrt{A_{zx}^2 + A_{zy}^2}$. A_{zz}, A_{zx} and A_{zy} are hyperfine tensor elements. $\omega_I = \gamma_I \times B_0$ is the Larmor frequency of nucleus, where γ_I is the gyromagnetic ratio, B_0 is the external magnetic field. These peaks help us to identify the type of nucleus that is coupled to the electron spin. For example, the ^{1}H provides ESEEM signal at ~14 MHz ($\omega_\alpha \approx \omega_\beta$).[25]

For an I > 1/2 nucleus, the existence of nuclear quadrupole interaction will similarly provide some characteristic spectral lines in the ESEEM spectrum. Figure 1-7 shows a typical ^{14}N-ESEEM spectrum of a Cu^{2+}-protein-DNA complex. There are three peaks at 0.60, 1.09 and 1.60 MHz as well as some broad peaks at approximately 4.0 MHz. The energy levels, shown in the inset of Figure 1-7, indicates that the hyperfine interaction between the ^{14}N nucleus and electron spin is comparable to the nuclear Zeeman interaction and cancel each other in one electron spin manifold. Therefore, the nuclear quadrupole interactions (NQI) are observed in this electron spin manifold.

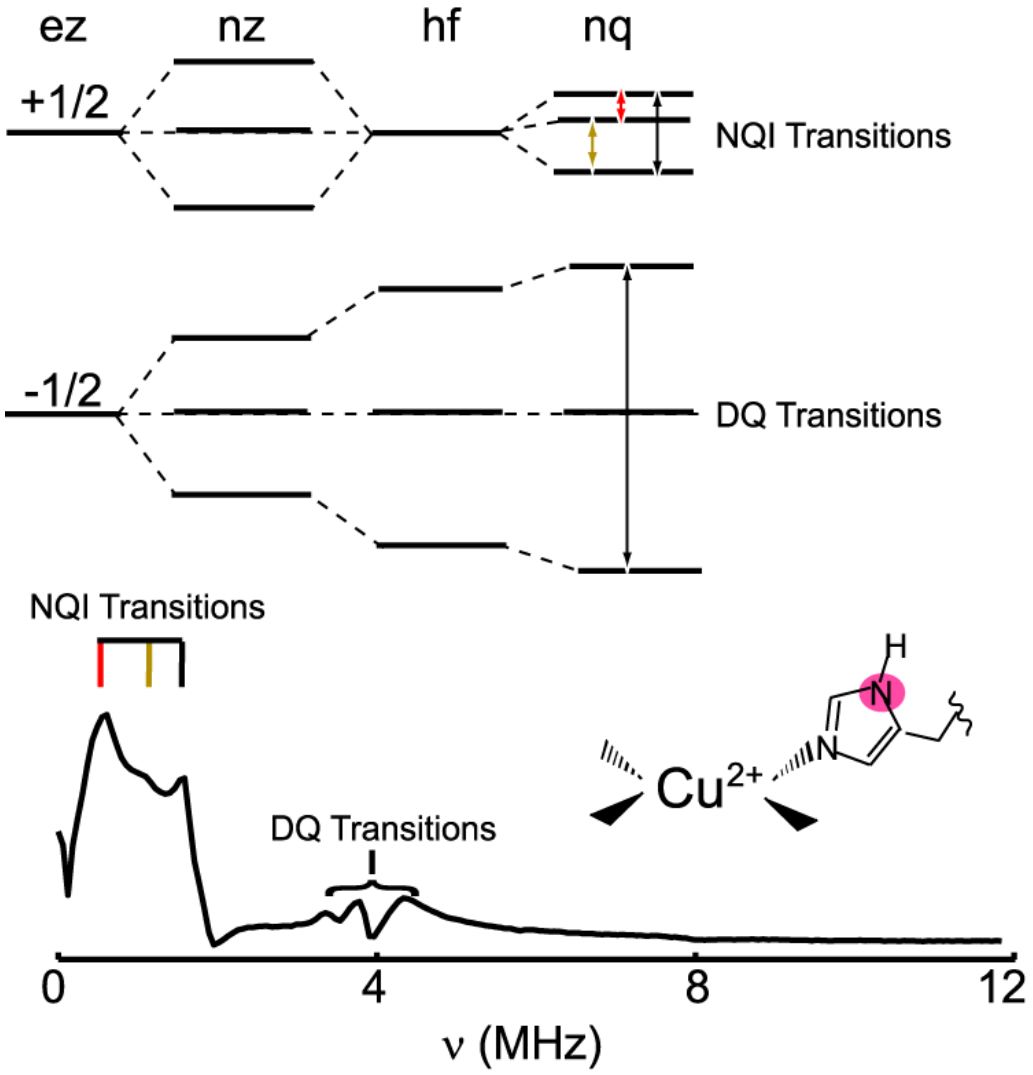

Figure 1-7. The ESEEM spectrum shows characteristic frequencies when Cu^{2+} coordinates to the histidine imidazole ring.[7] The red color labeled ^{14}N atom provides these ESEEM signals. The energy levels show the NQI and DQ transitions in the spectrum.

The three transitions of the NQI as shown in Figure 1-7 inset are given by:[26]

$$\nu_{-} = \frac{e^2 qQ(3-\eta)}{4h};\ \nu_0 = \frac{2\eta e^2 qQ}{4h};\ \nu_{+} = \frac{e^2 qQ(3+\eta)}{4h} \tag{1-12}$$

where e is the electron charge, q is the electric gradient at the nuclear site, Q is the nuclear quadrupole moment, η is the asymmetry parameter, h is Planck′s constant. The sum of the two lower frequencies is equal to the highest one.

The broad peaks at ~ 4.0 MHz are from the double quantum (DQ) transition shown in the inset of Figure 1-7. This DQ transition frequency is given by:[27]

$$\nu_{dq} = 2\sqrt{(\nu_I + \frac{A^2}{2}) + \frac{B^2}{4} + \frac{e^2 qQ(3+\eta^2)}{4h}} \tag{1-13}$$

These NQI and double quantum transitions can be used to characterize the local structure around the Cu^{2+} center. For example, when Cu^{2+} coordinates to histidine, the remote ^{14}N nucleus provides three NQI peaks below 2 MHz (at ~ 0.5 MHz, ~1.0 MHz and ~1.5 MHz) and a DQ transition at ~4 MHz.[28] If more than one histidine residues simultaneously coordinate to Cu^{2+} center, combination peaks might appear between 2 and 3.5 MHz.[29] At the same time, as the number of Cu^{2+}-coordinated histidine residues increases, the relative intensity of the DQ peak increases.[30-33] When the protein backbone carbonyl oxygen coordinates to Cu^{2+}, the interaction between the nearest remote amide ^{14}N and Cu^{2+} generates the ESEEM signals at ~2 and 3 MHz.[28] All these transitions in ESEEM spectra are fingerprints that help identify histidine coordination or protein backbone interaction.[23,27,28,30,32,34,35] Combined with spectral simulations, the hyperfine coupling constants and the relative orientation between the Cu^{2+} center and remote nuclei, such as ^{14}N, can be estimated to provide detailed structural information.

• *Hyperfine sublevel correlation (HYSCORE)*

From equation (1-10), it is clear that at certain τ values, (1-cos$\omega_\alpha \tau$) or (1-cos$\omega_\beta \tau$) could be zero. This may cause the peaks at ω_β or ω_α not be observed in the ESEEM experiment, which is called the blind-spot effect. To obtain a robust time domain data, we need to collect a series of data with different τ values. At the same time, some transitions of different nuclei in the ESEEM are close to each other and may overlap in the spectrum. For example, the DQ transition of ^{14}N shows a broad peak at ~4.0 MHz, may cover a range from 3 MHz to 5.5 MHz. The ^{31}P nucleus gives a ESEEM signal at ~5.5 MHz.[36] These signals may not be resolvable in the ESEEM spectrum, thus making it difficult to unambiguously identify the Cu^{2+} coordination environment. The 2D experiment HYSCORE[37] provides a useful alternative to resolve information which is not easily obtained from 1D ESEEM experiments and also overcome the blind spot problem.

The pulse sequence of HYSCORE is shown in Figure 1-8a. Compared to the three-pulse ESEEM, another π pulse is inserted in between the second and third π/2 pulses. The interval t_1 between the second π/2 and π pulses as well as the interval between π and third π/2 pulses are independently incremented. The π pulse interchanges the nuclear coherence between two electron spin manifolds. Thus, HYSCORE spectrum can identify the nuclear transitions in two electron spin manifolds from the same nucleus. The HYSCORE spectrum usually contains diagonal peaks as well as cross peaks. The cross peaks can provide further nuclear frequency information and improve spectrum resolution, especially when nuclear peaks overlap in the 1D experiment.

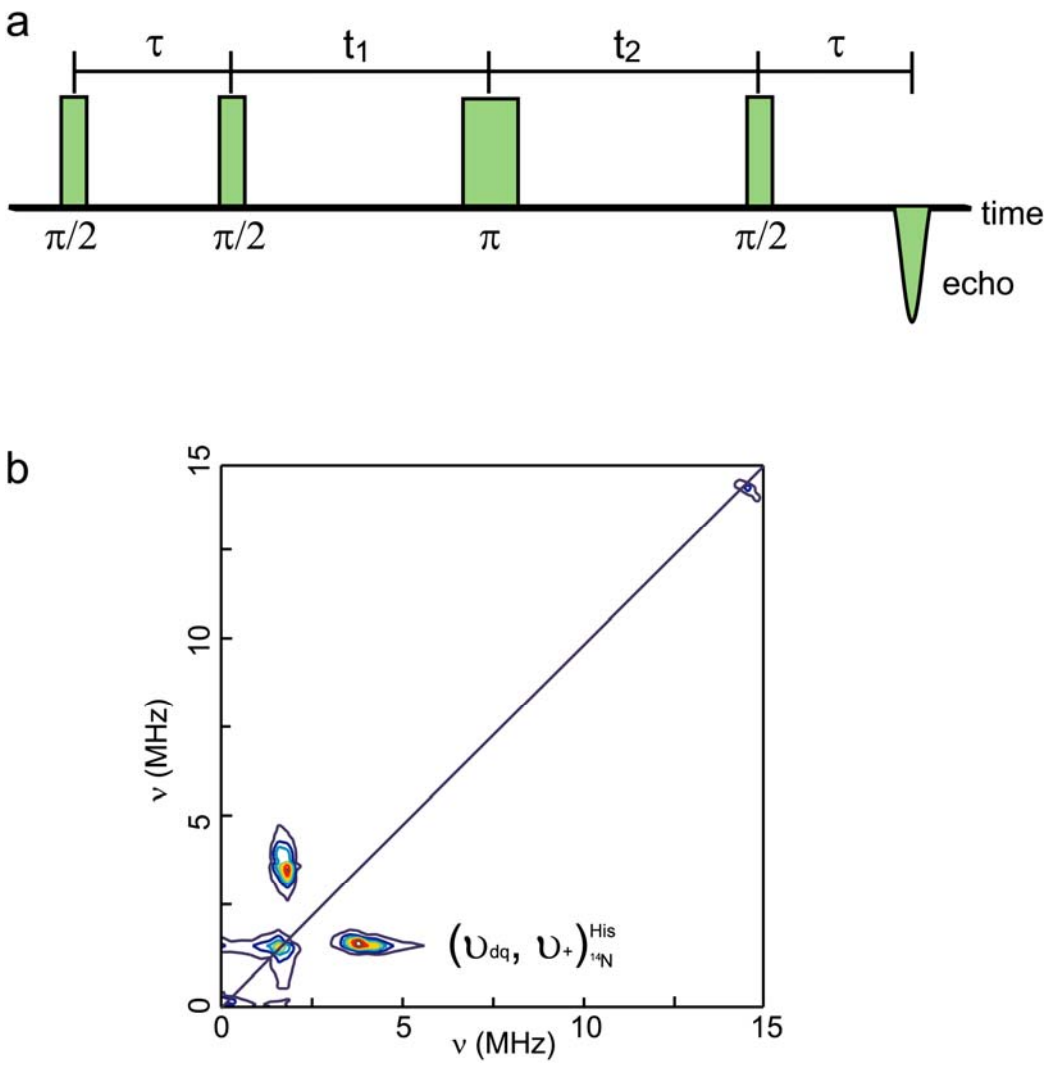

Figure 1-8. (a) HYSCORE pulse sequence. (b) Cross peaks at (~1.5 MHz, ~4.0 MHz) provide the evidence of Cu^{2+}-imidazole interaction.

For example, in HYSCORE spectrum, the ^{31}P nucleus provides cross peaks at (~2 MHz, ~10 MHz) and a diagonal peak at ~5 MHz,[36] while the ^{14}N nucleus from histidine imidazole presents cross peaks at (~1.5 MHz, ~4 MHz). Figure 1-8b shows a typical HYSCORE spectrum of the same Cu^{2+} sample as in Figure 1-7. The presence of the cross peaks at (~1.5 MHz, ~4 MHz) help identify the Cu^{2+}-histidine coordination. The absence of the cross peaks at (~2 MHz, ~10 MHz) and the diagonal peak at ~5 MHz excludes the interaction between the Cu^{2+} center and ^{31}P nucleus. Combined with ESEEM, the structure around Cu^{2+}, such as Cu^{2+}-histidine and Cu^{2+}-backbone ^{14}N coordination can be unambiguously identified.[28]

• *Electron nuclear double resonance (ENDOR) spectrum*

Apart from ESEEM and 2D HYSCORE techniques introduced in the previous section, electron nuclear double resonance (ENDOR) spectroscopy is another technique that measures the hyperfine interactions between the electron spin and nuclear spin. ENDOR can provide hyperfine parameters with much higher precision than the other ESR techniques. This technique uses two different frequencies in the experiment. A microwave frequency is used to monitor the electron spin transitions, and a radio frequency is applied to change the electron spin population difference between energy levels.

• *Mechanism of ENDOR spectrum*

Here, a simple S = 1/2 and I = 1/2 system is used to explain the mechanism of ENDOR spectroscopy. Figure 1-6b shows this system when *g* and *A* are isotropic. Based on the selection rule ($\Delta m_s = \pm 1$, and $\Delta m_I = 0$), only two transitions occur in ESR spectroscopy between energy levels 1 and 3 (**a**), and energy levels 2 and 4 (**b**). The amplitude of these two transitions is proportional to the population difference among these energy levels. The transitions between energy levels 1 and 2, as well as 3 and 4 are the nuclear transitions ($\Delta m_s = 0$, and $\Delta m_I = \pm 1$). To

simplify the discussion, we only consider the ESR transition between energy levels 1 and 3, as well as the nuclear transition between energy levels 1 and 2. When the radio frequency radiation induces the nuclear transition between energy levels 1 and 2, the electron spin populations in levels 1 and 2 are equalized or reversed, which causes the population difference in energy levels 1 and 3 to change. Hence, the electron spin resonance signal **a** becomes dependent on the radio frequency radiation.

CW-ENDOR

In CW-ENDOR, the ESR transition **a** in Figure 1-6b is saturated by a continuous microwave. Simultaneously, a radio frequency (rf) radiation induces the nuclear transition between energy levels 1 and 2. The intensity of ESR transition **a** is:[38]

$$E = 1/(4 + 2\frac{W_n}{W_e} + 2\frac{W_e}{W_n}) \tag{1-14}$$

where W_n and W_e are the relaxation rates between energy levels 1 and 2, and levels 1 and 3, respectively. The ENDOR signal is recorded as a function of rf frequency. Based on this equation, it is clear that the CW-ENDOR signal intensity depends on the relaxation properties of the system in a critical way. This relaxation dependent property makes CW-ENDOR restricted to a narrow temperature range.

Pulsed ENDOR

The pulsed ENDOR techniques are based on the electron spin echo (ESE) signal, which is generated by microwave pulse. The radio frequency (rf) pulse, which generates the NMR allowed transitions ($\Delta m_s = 0$, and $\Delta m_I = \pm 1$; the transitions shown by the red arrow in Figure 1-6b), changes the electron spin population at different energy levels. Thus the intensity of the ESE signal depends on the rf pulse frequency. The ENDOR signal is recorded as the amplitude of the ESE signal change versus the rf pulse frequency. Compared to CW-ENDOR, the entire pulse

sequence in pulsed ENDOR technique is short enough to avoid the relaxation dependence. Therefore, pulsed ENDOR can be utilized in a larger temperature range than the CW-ENDOR. In the following section, details of two pulsed ENDOR techniques are discussed.

The microwave pulse sequence of Davies ENDOR and Mims ENDOR are shown in Figure 1-9.[38] As shown in Figure 1-10, the first microwave π pulse in Davies ENDOR inverts the electron spin population between two energy levels, e.g. 1 and 3. After the first π pulse, a radio frequency π pulse is applied to the system. The final ESR transition between energy levels 1 and 3 is detected by the two-microwave pulse sequence π/2-τ-π-τ-echo. When the radio frequency pulse is on resonance with nuclear transition between energy levels 3 and 4, the electron spin population of these two levels alters, and therefore, the echo intensity changes. When the rf pulse is off resonance with nuclear transition between energy levels 3 and 4, there is no change in electron spin population and the echo intensity does not change. The final ENDOR signal is recorded as a function of the rf pulse frequency.

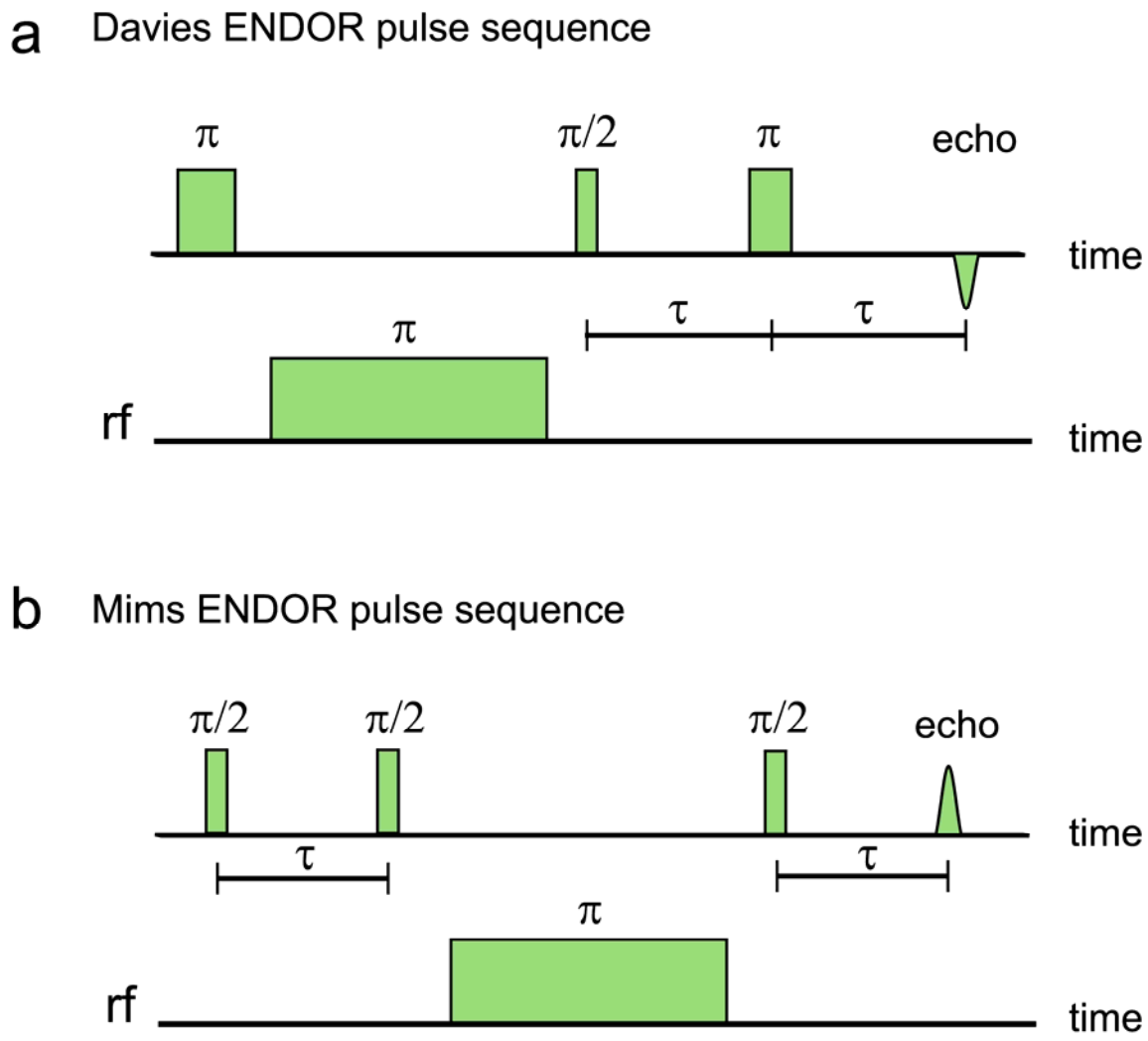

Figure 1-9. (a) Davies ENDOR pulse sequence. All the time intervals are fixed. The rf pulse is in between the first microwave π and π/2 pulses; (b) Mims ENDOR pulse sequence. All the time intervals are fixed. The rf pulse is in between the second and third microwave π/2 pulses.

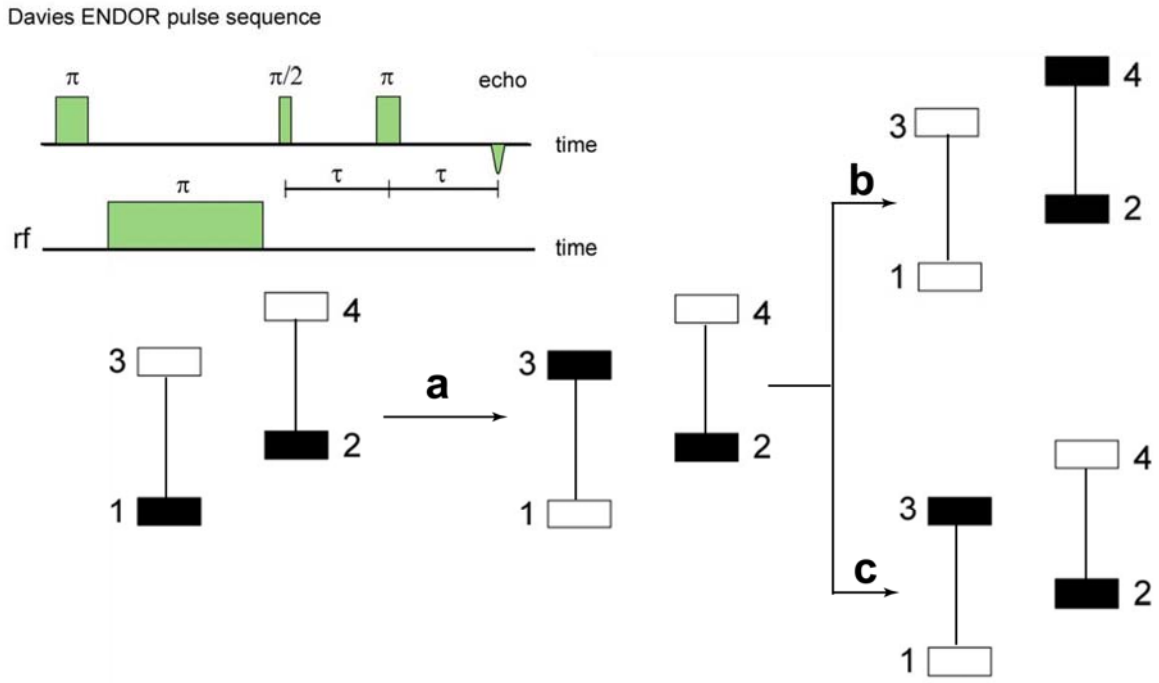

Figure 1-10. Effect of pulses in the Davies ENDOR experiment. The first microwave π pulse inverts the spin population in energy levels 1 and 3 (a). When the rf π pulse is on resonance of the transition between energy levels 3 and 4 (b), the echo signal from the transfer between energy levels 1 and 3 changes. When rf π pulse is off resonance (c), the echo signal from the transfer between energy levels 1 and 3 will not change.

.

In Mims ENDOR, both the ESR transitions (1 to 3 and 2 to 4) are excited by the mw pulse. The rf pulse changes the value of m_I, which in turn changes the local magnetic field of the electron spin. Thus the electron spin Larmor processing frequency changes accordingly. The frequency of this procession during the first and second τ period differs by a value of *a*. The echo intensity detected is then proportional to:[38]

$$S_y = \cos(a\tau) \tag{1-15}$$

Based on this relationship, when $a\tau = 2\pi n$, where n is an integer number, no ENDOR signal can be detected. Thus Mims ENDOR exhibits a blind spot behavior: with certain τ values, the ENDOR sensitivity is severely decreased. Thus, it requires collection of data at different τ values to avoid this blind spot problem.

In Davies ENDOR, only one ESR transition is required to be excited by the mw pulse, such as the transition between energy levels 1 and 3 shown in Figure 1-10. Under this condition, the amplitude of the microwave pulse should be properly adjusted to avoid the excitation of the second ESR transition. When the system has large hyperfine interactions, the difference in the frequencies between the two ESR transitions (energy levels 1 to 3 and 2 to 4 in Figure 1-10) is large. Accordingly, it is easier to excite only one ESR transition as compared with a system that has small hyperfine interactions. Therefore, Davies ENDOR is useful for nuclei with relatively large hyperfine interactions, such as ^{1}H, ^{14}N. Compared to Davies ENDOR, Mims ENDOR is more sensitive to weakly coupled nuclei with small hyperfine values (less than 2 MHz), such as deuterium nucleus, since both ESR transitions need to be excited by microwave pulse.[38].

With the nuclear Zeeman and hyperfine interaction information in ENDOR spectra, it is possible to identify the nuclei that are coupled to the electron spin, such as ^{1}H, ^{14}N and ^{31}P as well as the spatial relationships between the coupled nuclei and electron spins. Combined with

the solvent exchange (e.g. D_2O exchange) technique, ENDOR results can be used to clarify the source of ^1H signals, such as the solvent exchangeable ^1H. The details of this application of ENDOR will be shown in Chapter 4 of this thesis.

1.4 HIGH FIELD ESR

Although X-band (~9.5 GHz) ESR spectroscopy can provide useful information for identifying the Cu^{2+}-coordination environment in molecules, W-band (~ 94 GHz) can provide complementary information to help elucidate the structure around Cu^{2+}.

There are several advantages of high field ESR spectroscopy. First, high field provides higher spectral resolution. High field allows separation of paramagnetic centers with small g value differences. As shown in Figure 1-11a, two Cu^{2+} components with different $g_{\|}$ values (2.228 and 2.289) in the EcoRI-DNA complex are poorly resolved in the CW-ESR spectrum at X-band (~9.5 GHz) (inset in Figure 1-11a). However, a much higher resolution of the two Cu^{2+} components is achieved at W-band (~94 GHz) (Figure 1-11a, black solid line).

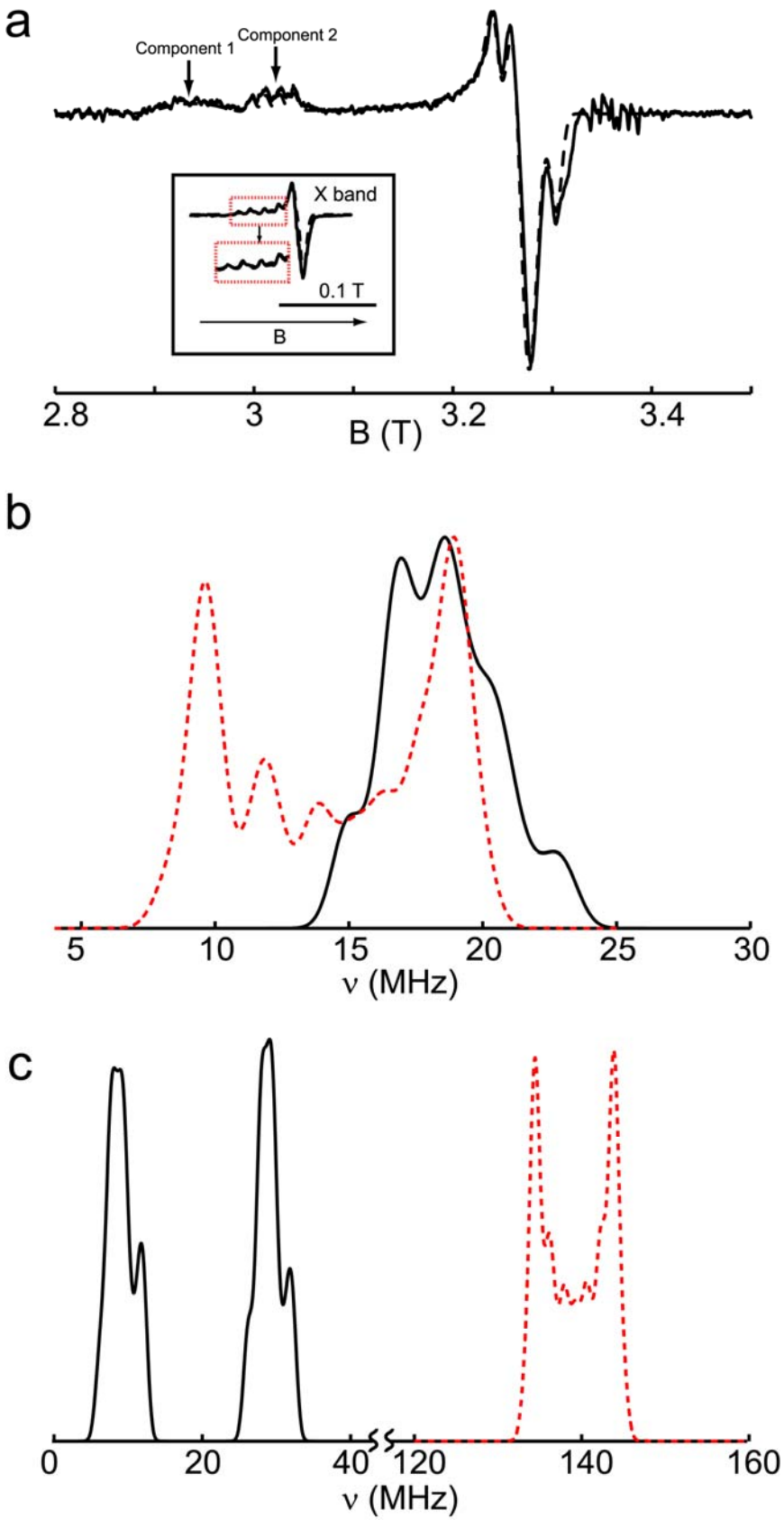
a
Component 1
Component 2
X band
0.1 T
B
2.8
3
3.2
3.4
B (T)
b
5
10
15
20
25
30
ν (MHz)
c
0
20
40
120
140
160
ν (MHz)

Figure 1-11. (a) First derivative of the W-band field-swept electron spin echo (FS-ESE) spectrum of the Cu^{2+}-EcoRI-DNA complex. The two Cu^{2+} components with different g_{zz} values are completely resolved, shown here by the arrow. The inset shows the CW-ESR spectrum of the same complex at X-band. The two components are poorly resolved as shown by the dotted red rectangle. (b) Simulated X-band ENDOR spectrum of ^{14}N (red dotted line) and ^{1}H (black solid line). The parameters for the simulation are: ^{14}N, the three hyperfine values are 32, 33, 42 MHz, the three quadrupole values are 0.20, 0.68, -0.88 MHz; ^{1}H, the three hyperfine values are -10.5, -10.5, 12 MHz. The g_{xx}, g_{yy} and g_{zz} values for the simulation are 2.055, 2.055 and 2.289, respectively. (c) Simulated W-band ENDOR spectrum of ^{14}N (red dotted line) and ^{1}H (black solid line). The parameters for the simulation are the same as in Figure 1-11b.

At the same time, because of the significantly large nuclear Zeeman interaction at high field, signals from different nuclei with non-zero spin are better resolved in ENDOR experiments. For example, the ENDOR signals of ^{14}N are between 10 MHz and 20 MHz at X-band, which is also the range of ^{1}H signals. A simulated ^{14}N (black solid line) and ^{1}H ENDOR (red dotted line) signals at X-band is shown in Figure 1-11b. This overlap makes it difficult to distinguish the ^{14}N and ^{1}H ENDOR signals. Figure 1-11c shows the ENDOR signals of ^{14}N and ^{1}H at W-band. The ^{1}H ENDOR signal is centered at ~140 MHz at W-band, while the ^{14}N signal is still at ~20 MHz. This frequency difference largely simplifies the signal collection and assignment procedures. Second, small *g*-anisotropies can be easily determined. The wide spread ESR spectra allows for the measurement of the orientation selective spectra detection. Third, in high electron spin systems, high order effects that result in increased inhomogeneous broadening are significantly reduced. Fourth, in pulsed ESR experiments at high field, the spectrometer dead time is significantly reduced because the pulse ring down time constant is inversely proportional to the spectrometer frequency.[39]

1.5 THE DISTANCE MEASUREMENT BY DOUBLE QUANTUM COHERENCE (DQC)

Several pulsed ESR techniques have been widely utilized for long distance distribution measurements, such as double electron-electron resonance (DEER)[40-44] and double quantum coherence (DQC).[45,46] These experiments measure the distance-dependent dipolar interaction between two spins. These ESR distance measurements are advantageous in providing structural information of biological systems.

• *Dipole-dipole coupling between two interacting spins*

In a system with two interacting electron spins, the spin Hamiltonian is given by

$$\hat{H} = \hat{H}_1 + \hat{H}_2 + \hat{H}_{12} \tag{1-16}$$

where $\hat{H}_1$ and $\hat{H}_2$ are the spin Hamiltonian of each electron spin, which have the same expression as in equation (1-1).

$$\hat{H}_{12} = \hat{S}_1 \cdot \vec{D} \cdot \hat{S}_2 - J\,\hat{S}_1 \cdot \hat{S}_2 \tag{1-17}$$

where $\vec{D}$ is the dipolar coupling tensor between two electron spins, and J represents the exchange interaction between these two spins. $\hat{S}_1$ and $\hat{S}_2$ are the electron spin angular momentum operators of the first and second spins. When the distance between the two electron spins is longer than 12 Å, this exchange interaction can be neglected.[47] Equation (1-17) can then be simplified as:

$$\hat{H}_{12} = \hat{S}_1 \cdot \vec{D} \cdot \hat{S}_2 = \frac{\mu_0}{4\pi\hbar r_{12}^3} g_1 g_2 \beta_e^2 \left[\hat{S}_1 \cdot \hat{S}_2 - \frac{3(\hat{S}_1 \cdot \vec{r}_{12})(\hat{S}_2 \cdot \vec{r}_{12})}{r_{12}^2} \right] \tag{1-18}$$

here μ_0 is the permeability of vacuum, $\hbar$ is the reduced Planck constant, β_e is the Bohr magneton, g_1 and g_2 are the isotropic g-values of the first and second electron spins that are coupled, $\vec{r}_{12}$ is the vector connecting the two electron spins. When the experiments are done at low temperature and with the high field approximation, equation (1-18) can be further simplified as:

$$\hat{H}_{12} = \frac{\mu_0}{4\pi\hbar r_{12}^3} g_1 g_2 \beta_e^2 \hat{S}_{1z} \hat{S}_{2z} (1 - 3\cos^2\theta) \tag{1-19}$$

where θ is the angle between the external magnetic field and the interspin vector as shown in Figure 1-12.

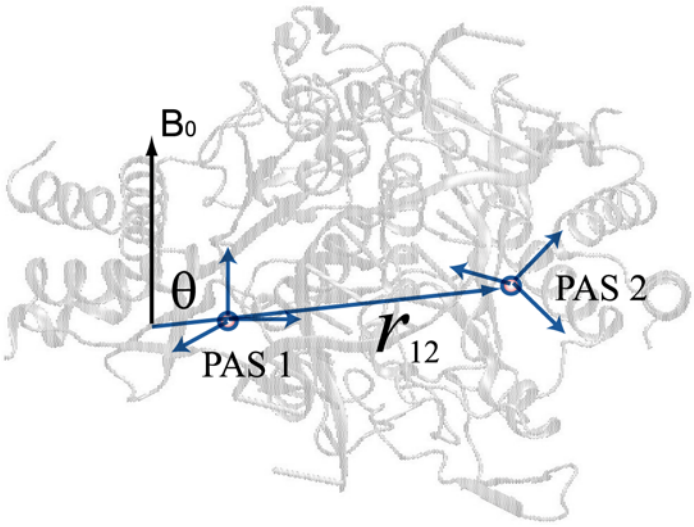

Figure 1-12. The orientation of interspin vector $\vec{r}_{12}$ with respect to the external magnetic field B_0. The molecular frame of the two spin centers are shown as PAS1 and PAS2.

In this thesis, we used the DQC technique to measure the Cu^{2+}-Cu^{2+} distance distribution in the EcoRI-DNA complex.

• *Double quantum coherence (DQC)*

Double quantum coherence is a pulsed ESR technique applied for distance measurements between two electron spin centers separated by up to 80 Å.[45,46] Compared to the commonly used DEER, DQC does not require a second frequency to excite the electron spins and can provide higher signal-to-noise ratio per shot.

The six-pulse DQC-ESR pulse sequence is shown in Figure 1-13, with a $\pi/2$-t_p-π–t_p-$\pi/2$-t_1-π-t_1-$\pi/2$-t_m-π-t_m-echo sequence. The DQC pulse sequence excites the double quantum coherence that relates to the dipolar interaction of a spin pair. Figure 1-13 also shows the corresponding coherence pathways to form the echo. The final DQC signal with non-selective pulses is given by:[48,49]

$$V(t_p, t_m) = \sin(2\pi\upsilon_{1,2}t_p)\sin(2\pi\upsilon_{1,2}t_m) \tag{1-20}$$

where $\upsilon_{1,2} = \frac{\mu_0}{4\pi\hbar r_{12}^3} g_1 g_2 \beta_e^2 (1 - 3\cos^2\theta) + 2J$.

A 256-step phase cycling is required in the DQC experiment to selectively measure the proper signal.[48,49]

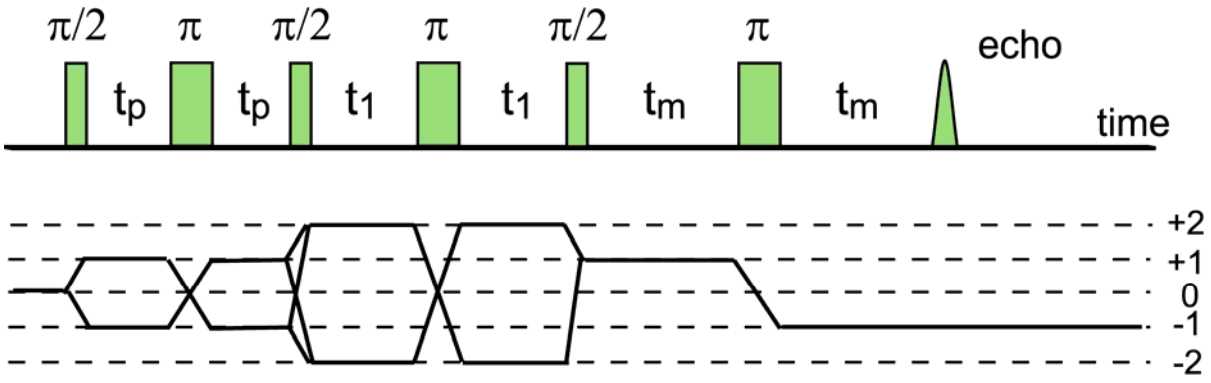

Figure 1-13. Pulse sequence of DQC and associated relevant coherence pathways.

2.0 PARAMAGNETIC METAL IONS IN PULSED ESR DISTANCE DISTRIBUTION MEASUREMENTS

This work, written in collaboration with Sharon Ruthstein and Sunil Saxena, has been accepted for publication in Accounts of Chemical research.

2.1 INTRODUCTION

Advances in measuring interspin distance distributions using pulsed electron spin resonance (ESR) have added an important new tool in biophysical research. There are three major pulsed ESR techniques for the distance distribution measurements with long-range distance accessibility: relaxation rate based distance distribution measurements,[50] double quantum coherence (DQC),[45,46] and double electron electron resonance (DEER) also known as pulsed electron double resonance (PELDOR).[40-44] Among these methods, the DEER/PELDOR technique has become the most widely used approach. The prevalence of DEER is largely due to the ease of implementation on commercial instruments, as well as due to the availability of programs that can analyze experimental data to obtain distance distributions.[51,52] However, microwave pulses at two different frequencies are required in DEER experiments.[40-44]

Most DEER distance distribution measurements are based on the site-directed spin-labeling technique wherein a cysteine residue is chemically modified with the nitroxide

methanethiosulfonate spin label (MTSSL).[53] The application of site-directed spin-labeling and DEER in biophysics and materials research has been extensively reviewed recently.[3-6]

Figure 2-1 shows the R1 side chain generated by the reaction between cysteine(s) and MTSSL. The conformation of the side chain is defined by the dihedral angles of the five rotatable bonds between the protein backbone and the nitroxide ring, denoted as χ_1 through χ_5. One limitation of MTSSL is that the distance distributions are often dominated by the conformational preferences of the R1 side chain. Numerous attempts have been made to account for the spatial distribution of R1 in experimental distance distributions.[54-61]

As an alternative, researchers have begun to employ endogenously bound paramagnetic metal ions as spin probes for ESR distance distribution measurements. Metal ions are involved in a variety of important biological processes, including photosynthetic electron transfer,[62,63] catalysis and gene regulation,[64,65] metabolism of carbon, nitrogen and sulfur,[66] hydrolysis of amides and esters,[67-69] and disease mechanisms.[70-74] More than 30% of proteins require metal ions for function.[75] Utilizing these endogenously bound paramagnetic metal ions as probes for ESR detection only causes minimal functional perturbation to molecules. Distance distributions based on such endogenously bound metal ions may potentially be related to backbone conformations with greater ease than MTSSL, which may simplify the interpretation of protein structure.

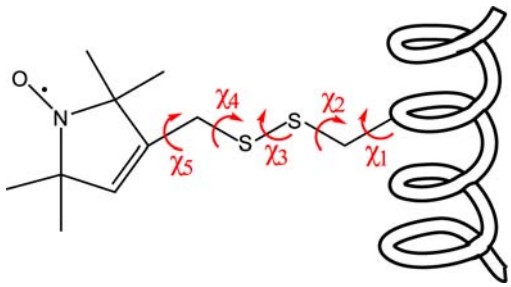

Figure 2-1. Structure of the R1 side chain. Five dihedral angles, χ_1-χ_5 are needed to describe the orientation of the side chain.

Huber and co-authors presented the very first work in detecting the distance distribution between two Cu^{2+} centers in the dimer azurin structure.[76] Subsequently, other groups have used Cu^{2+} as a spin probe to detect the conformation of linked porphyrins, polypeptides and proteins.[7,77-82] Iron-sulfur clusters have also been introduced as spin probes for structural detection.[83-85] To achieve high sensitivity, Gd^{3+} as well as Mn^{2+} have been used as spin probes for high frequency DEER experiments.[86-96] The Gd^{3+}-based DEER distance method has been reviewed recently.[97]

2.2 CHALLENGES OF USING CU^{2+} IN DEER EXPERIMENTS

Sensitivity: The pulses in DEER experiments on Cu^{2+} excite fewer spins when compared with MTSSL, which leads to a reduction in sensitivity of the DEER signal. Figure 2-2a shows the ESR absorption spectra of Cu^{2+} (red dotted line) and MTSSL (green solid line) at low temperature. Because of the larger anisotropic values of *g* and hyperfine tensors, the ESR absorption spectrum of Cu^{2+} is ~10 times broader than MTSSL at X-band (~9.5 GHz), as is shown in Figure 2-2a. The blue dashed line in Figure 2-2a shows the typical coverage of a 36 ns microwave pulse, which is typically used in DEER experiments. With the same pulse length, significantly fewer spins can be excited in Cu^{2+} spectrum as compared with MTSSL.

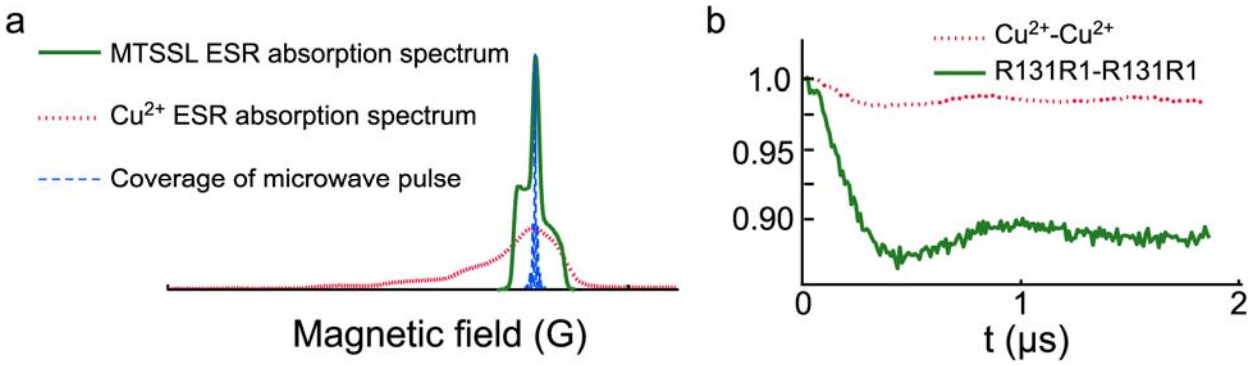

Figure 2-2. (a) ESR absorption spectra of Cu^{2+} (red dotted line) and MTSSL (green solid line). The coverage of a 36 ns microwave pulse is shown in blue dashed line. (b) Cu^{2+}-Cu^{2+} (red dotted line)[7] and R131R1-R131R1 DEER (green solid line)[13] signals after baseline subtraction in the EcoRI-DNA complex with 44 ns and 48 ns pump pulse, respectively.

The DEER time domain signal can be expressed as:[4,41,81,98]

$$V(t) = 1 - \iint P(r)\left(\lambda - \lambda \cos[\frac{k}{r^3}(1 - 3\cos^2 \theta)t] \right)\xi(\theta) d\theta dr \qquad (2\text{-}1)$$

where $P(r)$ is the distance distribution and θ is the angle between the interspin vector and the external magnetic field, as shown in Figure 2-3a. k is a constant that is proportional to the product of the g values of two spin centers, and r is the distance between two spins. In equation 1, λ is the modulation depth and $\xi(\theta)$ is the geometrical factor. The broad Cu^{2+} ESR absorption spectrum at low temperature leads to a low modulation depth in DEER, as well as possible complications from limited excitation of spins. These are discussed in the following sections.

Modulation depth: The modulation depth, λ, is the fraction of spins excited by the pump pulse, which are also coupled to the spins that are excited by the observer pulse.[99] The modulation depth depends on the pump pulse length as well as the shape of the ESR absorption spectrum.[40,100] A small modulation depth causes a low signal-to-noise ratio in the time domain data.[101,102] Also it is disadvantageous in the discrimination of nuclear modulations. Figure 2-2b shows the Cu^{2+}-Cu^{2+} (red dotted line) and R131R1-R131R1 DEER time domain data (green solid line) in the specific EcoRI-DNA complex. The Cu^{2+}-Cu^{2+} DEER data with a shorter pump pulse (44 ns) has a much smaller modulation depth (~2%) compared to the ~13% modulation depth of R131R1-R131R1 with a longer pump pulse (48 ns).[7,13] By using commercial available microwave pulse forming unit to provide shorter pump pulses (e.g. 16 ns) and by choosing a proper frequency offset to minimize nuclear modulation, data with modulation depth of ~12% can be obtained on Cu^{2+} at X-band (9.5 GHz frequency).[102]

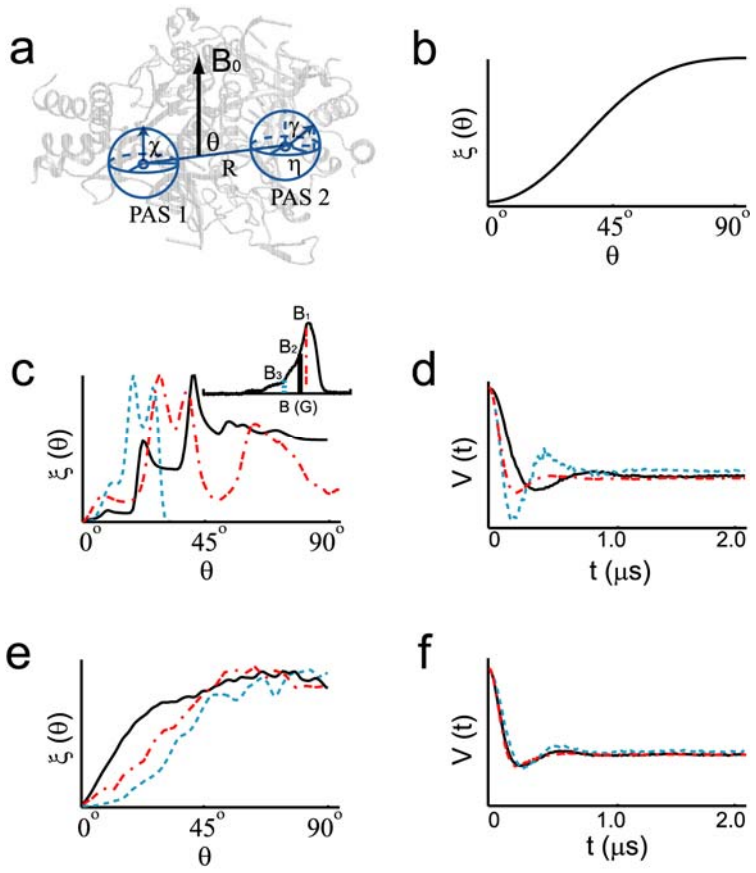

Figure 2-3. (a) The diagram shows the orientation θ, of a vector connecting two interacting spins, R, with respect to the external magnetic field B_0. The relative orientation of the two spin centers is defined by three angles χ, γ and η. PAS1 and PAS2 denote the principle axis systems of the *g*-tensors of the first and second spin, respectively; (b) Ideal geometrical factor $\xi(\theta)$; (c) Representative calculations of the geometrical factor $\xi(\theta)$ at three magnetic fields (B_1 = 3342 G, B_2 = 3290 G and B_3 = 3060G) shown in the *inset*. The simulations assume a small orientational distribution (standard deviation of 2°) between two Cu^{2+} centers. The pump pulse frequency is 92 MHz lower than the observer pulse frequency in these simulations; (d) Simulated DEER signals at three magnetic fields with the geometrical factors as shown in panel c; (e) The geometrical factor $\xi(\theta)$ at three magnetic fields as shown in Figure 3c *inset* (B_1 = 3342 G, B_2 =

3290 G and B_3 = 3060G) with a larger orientational distribution (standard deviation of 10°); (f) Simulated DEER signals at three magnetic fields with the geometrical factors shown in panel e.

Interestingly, the six-pulse double quantum coherence (DQC)–based distance distribution measurements have a small background signal,[103] which allows for an easier extraction of the dipolar interaction. On the other hand, the DQC signal has substantial contributions from electron-nuclear interactions between the electron spin and neighboring ^{14}N as well as ^{1}H nuclear spins that are present in the amino-acid coordination environment. These nuclear modulation effects may swamp the modulation due to the electron-electron dipolar interactions and make it difficult to measure the interspin distance distribution.

We recently presented a simple way to minimize these low-frequency nuclear peaks in the DQC spectrum and resolve the dipolar interaction between two Cu^{2+} centers with high sensitivity, by dividing two DQC signals with different pulse lengths.[103] This simple DQC method has a signal-to-noise ratio twice as high as DEER per shot. Further improvements in Cu^{2+} based DQC can be made by the use of narrower pulse lengths and by manipulating the pulse sequence to avoid acquisition of two DQC time domain signals. However, because of the narrower pulse lengths in the experiments, the power of the microwave pulse required in DQC is much higher than in the DEER experiment. Additionally, the 256-step phase cycling in the experiment leads to a much longer data collection time. These factors limit the application of DQC on commercial instruments.

Orientational selectivity effect: In Cu^{2+}-based DEER, because of the broad absorption ESR spectrum, a typical microwave pulse of ~36 ns can only excite a small portion of the θ angles. Both the electron-electron dipolar frequency [$\omega_{ee}= \frac{k}{r^3}$ (1-3cos$^2\theta$)] as well as the geometrical factor, $\xi(\theta)$, depend on the position of the microwave pulse. Hence, the DEER signals at different external magnetic field positions might have different modulation periods and

modulation depths. This phenomenon is known as the "orientational selectivity" effect.[77,79,81,104,105]

In MTSSL-based DEER, the interplay of the anisotropies of *g* and hyperfine tensors and the flexibility of the R1 side chain typically randomize the relative orientation between the spin labels. When a pump pulse (e.g. 36 ns) is applied at the maximum of the MTSSL absorption spectrum, an ideal θ excitation profile [i.e. geometrical factor $\xi(\theta)$] can be achieved as shown in Figure 2-3b.[79-81] In this case, the model-free Tikhonov regularization method has been developed to analyze the time domain data and obtain accurate distance distributions.[51,52]

In Cu^{2+}-based DEER, the signal may potentially depend on the relative orientation between the two metal ions. For the case of Cu^{2+}, the relative orientations between the two metal ions can be defined by three angles χ, γ and η with certain orientational distribution, as shown in Figure 2-3a. Simulations with a pump pulse of 36 ns, shown in Figure 2-3c, yield three different geometrical factors at three different magnetic fields (B_1 = 3342 G, B_2 = 3290 G, and B_3 = 3060 G). For these simulations, χ, γ and η angles are 60°, 60° and 0°, respectively. Each angle is assumed to be Gaussian distributed with a standard deviation of 2°.

The simulated DEER time domain data shown in Figure 2-3d with geometrical factors from Figure 2-3c shows that even with the same distance distribution, this partial selectivity can potentially lead to different DEER signals[77,79-81,104,105] at different external magnetic field positions. Figure 2-3e shows that with the increase of the orientational distribution between two Cu^{2+} centers, the geometrical factor $\xi(\theta)$ become broader and more θ angles are excited.[81] Accordingly, the time domain orientational selectivity effect is largely reduced as shown in Figure 2-3f.

DEER experiments on peptides and proteins show that the orientational selectivity effects are small but detectable.[7,81] The Cu^{2+}-Cu^{2+} DEER data in the EcoRI-DNA complex are shown in Figure 2-4a. The modulation periods changes by ~60 ns (~10% of the modulation period) at different magnetic fields.[7] Nevertheless, the data analyzed by using the model-free Tikhonov regularization method gives distance distributions that have artifacts (shoulder peaks) and most probable distances that differ by 1 to 3 Å (dashed lines shown in Figure 2-4b).[81] A difference in the width of the distance distributions may also be observed.[81] If only the most probable distances are needed and when the orientational selectivity effects are weak, the measured most probable distances based on Tikhonov regularization method are still acceptable within 1 to 3 Å error range.[78,81] For a more accurate measurement, one needs to collect data at different magnetic fields and frequency offsets and include the effects of orientational selectivity to analyze all the data.[81] As shown in Figure 2-4, a single distance distribution can fit the data when orientional selectivity is included in the analysis.[7] On smaller molecules, the data can also be analyzed based on molecular dynamics simulations and DFT calculations.[79,80,105] Strong suppression of orientational selectivity can also be achieved by summing experimental traces collected at different external magnetic fields (field averaging)[106,107] or with different frequency offsets.[108]

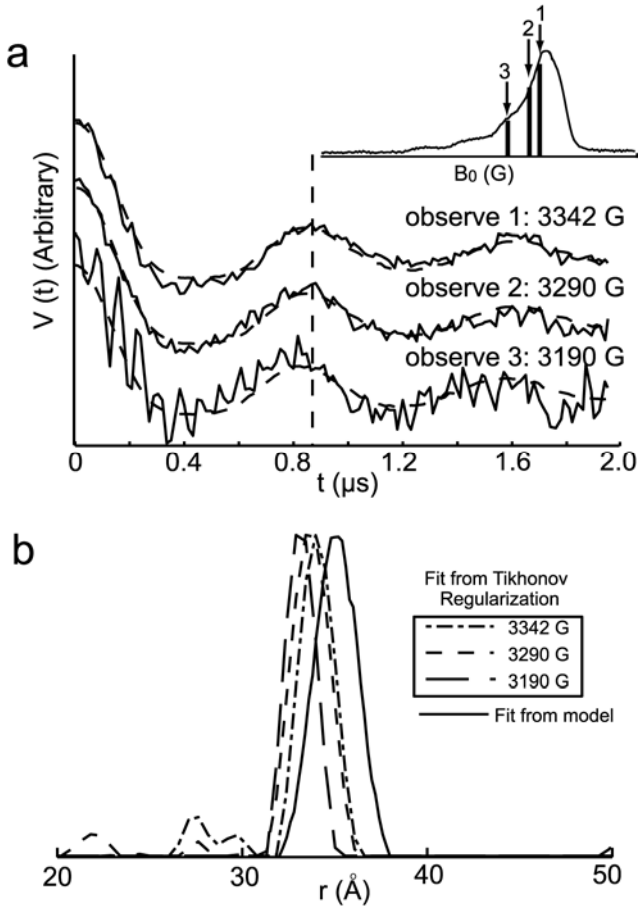

Figure 2-4. (a) Cu^{2+}-Cu^{2+} DEER signal in the EcoRI-DNA complex at different magnetic fields with the same frequency offset (100 MHz). The positions of the observer pulse are highlighted on the absorption ESR spectrum shown on the *inset*. The normalized signals are offset in the y-axis in order to clearly indicate the modulation periods. The vertical dashed line indicates the modulation period difference; the dashed line shows the simulations using the procedure described in reference 81; (b) The distance distribution functions (dashed lines) obtained at different external magnetic fields (3342 G, 3290 G and 3190 G) using the Tikhonov regularization method; the Cu^{2+}-Cu^{2+} distance distribution (solid line) obtained by accounting for orientational selectivity.

2.3 APPLICATIONS OF METAL ION-BASED DEER

Elucidation of protein-DNA interaction by Cu^{2+}-based DEER: We have recently focused on the use of ESR to examine the relationship between DNA sequence recognition and catalytic specificity in a DNA-modifying enzyme. The EcoRI endonuclease, a 62 kDa homodimer, recognizes the DNA site 5'-GAATTC-3' and cleaves both DNA strands in the presence of the catalytic cofactor Mg^{2+}. Interestingly, the DNA cleavage rates are as much as 10^6–fold higher for the GAATTC site than for sites with a different base pair sequence. Importantly, Cu^{2+} by itself does not support DNA cleavage by EcoRI.[109] Therefore, it is appropriate as a spin probe in this protein-DNA system. Cu^{2+} based distance measurements thus provide an exciting route to probe the structural and electrostatic effects that determine site specific catalysis in this class of enzymes.

We utilized bound Cu^{2+} ions and site-directed spin-labeling to shed light on the Cu^{2+} interaction with EcoRI. X-band pulsed techniques like electron spin echo envelope modulation (ESEEM) spectroscopy and hyperfine sub-level corelation (HYSCORE) spectroscopy results established that Cu^{2+} ions coordinate to a histidine in EcoRI. There are 5 histidine residues in each EcoRI monomer (H31, H114, H147, H162, H225). We obtained Cu^{2+}-Cu^{2+} (on wild type EcoRI) and Cu^{2+}-S180R1 distances using DEER-ESR to identify the Cu^{2+}-coordinated histidine. Interestingly, more than one complete modulation period was observed for the Cu^{2+}-Cu^{2+} DEER data (Figure 2-4a). This observation indicates that the endogenously bound Cu^{2+} in the EcoRI-DNA complex provides a relatively fixed reference point for the distance measurements. This may be an advantage when two close distance distributions need to be resolved.

A single, most probable Cu^{2+}-Cu^{2+} distance distribution of 35 Å was observed with a standard deviation of 1 Å. Cu^{2+}-S180R1 distance measurements yielded two most probable

distances at 22 Å and 42 Å with standard deviations of 2 Å and 3 Å, respectively. These distances were similar to the H114 N_ε-H114 N_ε distance (red solid line in Figure 2-5a) as well as H114 N_ε-S180 C_α intra- (green dotted line in Figure 2-5a) and intermonomer (blue dashed line in Figure 2-5a) distances from the metal free EcoRI-DNA crystal structure.[110] The distance distributions from ESR experiments were uniquely consistent with Cu^{2+} binding to H114. This was strongly supported by biochemical studies, which showed that the mutant H114Y-DNA complex binds Cu^{2+} with 1600-fold lower affinity than the wild type EcoRI-DNA complex.

Unexpectedly, we found that Cu^{2+} is a powerful inhibitor of EcoRI catalysis; 100 μM Cu^{2+} completely inhibits cleavage by wild type EcoRI. On the other hand, even at 200 μM, Cu^{2+} does not inhibit H114Y-catalyzed DNA cleavage in the presence of Mg^{2+}. This data further supports our conclusion that Cu^{2+} binds to H114 rather than the negative charge cluster (E111, D91, G**p**AATTC) that coordinates to Mg^{2+}.

An earlier model from Jen-Jacobson's group suggests that sequence-dependent DNA distortion has a critical function in EcoRI catalysis.[111] As shown in Figure 2-5b, the Mg^{2+}-bound water (W_a) that makes the nucleophilic attack on the scissile phosphate is precisely positioned by H-bonding to another water (named W_c). The W_c water is held in turn by H-bonding to both H114-N_ε as well as to a phosphoryl oxygen of the phosphate GA**p**ATTC, one step downstream from the scissile phoshate.

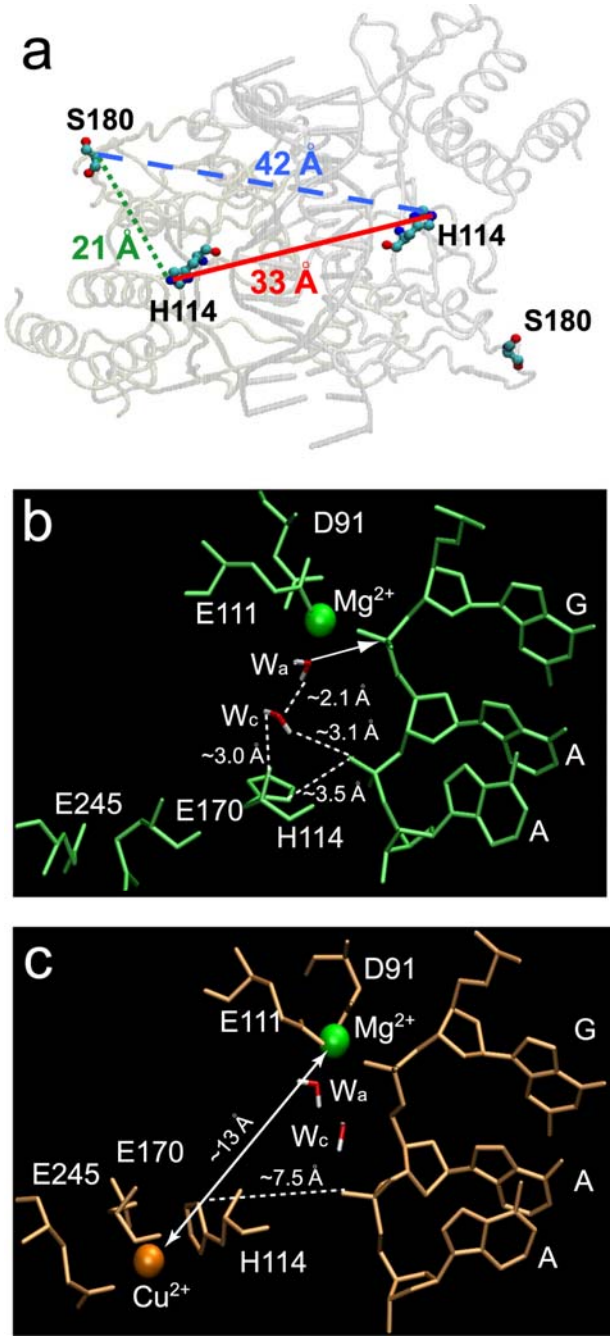

Figure 2-5. (a) The H114 N_ε–H114 N_ε (red solid line) as well as intra (green dotted line) and intermonomer (blue dashed line) S180 C_α-H114 N_ε distances from crystal structure of metal-free EcoRI-DNA complex (PDB ID 1CKQ);[110] (b) The local structure of the EcoRI-DNA complex with only Mg^{2+}; (c) The local structure of the EcoRI-DNA complex with both Mg^{2+} and Cu^{2+}.

This water network is only possible when EcoRI-induced DNA distortion creates a unique configuration, which brings the two phosphates into an unusual spatial relationship. Detailed MD simulations with explicit solvent showed that H114 is ~4 Å from its normal position in the presence of Cu^{2+} as shown in Figure 2-5c. Lacking interaction with H114, the GA**p**A phosphate moves to where it cannot support the water network that is crucial for the DNA cleavage. The overall picture is that the conformation essential for catalysis no longer exists in the presence of Cu^{2+}.

Selective measurement of Cu^{2+}-Cu^{2+} distances in a multi-copper binding protein: Recently, MacMillan and co-workers applied a new DEER technique to selectively measure Cu^{2+}-Cu^{2+} distance distributions in nitrite reductase from *Achromobacter xylosoxidans* (AxNiR).[82] Each monomer in this homotrimeric protein contains two different types of Cu^{2+}-sites. The presence of six Cu^{2+} in the protein leads to overlapping distances that are not completely resolved in the DEER experiment. The authors were able to selectively measure distances between Cu^{2+}-ions in one of the two sites by exploiting the differences in spin-lattice relaxation times. In this approach an inversion recovery filter was used before the DEER sequence to suppress the signal from one of the two Cu^{2+}-site at a time.[82]

The application of other metal ions in DEER experiments: High-quality DEER data using Gd^{3+} as a spin probe have been observed at high magnetic fields.[86-95] Gd^{3+} is a $S = 7/2$ ion with an isotropic *g*-factor. Several characters of Gd^{3+} make it a candidate for the DEER distance distribution measurements at high fields.[55] First, with the increase of frequency, the central transition $|-1/2\rangle \rightarrow |1/2\rangle$ narrows. Therefore, the sensitivity of Gd^{3+} in ESR increases with increasing of frequency. Second, because of the large zero-field-splitting distribution, the central transition can be considered effectively isotropic and Gd^{3+} abolishes the orientational selectivity

effect at high magnetic fields. Thus, Gd^{3+}-based DEER allows the determination of precise distance distributions from DEER time domain traces by using the model-free Tikhonov regularization. The collection of a series of data at different external magnetic fields or with different frequency offsets is therefore not needed.[112] Furthermore, the use of cysteine-specific Gd^{3+} labels allows the application of Gd^{3+}-based DEER to any protein.[97] The Cu^{2+}-based DEER method can be similarly generalized by the use of EDTA-Cu^{2+} labels that can be incorporated into proteins through a disulphide linkage on cysteines.[113] Similar to Gd^{3+}, Mn^{2+} also displays an intense and relatively narrow center transition at high fields. On the other hand, the reduced toxicity of Mn^{2+} compared with Gd^{3+} makes the Mn^{2+}-based distance distribution measurements even more attractive at high fields.[96] There are also reports of DEER distance distribution measurements by using iron-sulfur clusters.[83] The electron spin delocalization over the cluster causes the point-dipole approximation to break down, and the spin projection factors need to be included to analyze data.[84,85]

2.4 SUMMARY AND OUTLOOK

In this account, we presented the application of paramagnetic metal ion Cu^{2+} in DEER. Although small modulation depth and orientational selectivity effects complicate the data collection and analysis procedures, the simple sample preparation process and limited spatial flexibility make Cu^{2+} an attractive probe for research. The application of Cu^{2+}-based distance measurements in the restriction endonuclease EcoRI-DNA complex illustrates the potential of using Cu^{2+} to probe structural and electrostatic effects that determine site specific catalysis in this class of enzymes. The development of methods that use other paramagnetic metal ions, for example, Gd^{3+} and Mn^{2+}, as spin probes for high field DEER experiments may overcome the orientational selectivity effect from Cu^{2+}-based DEER and extend the reach of pulsed ESR distance distribution measurements.[86,96]

2.5 ACKNOWLEDGMENT

This research was supported by National Science Foundation grants, MCB 0842956 and MCB 1157712.

3.0 ESR SPECTROSCOPY AND MD SIMULATIONS REVEAL A NEW DIVALENT METAL ION BINDING SITE IN A PROTEIN-DNA COMPLEX

Part of this work, written in collaboration with Zhongyu Yang, Michael R. Kurpiewski, Jacque E. Townsend, Preeti Mehta, Linda Jen-Jacobson and Sunil Saxena, has been published in Proc. Natl. Acad. Sci. U.S.A., 2012, V.109, pages E993-E1000. Author contributions: L. J.-J. and S. S. designed research; M. R. K., J. E. T. and P. M. performed sample preparation, equilibrium binding studies, cleavage kinetics and isothermal titration calorimetry; Z. Y. performed the distance measurements; M. J. performed the other ESR experiments, MD simulations and electrostatic potential calculations. Z. Y., M. R. K. M. J., J. E. T., L. J.-J. and S. S. analyzed the data.

3.1 INTTRODUCTION

Protein-DNA interactions are important in many essential biological processes, including gene transcription, regulation and replication. Many of these processes involve the modification of DNA. It is, therefore, interesting to elucidate the details of how DNA-modifying enzymes bind to and catalyze DNA cleavage or repair, at specific positions. Type II restriction endonucleases EcoRI is an exemplary system for answering this question.[114,115] EcoRI is a 62 kDa homodimer. It recognizes the DNA 5'-GAATTC-3' site and binds to this site up to 90,000-fold better than the

sites that differ by only one base pair.[114,116] With the existence of divalent metal ion Mg^{2+},[111,114] EcoRI cleaves both DNA strands at positions indicated by the arrows:

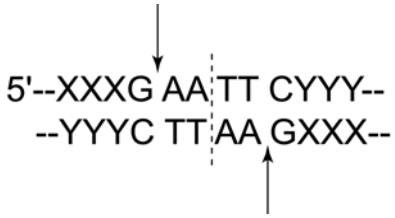

Importantly, the catalytic rate is as much as 10^6–fold higher for specific sites than for sites that differ by one base pair.

The EcoRI homodimer, with its specific DNA site, contains two catalytic centers. In contrast to some metallonucleases that use two Mg^{2+} per catalytic site, EcoRI is generally considered to use only one Mg^{2+} at each catalytic center.[110,117,118] In each center, one Mg^{2+} coordinates to the carboxylate sidechains of D91, E111 and the oxygen of scissile phosphate GpAATTC.[110,111] By using biochemical studies with chiral phosphate analogues and molecular dynamics (MD) simulations, Kurpiewski et al. proposed a mechanism of the Mg^{2+}-catalyzed DNA cleavage by EcoRI.[111]

With different divalent metal ions, the catalytic rates for EcoRI vary according to the series $Mg^{2+} \approx Mn^{2+} > Co^{2+} >> Zn^{2+} >> Cd^{2+} > Ni^{2+}$.[109,117] Ca^{2+} cannot catalyze the cleavage. On the other hand, it can inhibit the Mg^{2+}-catalyzed cleavage by competing with Mg^{2+}.[111] Cu^{2+} has a similar ionic radius (73 pm) compared to Mg^{2+} (72 pm).[119] Interestingly, Cu^{2+} by itself, does not support the DNA cleavage by EcoRI.[109]

Given the similar ionic radius and the same charge, why Cu^{2+} and Mg^{2+} behave differently in the DNA catalysis is of interest. In this chapter, we combined ESR spectroscopy with biochemical studies to identify the Cu^{2+} binding site in the EcoRI-DNA complex in order to understand the functional difference between Cu^{2+} and Mg^{2+}. Unexpectedly, we found that Cu^{2+}

profoundly inhibits the Mg^{2+}-catalyzed cleavage. By using MD simulations to refine the local protein-DNA structure in the presence of Cu^{2+}, a possible inhibition mechanism is proposed. This inhibition mechanism further confirmed the catalytic mechanism of the Mg^{2+}-catalyzed DNA cleavage proposed by Kurpiewski et al..[111]

In order to fulfill its biological function, EcoRI simultaneously cleaves both DNA strands with the existence of Mg^{2+}.[111,117] A single-strand nicking of DNA can be rapidly repaired by DNA ligases *in vivo*.[120]Another critical question, therefore, is how EcoRI inactivates the foreign DNA by simultaneous double-strand cuts. This question is particularly intriguing because the two catalytic sites are relatively distant (i.e. ~25 Å from each site). In order to answer this question, we used MD simulations and electrostatic potential calculations to elucidate the genesis for the long range interaction between the two catalytic centers. Based on the results, we propose a mechanism of Mg^{2+}-binding that enables double-strand cleavage. Taken together, all these results shed light on the structural and electrostatic factors that affect the site-specific catalysis by EcoRI.

3.2 MATERIALS AND METHODS

ESR experiments: All of the pulsed ESR experiments were performed on a Bruker Elexsys 580 spectrometer at 20 K. The continuous wave ESR experiments were performed at 80 K. A MS3 resonator was used in the continuous wave-ESR experiments. A MD5 resonator was used in all the pulse experiments.

***ESEEM experiment*:** The three-pulse ESEEM signal was collected by recording the stimulated electron spin echo intensity as a function of T using the pulse sequence: $(\pi/2)$-τ-$(\pi/2)$-T-$(\pi/2)$-τ-

(stimulated echo), on the Cu^{2+}-bound EcoRI–DNA complex. The duration of the (π/2) pulses was 16 ns. The interpulse delay τ was fixed at 200 ns. The time interval T was incremented from 400 ns with a step size of 16 ns, for a total of 1024 points. A four step phase cycle was employed to eliminate unwanted signals.[121,122]

***Hyperfine sublevel correlation (HYSCORE) experiment*:** The HYSCORE signal was collected by recording the electron spin echo intensity as a function of T1 and T2 using the pulse sequence: (π/2)-τ-(π/2)-T1-(π)-T2-(π/2)-τ-(echo), on the Cu^{2+}-bound EcoRI–DNA complex. The duration of the (π/2) and (π) pulses was 16 ns and 32 ns, respectively. The interpulse delay τ was fixed at 140 ns. The time intervals T1 and T2 were incremented from 400 ns with a step size of 16 ns, for a total of 512 points. A four-step phase cycling was employed to eliminate unwanted signals.

Molecular dynamics simulation: A highly refined EcoRI-DNA structure based on PDB code 1CKQ[110] was used as the starting structure for all molecular dynamics simulations. Hydrogen atoms were added onto the protein and DNA using psfgen in the NAMD program.[123] The CHARMM22/CMAP and CHARMM27 force field were used for the MD simulation.[124-126] The system was hydrated by TIP3P water molecules[127] to 8 Å beyond any EcoRI-DNA complex atoms. An explicit 0.22 M NaCl (80 Na^+ and 80 Cl^-) salt concentration was used for a periodic water box with size of 90 × 92 × 73 Å. Additional Na^+ ions (20 to 28, depending on the situation) were added to neutralize the charge in the water box. The effective concentration of the EcoRI-DNA was approximately 2.5 mM within the water box. SHAKE[128] was used to restrain all bonds (tolerance 0.000001 Å) and an Ewald[129] cutoff of 10 Å was assigned. The positions of the added hydrogens, water molecules and added salt were refined by energy minimization using a conjugate gradient method. The system was then heated up to 300 K and equilibrated for 0.5 ns with a time step of 1 fs in an isobaric-isothermal (NPT) ensemble (1 atm; 300 K) using the

Langevin piston method. During both minimization and equilibration, the protein backbone and DNA were restrained.

After the equilibration, a molecular dynamics run was initiated (300 K) at the University of Pittsburgh Center for Simulation and Modeling with a time step of 1 fs were performed in a canonical (NVT) ensemble. All MD simulations were performed using the NAMD 2.7b3 program.[130] Simulations were performed on EcoRI-TCGCGAATTCGCG complexes with (i) no metal ions, (ii) one active site (either A or B) with Mg^{2+}, (iii) both active sites A and B with Mg^{2+}, (iv) one subunit (either A or B) with Cu^{2+}, (v) both subunits with Cu^{2+}, (vi) both active sites A and B filled with Mg^{2+}, one Cu^{2+} added to one subunit (either A or B), (vii) both active sites A and B filled with Mg^{2+}, and a Cu^{2+} ion added to both subunits. Based on the previous studies,[111] Mg^{2+} was inserted in the center of an active site such that it was equidistant (2.8 Å) from E111 (one of the carboxylate oxygens), D91 (one of the carboxylate oxygens), A112 (main-chain carbonyl) and the scissile phosphate GpAATTC (O1P). The Cu^{2+} ion was inserted near the N_ε (1.7 Å) of H114 in one subunit (either A or B) or both subunits.

Electrostatic potential calculations: Electrostatic potentials were calculated by using DelPhi v.5.[131,132] Input coordinate files for the DelPhi calculations were generated from snapshots of multiple parallel molecular dynamics simulations (see above) of the EcoRI–DNA complex (i) in the absence of Mg^{2+}; (ii) with one Mg^{2+} added to either active site A or B; (iii) two Mg^{2+} added to both active sites; (iv) both active sites A and B filled with Mg^{2+}, and a Cu^{2+} ion added to one subunit; (v) both active sites A and B filled with Mg^{2+}, and a Cu^{2+} ion added to both subunits. The region inside the volume enclosed by the molecular surface of the protein–DNA complex was assigned a dielectric constant of 4.[133] The surrounding solvent was treated as a continuum with dielectric constant of 80.[133] An ion exclusion layer of 2 Å was assigned to the surface of the

macromolecules. A salt concentration of 0.145 M was used in the calculation. The first calculation stage (Coulombic boundary conditions) used a scale of 2.0 grids/Å, with 35% fill of a cubic lattice of 449 to 483 points per edge in various structures. The second calculation stage (focusing boundary conditions) used a scale of 3.2 grids/Å, with 81% fill of a cubic lattice of 311 to 317 points per edge in various structures. The potential was considered to have converged (after 3000 iterations) when its maximum value changed less than 0.00018 kT/e between successive iterations. Calculated electrostatic potentials of the molecular surface were displayed using the PyMOL program.[134]

Details of **sample preparation, equilibrium binding studies, cleavage kinetics and isothermal titration calorimetry (ITC)** are given in reference 7.

3.3 RESULTS AND DISCUSSION

***ESEEM and HYSCORE indicate that Cu^{2+} coordinates to histidine residue(s) in the EcoRI-DNA complex*:** The CW-spectrum from the Cu^{2+}-EcoRI-DNA complex is shown in Figure 3-1a. There are two distinct components, and the best-fit simulated spectrum (black dotted lines, Figure 3-1a) is obtained when the ratio of these two components is ~1:1. The $g_{||}$ and $A_{||}$ values are within the range of type-II Cu^{2+} complexes,[20] indicating that both Cu^{2+} components have four equatorial ligands. The $g_{||}$ and $A_{||}$ values of the first component are consistent with either one, two or three nitrogen ligands, with oxygens providing the remaining ligands in the equatorial plane.[20] The second component has smaller $g_{||}$ and $A_{||}$ values, which are not consistent with any known equatorial coordination structures of type II Cu^{2+} complexes.[20] Based on MD simulation results (see below), we propose that these anomalous $g_{||}$ and $A_{||}$ values may be attributed to some

distortion in the planarity of the four equatorial ligands.[135] Details of the differences between the two Cu^{2+} components will be discussed later and in Chapter 4.

To further characterize the Cu^{2+} coordination, we obtained a three-pulse ESEEM spectrum at a magnetic field that corresponds to the $g_{\perp}$ region of the Cu^{2+} ESR spectrum. At this magnetic field, both Cu^{2+} components contribute to the ESEEM signal. The ESEEM spectrum in Figure 3-1b has two sharp peaks at ~0.60 MHz and ~1.60 MHz, and one broad shoulder peak at ~1.09 MHz. The sum of the two lower frequencies is close to the highest one, indicating that they are mainly due to the nuclear quadrupole interactions of a weakly coupled ^{14}N.[23,27,136] Both the quadrupole parameters derived from these frequencies (e^2Qq/h ~1.73 MHz and η ~0.69)[136] and the three peaks in the ESEEM spectrum are typical of remote, non-coordinated ^{14}N from a histidine imidazole ring bound to Cu^{2+}.[23,27,28,30,32,34,35] Broad peaks at ~4.0 MHz are also resolved as shown in Figure 3-1b. These peaks may arise from the double quantum transition of ^{14}N.[27] Figure 3-1c shows the hyperfine sublevel correlation (HYSCORE) spectrum of the Cu^{2+}-EcoRI-DNA complex at the same magnetic field as ESEEM, which contains a cross-peak around (1.6 MHz, 4 MHz). This peak is due to the correlation between the ^{14}N NQI and double quantum transitions for the noncoordinating nitrogen of histidine imidazole ring. This observation supports the assignment that all the peaks at ~4.0 MHz in the ESEEM spectrum are from the double quantum transition of the remote nitrogen atom of a coordinating histidine.[28,32] The diagonal peak at 14.3 MHz in the HYSCORE spectrum is from weakly coupled protons around the Cu^{2+} electron spin. These protons may come from either the solvent or the protein/DNA.

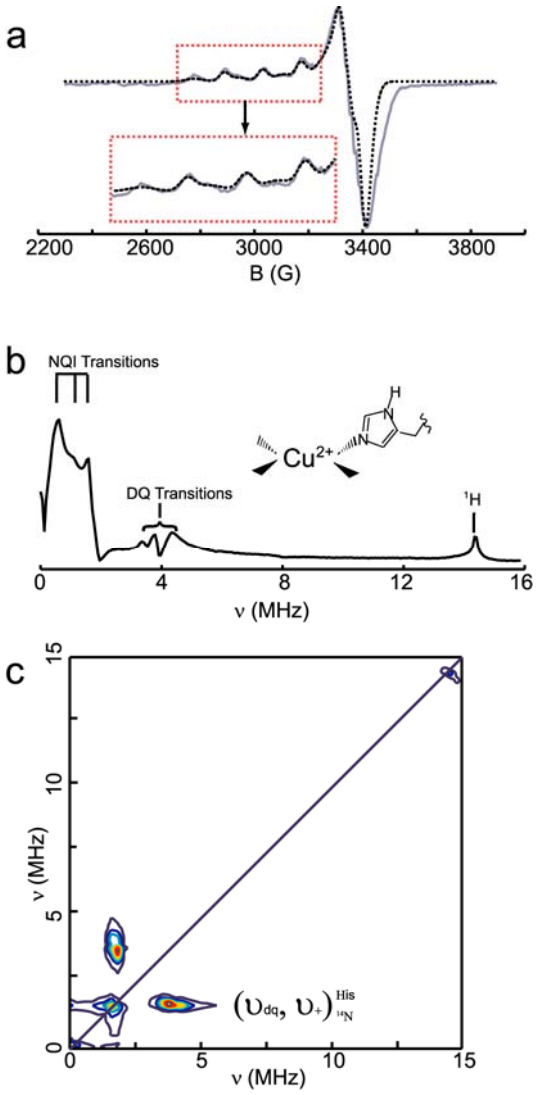

Figure 3-1. ESR data on the Cu^{2+} bound EcoRI–DNA complex. *(A)* The CW-ESR spectrum at 80 K (grey solid line) shows two components. The second component is clear in the magnified section of the spectrum, which is shown in the inset. The simulated spectrum is shown by the dark dotted line. The best-fit simulation was obtained with the following parameters: component 1: $g_{\|}$ = 2.289, $A_{\|}$ = 163 G, $g_{\perp}$ = 2.06, $A_{\perp}$ = 20 G and component 2: $g_{\|}$ = 2.228, $A_{\|}$ = 143 G, $g_{\perp}$ = 2.06, $A_{\perp}$ = 20 G. The relative ratio of the two components is ~1:1. *(B)* The three pulse ESEEM spectrum at 20 K obtained at a magnetic field of 3369 G. The peaks between 0-2 MHz, indicated by the trident, are assigned to the imidazole ^{14}N from a histidine residue. The broad peaks at ~4.0

MHz are assigned to the double quantum transition. The peak at ~ 14.3 MHz is assigned to the proton ESEEM peak. (Inset) The Cu^{2+} coordination derived from the ESEEM results. *(C)* HYSCORE spectrum of the Cu^{2+}-bound EcoRI–DNA complex. A set of broad cross-peak centered at ~4.0 MHz and ~1.6 MHz was observed. This peak appears from the correlation between the ^{14}N NQI and double quantum transition of the non-coordinating nitrogen atom of a histidine. The diagonal peak at ~14.3 MHz is from weakly coupled ^{1}H.

***Identification of the Cu^{2+} coordinated histidine residue(s) in the EcoRI-DNA complex*:** The ESEEM and HYSCORE results both clearly indicate that Cu^{2+} coordinates to histidine residue(s) in the EcoRI-DNA complex. There are five His residues in each subunit of EcoRI, at positions 31, 114, 147, 162 and 225. We employed a triangulation strategy based on the measurement of distance distributions to identify the specific histidine residue(s) that binds to Cu^{2+} in the EcoRI–DNA complex. All distance distributions were obtained by Dr. Zhongyu Yang.[137]

First, to narrow the possible Cu^{2+}-coordinated histidine residue(s), we obtained Cu^{2+}-Cu^{2+} distance distribution on wild type EcoRI-DNA by DEER-ESR and compared the result to the metal free crystal structure. Figure 3-2a shows the Cu^{2+}-Cu^{2+} DEER signal and the distance distribution function. By fitting the time domain data, a single most probable Cu^{2+}-Cu^{2+} distance at ~35 Å, with a standard deviation of 1 Å was observed. When compared to the metal free crystal structure, symmetrical binding at H31 (N_ε-N_ε 69 Å) and H147 (N_ε-N_ε 10 Å) are plainly excluded. H114 N_ε-H114 N_ε (33 Å), H162 N_ε-H162 N_ε (32 Å) and H225 N_ε-H225 N_ε (28 Å) remain as the only possibilities consistent with the DEER data. Binding to two histidines in the same monomer of EcoRI is intrinsically unlikely because of the symmetric homodimer structure.[110]

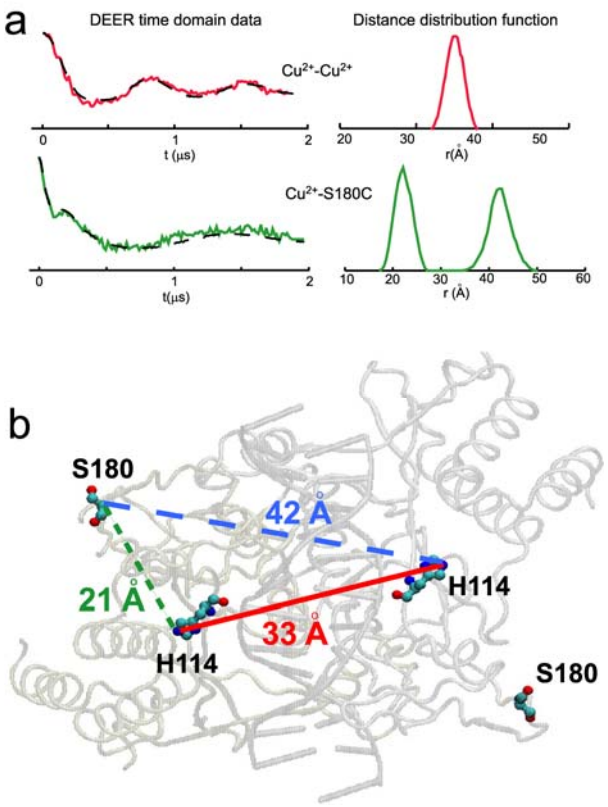

Figure 3-2. (a) DEER data on wild type and Ser180Cys mutant EcoRI protein. Cu^{2+}–Cu^{2+} and Cu^{2+}–nitroxide distance distributions are shown on the right. (b) The H114 N_ε-H114 N_ε distance (red solid line), S180 C_α-H114 N_ε intra (green dotted line) and inter monomer (blue dashed line) distances from the crystal structure of metal free EcoRI-DNA complex (PDB ID 1CKQ).[110] The distances from ESR experiments, overlaid on the structure of EcoRI, are consistent with Cu^{2+} binding to H114.

Second, to provide additional constraints for the triangulation, we mutated S180 to Cys, and labeled it with a nitroxide methanethiolsulfonate spin label (MTSSL).[13] Then we selectively measured the Cu^{2+}-nitroxide distance.[137] Figure 3-2b shows that by fitting the time domain data, two most probable distances at 22 Å and 42 Å, with standard deviation of 2 Å and 3 Å, respectively, were observed. Compared to the crystal structure, these distances from DEER experiments are uniquely consistent with Cu^{2+} binding to H114.

***Mutation and Isothermal titration calorimetry (ITC) results prove the Cu^{2+}-H114 coordination from ESR spectroscopy*:** Figure 3-3 shows the dependence of protein-DNA binding affinity on Cu^{2+} concentration and ITC titration of $CuCl_2$ into sample cell containing EcoRI and DNA. These data were collected by Dr. Linda Jen-Jacobson's group.

Interestingly, Figure 3-3a shows that in the presence of Cu^{2+}, the protein-DNA binding affinity increases by ~8 fold. This increase in binding affinity can be attributed to the fact that divalent metal ions can decrease the charge repulsion between protein and DNA.[111,138,139] In the H114Y mutant EcoRI, the stimulation by Cu^{2+} is almost completely abolished. The apparent dissociation constant for Cu^{2+} in the H114Y EcoRI is 8 mM, while in the wild type EcoRI, the apparent dissociation constant for Cu^{2+} is 5.1 ± 0.8 μM. The large change in the apparent dissociation constant of Cu^{2+} in the H114Y EcoRI confirms the Cu^{2+}-H114 coordination found in ESR spectroscopy.

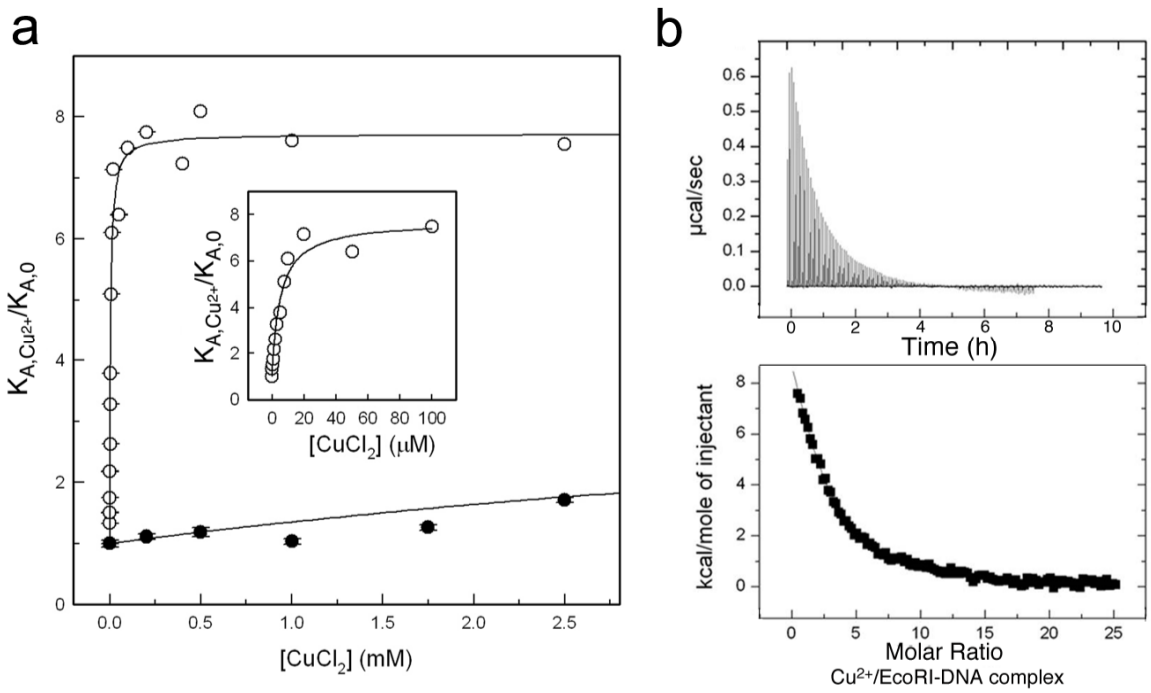

Figure 3-3. Interaction of Cu^{2+} with the EcoRI–DNA complex. (a) Cu^{2+} enhancement of EcoRI binding to cognate duplex TCGCGAATTCGCG (recognition site underlined). Ratio of K_A (plus Cu^{2+}) to K_A (no Cu^{2+}) is plotted for wild type EcoRI (empty circle) and H114Y (solid circle) enzymes; data show means ± std. dev. for at least 3 determinations at each [$CuCl_2$] or at least 6 determinations without Cu^{2+}. For wild type EcoRI, $K_{A,0}$ (no Cu^{2+}) = 1.2(± 0.1)×10^9 M^{-1}; $K_{A,Cu^{2+}}$ (max) = 9.3(± 0.3)×10^9 M^{-1}. For the promiscuous H114Y that shows better binding affinity than wild type EcoRI [140], $K_{A,0}$ = 1.7 (± 0.1)×10^{10} M^{-1} and $K_{A,\,Cu^{2+}}$(max) = 7.3(± 2.1)×10^{10} M^{-1}. Fit to the Hill equation $K_{A,\,Cu^{2+}} = K_{A,\,Cu^{2+}\,(max)}\,[Cu^{2+}]^n / (K_{D\ 0.5,\,Cu^{2+}} + [Cu^{2+}]^n)$ gives Hill coefficient n = 1.0 ± 0.15 and $K_{D\ 0.5,\,Cu^{2+}}$ = 5.1 ± 0.8 μM. Inset shows the hyperbolic binding isotherm of wild type EcoRI for [Cu^{2+}] from 0 to 100 μM. (b) Representative ITC titration of $CuCl_2$ (1 mM) into sample cell (15°C) containing EcoRI (9 μM) and DNA (20 μM). Top panel shows heat signals obtained for 125 injections (2.5 μL each). Lower panel shows integrated heat signal normalized to moles of Cu^{2+} injected (after subtraction of heats of dilution of Cu^{2+}) per mole of

EcoRI–DNA complex. The stoichiometry value n = 2.0 ± 0.3 and K_D value of 14 ± 6 μM (means ± std. dev. of at least 3 determinations at 10°C, 15°C, 21°C) did not vary with temperature or buffer identity (imidazole or TRIS; see Methods for buffer compositions).

The single Cu^{2+}-Cu^{2+} distance and only two Cu^{2+}-nitroxide distances from DEER-ESR suggest that only one Cu^{2+} binds to each EcoRI subunit. To confirm this conclusion, we determined stoichiometry by calorimetric measurement of binding. Figure 3-3b shows the ITC results by titrating Cu^{2+} into a solution of wild type EcoRI-DNA complex. The data showed a stoichiometry of 2.0 ± 0.3 Cu^{2+} bound per EcoRI-DNA molecule. This result thus confirmed the inference from ESR experiments that only one Cu^{2+} coordinates to each subunit of EcoRI dimer.

MD simulation suggests Cu^{2+} coordinates to N_ε of H114 in the EcoRI–DNA complex: Based on the triangulation procedure from the DEER experiment, we identified that H114 coordinates to Cu^{2+}. This is also strongly supported by biochemical studies, which show that the mutant H114Y-DNA complex binds to Cu^{2+} with a 1600-fold lower affinity than the wild type EcoRI-DNA complex.

There are two N atoms (N_δ and N_ε) in the histidine imidazole ring. Although both of the two nitrogen atoms can be the candidate for the Cu^{2+} coordination, in a single histidine, N_δ is more likely to coordinate to Cu^{2+} than N_ε is.[141] Whether the N_δ or N_ε coordinates to Cu^{2+} in the protein structure may depend on the particular local structure. In order to distinguish between N_δ or N_ε coordination, we carried out a series of parallel MD simulations with Cu^{2+} ion added to both subunits of the EcoRI–DNA complex near the N_δ or N_ε of H114.

Figure 3-4 shows the Cu^{2+}-Cu^{2+} distance distributions constructed from 4 × 10 ns parallel MD trajectories with Cu^{2+}-H114 N_δ coordination. These simulations yield a most probable Cu^{2+}-Cu^{2+} distance between 27 and 28 Å with a standard deviation ~0.4 Å.

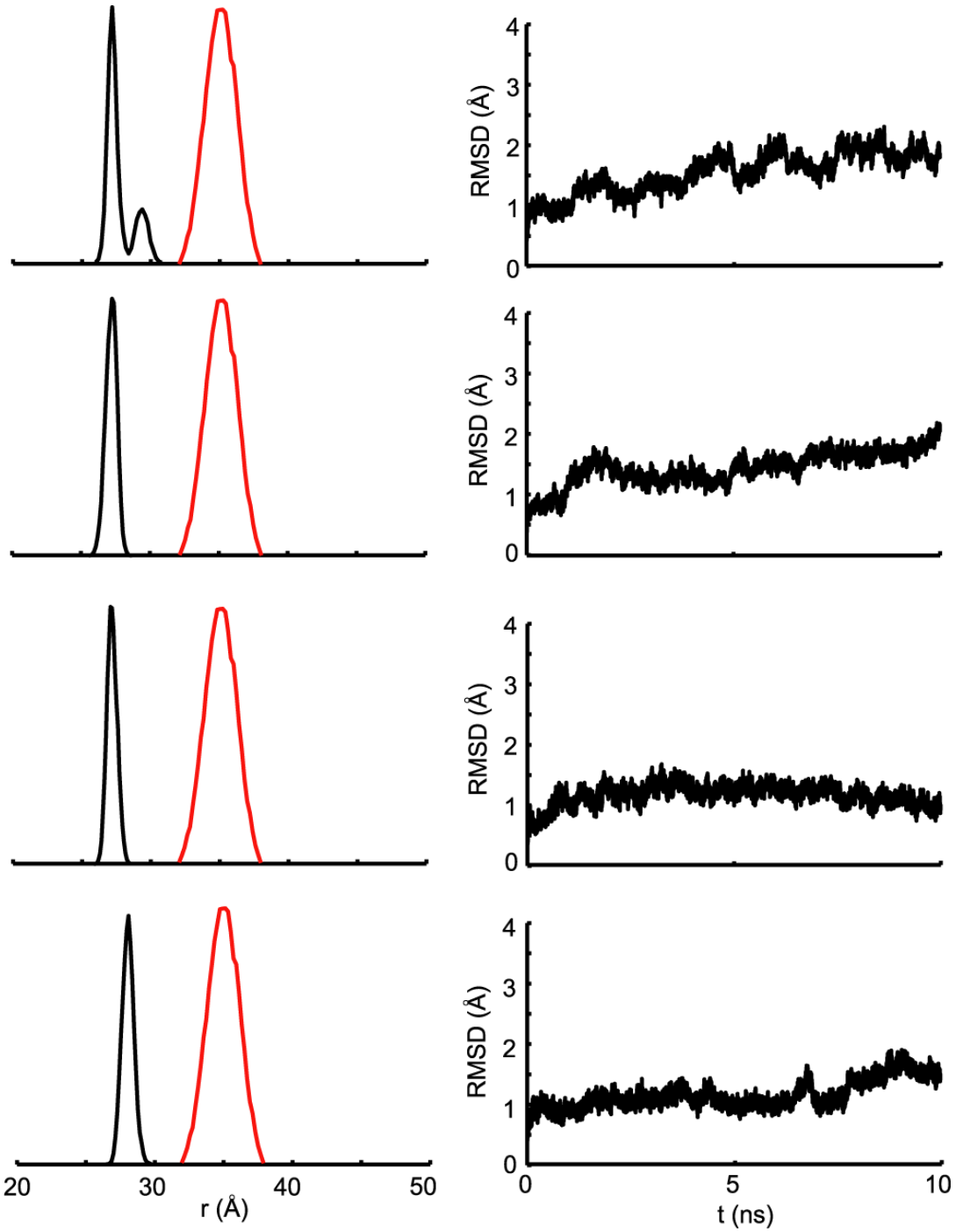

Figure 3-4. Comparison of the Cu^{2+}-Cu^{2+} distance distribution from experiment (red)[7] and MD simulation (black) (Cu^{2+}-N_{δ} His114 coordination). Left panel: The local backbone RMSD trajectories from different parallel MD simulations.

Figure 3-5 shows the Cu^{2+}-Cu^{2+} distance distributions constructed from 4 × 10 ns MD simulations with Cu^{2+}-H114 N_ε coordination. These simulations shows a most probable Cu^{2+}-Cu^{2+} distance between 34 and 38 Å with a standard deviation ~0.5 Å. The local backbone root mean square deviations (RMSD) of the Cu^{2+} binding sites and ~30 surrounding residues in all these simulations are also shown in Figure 3-4 and 3-5. Compared to the Cu^{2+}-Cu^{2+} distance distribution (red solid line in Figure 3-5 and Figure 3-6) from DEER experiments, simulations with Cu^{2+}-N_ε coordination provides a more consistent Cu^{2+}-Cu^{2+} distance distribution.

Figure 3-6 shows the local coordination environment of Cu^{2+} from MD simulations (4 to 5 parallel simulations for Cu^{2+}-N_δ and N_ε coordination with at least 2 ns MD run). Clearly, when Cu^{2+} coordinates to H114 N_δ, it interacts with the DNA phosphate GApATTC directly. When Cu^{2+} coordinates to H114 N_ε, it lies at ~10 Å away from the phosphate GApATTC. Previous research showed that in the EcoRI-DNA complex, the competitive inhibitor Ca^{2+} interacts with the DNA phosphate GpAATTC directly.[111] The existence of Ca^{2+} increases the protein-DNA equilibrium association constant (K_A) as much as 380-fold, which is due to the large decrease in negative charge repulsion between protein and nearby DNA phosphates.[111] Compared to Ca^{2+}, the 8-fold increase in the protein-DNA binding affinity with the presence of Cu^{2+}, as shown in Figure 3-3a, suggests that Cu^{2+} should not have a direct interaction with the DNA backbone. All these results suggest that Cu^{2+} coordinates to H114 N_ε.

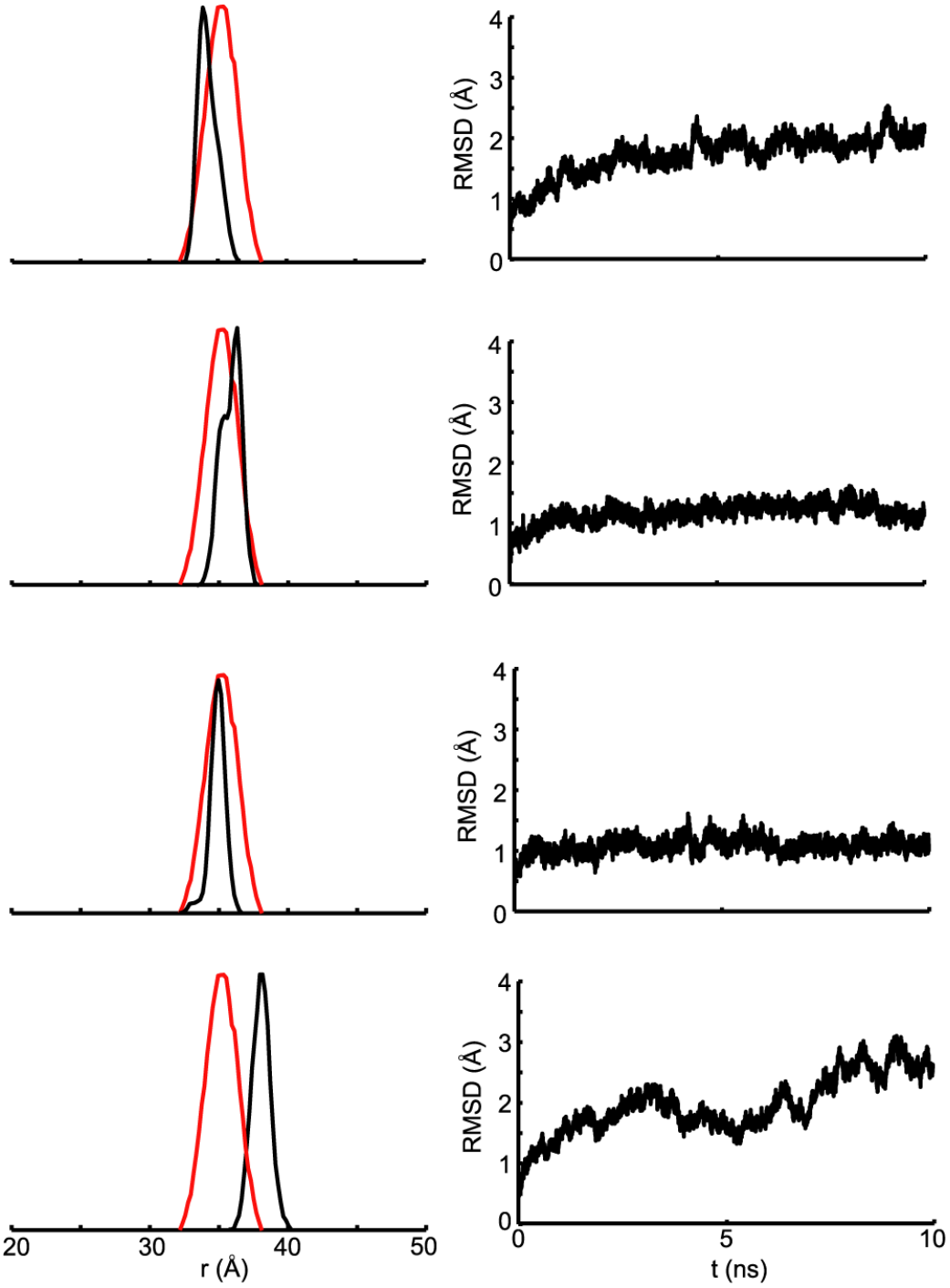

Figure 3-5. Comparison of the Cu^{2+}-Cu^{2+} distance distribution from experiment (red)[7] and MD simulation (black) (Cu^{2+}-N_{ε} His114 coordination). Left panel: The local backbone RMSD trajectories from different parallel MD simulations.

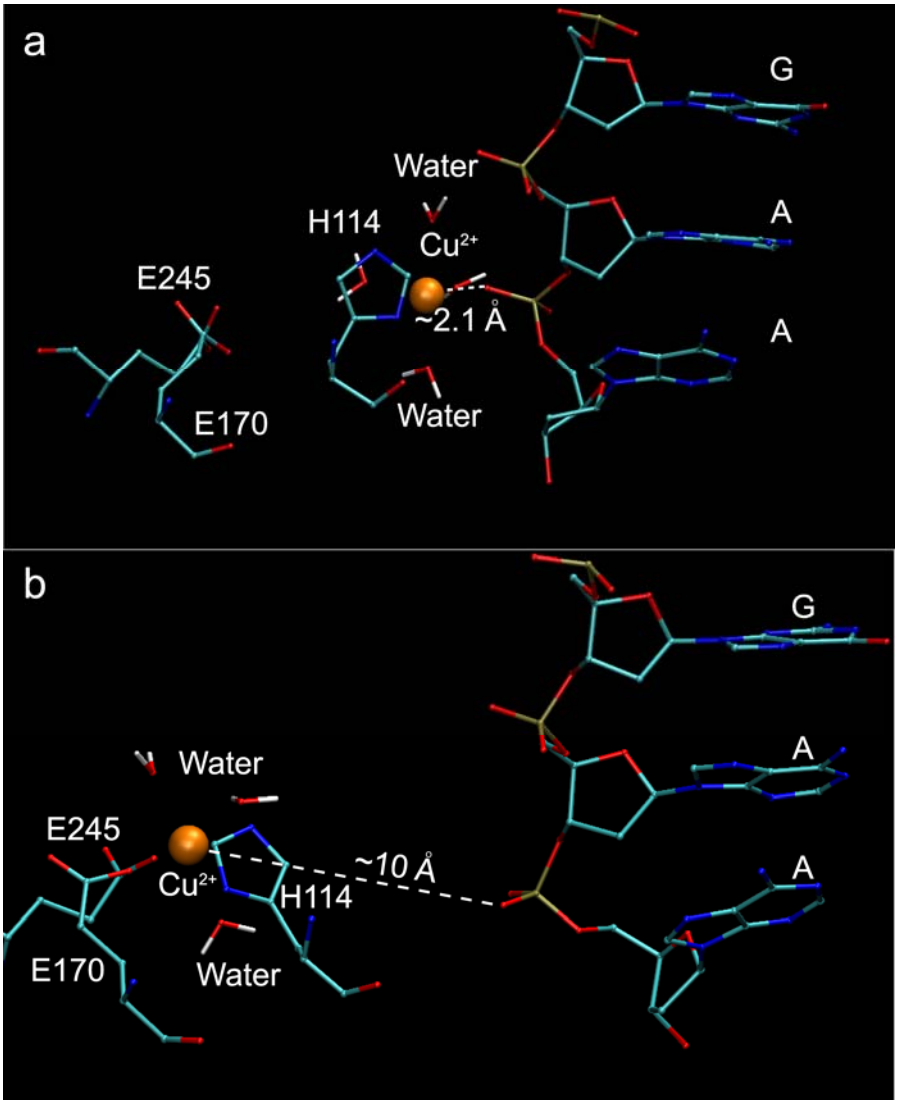

Figure 3-6. Cu^{2+} local coordination environment from series MD simulations. (a) Cu^{2+}-H114 N_δ coordination. (b) Cu^{2+}-H114 N_ε coordination. Cu^{2+} interacts with the GApATTC directly when it coordinates to N_δ. Cu^{2+} lies at greater distance from the nearest DNA phosphate GApATTC when it coordinates to N_ε.

With the insertion of Cu^{2+} into the EcoRI-DNA complex near H114 N_ε position, MD simulation with explicit solvent show that Cu^{2+} is coordinated to H114 N_ε, carboxyl oxygen of E170 and E245. The simulation results suggest that the transient rotation of the sidechain of E170 and E245 allows both the carboxylate oxygens coordinate to Cu^{2+}. This side chain rotation can create the distortion in the planarity of the equatorial ligands and may cause the observation of abnormal small $A_{||}$ and $g_{||}$ values of the second Cu^{2+} component in the CW-ESR spectrum.

Cu^{2+} inhibits Mg^{2+}-dependent catalysis. Based on all the ESR spectroscopy and biochemical experimental results, we found that Cu^{2+} binds to H114, a site distinct from that where Mg^{2+} binds.[111] Figure 3-7 shows the cleavage rate constant detection results from Dr. Jen-Jacobson's group, which clearly indicate that Cu^{2+} is a powerful inhibitor of Mg^{2+}-dependent DNA cleavage by wild type EcoRI: 100 μM Cu^{2+} completely inhibits catalysis by wild type EcoRI. In this detection, molar excess of enzyme over DNA was used. Thus, Cu^{2+} must affect the chemical step rather than the protein-DNA association or product release. Strikingly, in the H114Y mutant EcoRI, even at 200 μM, Cu^{2+} does not inhibit Mg^{2+}-catalyzed cleavage. This result further confirms our previous results that H114 is the Cu^{2+}-coordination site. The inhibition behavior is unexpected because Cu^{2+} does not bind directly to the catalytic site.

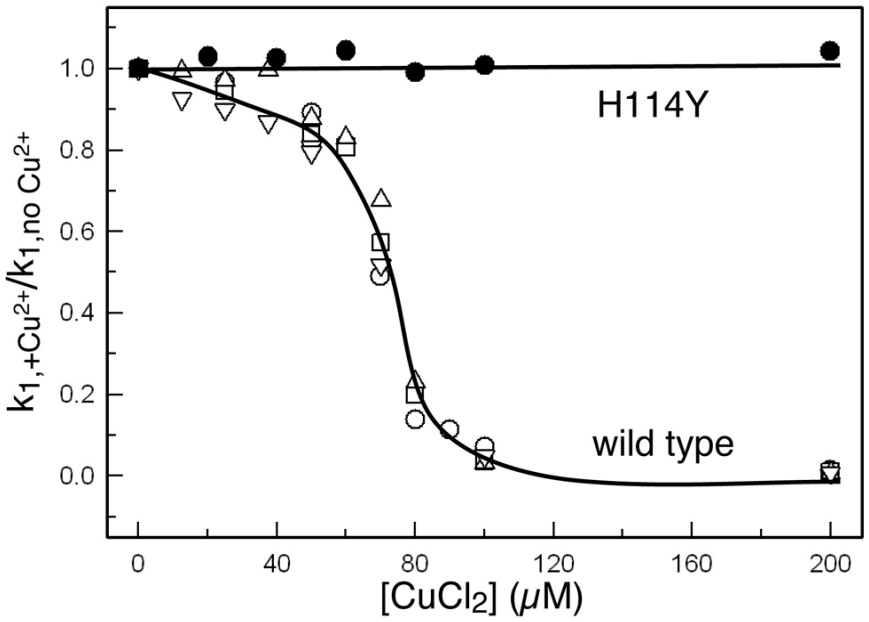

Figure 3-7. Inhibition of EcoRI cleavage by Cu^{2+}. Ratio of first order cleavage rate constant $k_{cleave}(+Cu^{2+})/k_{cleave}(\text{no } Cu^{2+})$ as a function of [$CuCl_2$]. Wild type EcoRI cleavage reactions were performed at Mg^{2+} concentrations 3 mM (upside down triangle), 4 mM (empty triangle), 6 mM (empty square), and 8 mM (empty circle); His114Tyr reaction was at 8 mM (solid circle). Plots for k_1 (cleavage in top strand) and k_2 (cleavage in bottom strand) were precisely superimposable. For clarity, only k_1 data are shown. Each point represents the mean of at least 3 determinations. Error bars are too small to be seen at this scale.

In order to understand the mechanism of Cu^{2+} inhibition, we carried out series MD simulations of the EcoRI-DNA complex in the presence of Mg^{2+} in two active sites, with or without Cu^{2+}. Figure 3-8a shows the catalytic site structure from series of MD simulations with only the existence of Mg^{2+} in the wild type EcoRI-DNA complex. In this local structure, H114 forms a hydrogen bond to the phosphate at GApATTC. This phosphate helps the orientation of a water (named W_C in Figure 3-8a), which hydrogen bonds to the Mg^{2+}-bound water (W_A) that makes the nucleophilic attack on the scissile phosphate. Studies with chiral phosphate analogs[111] implied that the precise positioning of the phosphoryl oxygen at GApA that participates in this "water relay" (W_C) structure is important for the cleavage. This configuration is thus an example of what Bruice and Benkovic have termed a "near attack conformer".[142]

Figure 3-8b demonstrates the local structure from the detailed MD simulations with explicit water molecules when one Cu^{2+} is inserted near N_ε of H114 in the EcoRI•DNA•$(Mg^{2+})_2$ complex. The H114 imidazole ring rotates to a position in which Cu^{2+} coordinates to H114-N_ε, E170 and E245, as shown in Figure 3-8b. Under this condition, H114 imidazole ring is ~4 Å away from its normal position (in the case without Cu^{2+}). This movement eliminates the interaction between GApATTC and His114 N_δ as well as the interaction between W_C and H114 N_ε, which helps the certain conformation of GApATTC and position of W_C to support the water network. Crucially, the water relay (W_C) from the GApA to W_A is no longer in stable form. From series of parallel MD simulations, the occupancy of water at W_C position drops from 98-100%, with average residence time between 300 ps to 500 ps in the absence of Cu^{2+}, to 20-40% and with average residence time less than 100 ps in the presence of Cu^{2+}. The overall picture is the critical conformation ("near attack conformer") for catalysis no longer exists in the Cu^{2+}-containing EcoRI•DNA•$(Mg^{2+})_2$ complex.

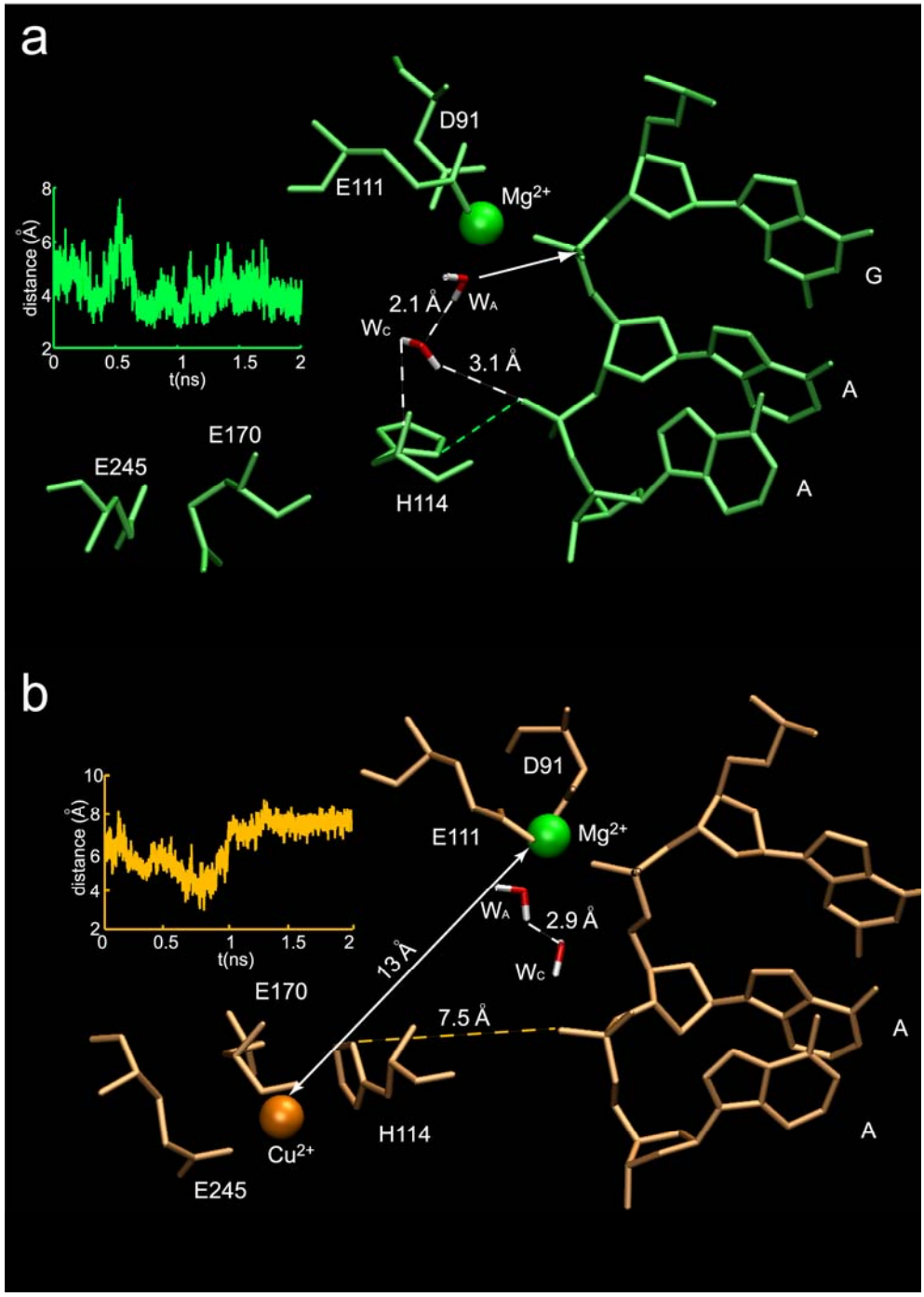

Figure 3-8. Simulations of Cu^{2+}-induced structural changes in the catalytic site of the EcoRI-DNA complex. (a) In the complex without Cu^{2+}, a water molecule, W_A, coordinated to Mg^{2+} carries out the nucleophilic attack (shown by the white arrow) at the scissile phosphate GpAATTC. This water is hydrogen-bonded to the stable "relay water" W_C, which is precisely

positioned by H-bonding to phosphate GApATTC, while H114-N_δ H-bonds to the phosphate GApATTC. The distance trajectory from the first 2 ns MD simulation of the distance between H114-N_δ and oxygen of GApATTC is shown in the inset. (b) With the coexistence of Mg^{2+} and Cu^{2+}, H114 and GApATTC assume completely different positions and there is no stable equivalent of W_C. The distance trajectory from the first 2 ns MD simulation of the distance between H114-N_δ and oxygen of GApATTC is shown in the inset.

Cooperative Mg^{2+} interactions in the two catalytic sites. To fully understand Cu^{2+} effects in catalysis, we reinvestigated the interaction of Mg^{2+} with the EcoRI-DNA complex. EcoRI is generally considered to use only one Mg^{2+} in each catalytic site.[110,117,118] Based on the crystal structures[110] and MD simulation results[111], Mg^{2+} coordinates to one phosphoryl oxygen (O1P) at the scissile GpAA, carboxylate oxygen from D91 and E111. The remaining phosphoryl oxygen (O2P) at the scissile phosphate site hydrogen-bonds to the positively charged sidechains of K113 and R145. These hydrogen bonds stabilize the phosphorane transition state and/or the oxyanion leaving group.[111] Thus the side chains of K113 and R145 mimic the functional role of the second metal ion proposed for many two-metal-ion phosphotransferase reactions, such as EcoRV, which uses two Mg^{2+} at each catalytic site.

Figure 3-9 shows the dependence of the cleavage rate constants on Mg^{2+} concentration (data collected and analyzed by Dr. Jen-Jacobson's group). Fitting of the first order cleavage rate constants to the Hill equation, $k_{cleave} = k_{max}[Mg^{2+}]^n/(K_{Mg^{2+}}+[Mg^{2+}]^n)$, yields values of Hill coefficient n = 1.9 ± 0.1 and n = 1.8 ± 0.1 for cleavage of each of the two DNA strands. This data implies positive cooperativity between the two Mg^{2+} binding sites which is ~20 Å away from each other (n > 1, positive cooperativity; n < 1, negative cooperativity; n = 1, no cooperativity).

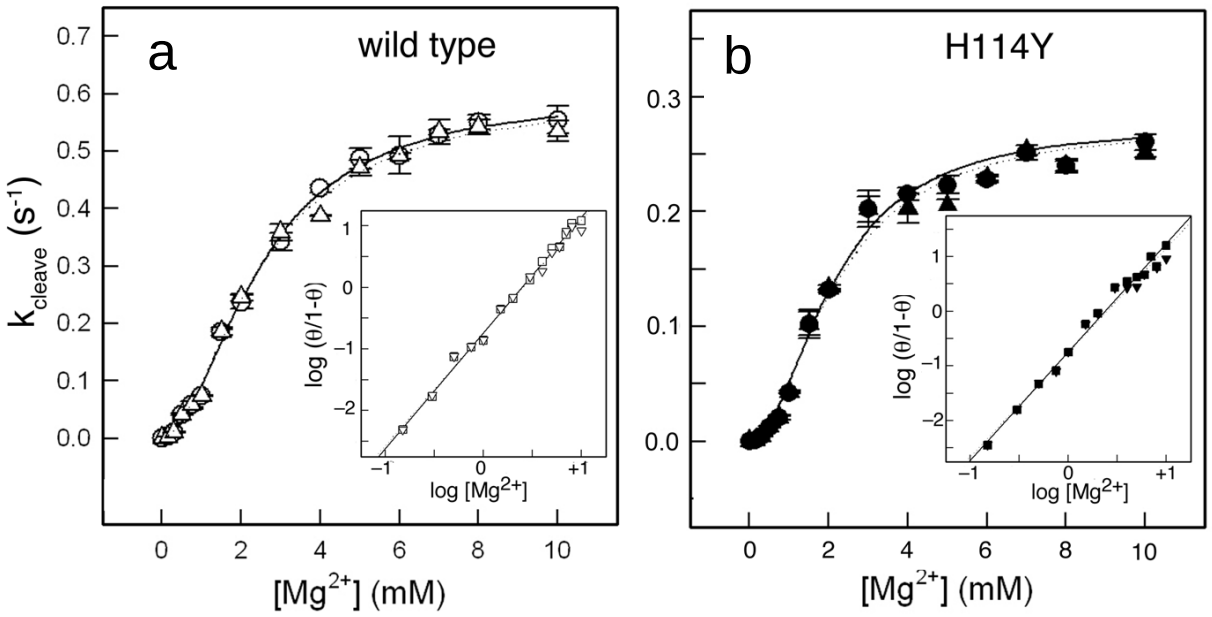

Figure 3-9. Dependence of single-turnover cleavage rate constants on Mg^{2+} concentration**.** Y-axis (k_{cleave}) represents first order rate constants k_1 (empty circle) or k_2 (empty triangle) for cleavage of the distinguishable top and bottom DNA strands (Materials & Methods). Data were fit to the Hill equation (see text). (a) The apparent affinities for Mg^{2+} are $K_{0.5,Mg^{2+}}$ = 2.4 ± 0.1 mM for wild type, measured for both k_1 and k_2 and (b) $K_{0.5,Mg^{2+}}$ = 2.2 ± 0.2 mM for H114Y enzyme. For wild type EcoRI, Hill coefficient n values were 1.9 ± 0.1 (k_1) and 1.8 ± 0.1 (k_2) and for H114Y, n values were 2.0 ± 0.3 (k_1) and 1.9 ± 0.3 (k_2). Each point is the mean ± std. dev. of at least 3 determinations.

Mg^{2+} cooperativity reflects long-range electrostatic interactions In order to explain the cooperativity behavior, we carried out a series of MD simulations of the EcoRI-DNA complex (i) with one Mg^{2+} added to either catalytic site A or B; (ii) two Mg^{2+} added to both catalytic sites. In previously MD studies,[111] it had been observed that the existence of Mg^{2+} at the catalytic site caused movements of the sidechains of residues D91, E111 and K113. The carboxyl side chains of D91 and E111 rotate to coordinate to Mg^{2+} and K113-N_ε moves to form a stable hydrogen bond with O2P of scissile phosphate GpAATTC at ~2.7 Å (~5 Å away from O2P of GpAATTC in metal free crystal structure).

Figure 3-10 shows the N_ε-O2P distance trajectories. In the case without the existence of Mg^{2+}, the most probable distance between K113-N_ε and O2P of GpAATTC in both catalytic sites is ~4.3 Å as shown in Figure 3-10a. In the simulation with only one Mg^{2+} placed at one of these two catalytic sites, we observed the expected movement of K113 sidechain at the Mg^{2+} exist site. The distance between K113-N_ε and O2P of scissile phosphate GpAATTC is at ~2.7 Å as shown in Figure 3-10b and c. Very interestingly, the distance trajectories shown in Figure 3-10b and c also indicate a similar movement of the K113 side chain in the Mg^{2+}-free site. A hydrogen bond interaction with the scissile phosphate GpAATTC was formed with a most probable distance at ~2.7 Å, which suggests that the existence of the first Mg^{2+} may have certain effects on the second catalytic site at a considerable distance ~20 Å.

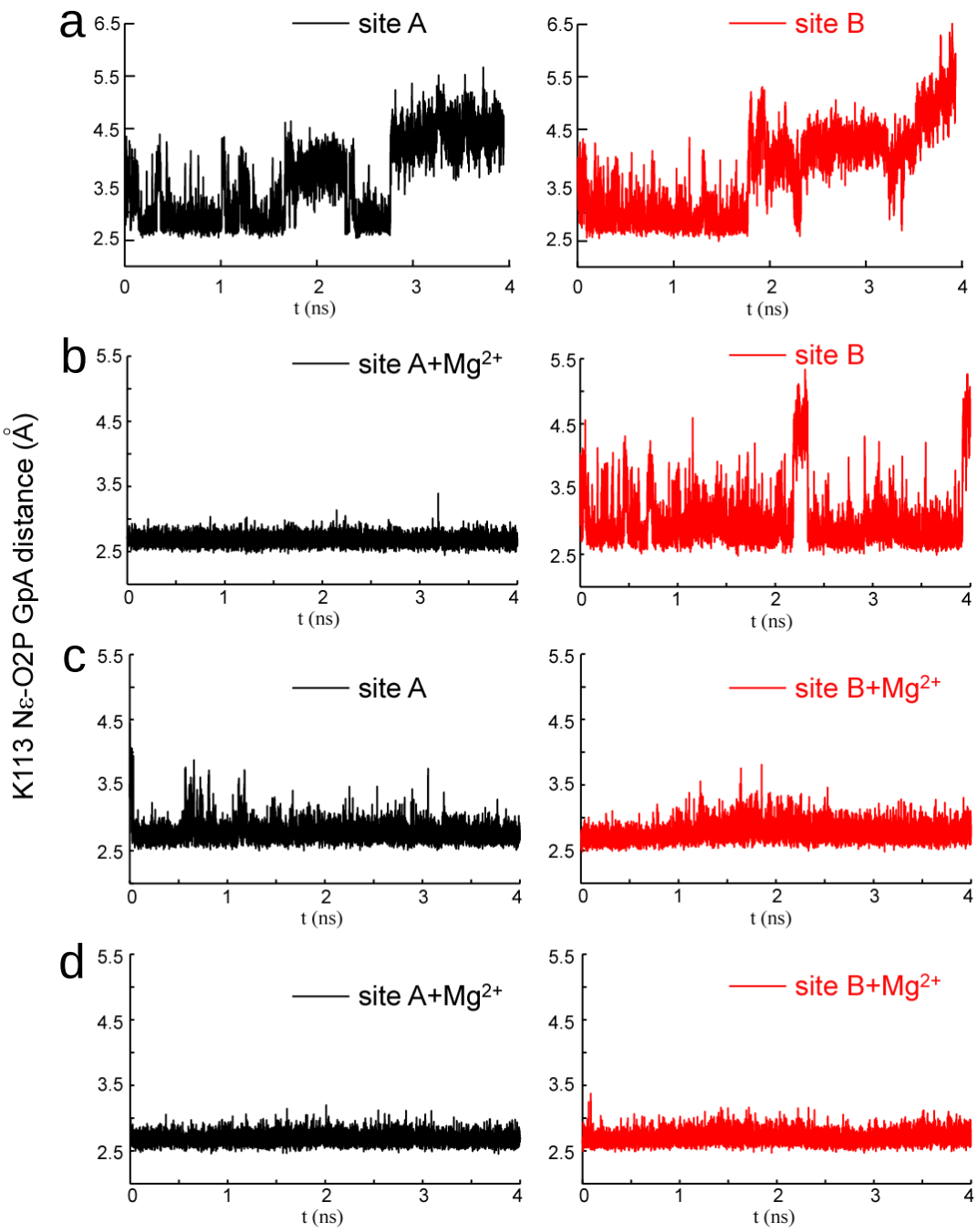

Figure 3-10. K113 N_{ε}-O2P distance trajectories at two sites in the EcoRI-DNA complex. (a) wild type EcoRI-DNA complex. (b) wild type EcoRI-DNA complex with one Mg^{2+} in active site A. (c) wild type EcoRI-DNA complex with one Mg^{2+} in active site B. (d) wild type EcoRI-DNA complex with two Mg^{2+} in both active sites.

It has been shown that the surface electrostatic potential in macromolecules plays a central role in a variety of biological processes.[143-145] The electrostatic potential not only depends on the locations of charged groups, but also on the shape of the molecular surface. The regions with remarkable negative potential could potentially be defined as a significant metal ion binding site.[146] With the purpose of understanding the cooperativity between two catalytic sites, we used the DelPhi program[131,132] to calculate the surface electrostatic potentials of these non-Mg^{2+}, single-Mg^{2+} and double-Mg^{2+} EcoRI-DNA complexes. Different snap shots from MD simulation were chosen to use as the input coordinates file for the calculations (see methods part).

Figure 3-11 shows the electrostatic potential of the protein-DNA molecule with and without Mg^{2+}. Not surprisingly, the site with the existence of Mg^{2+} has a more positive electrostatic potential compared to the site with no Mg^{2+}, since the Mg^{2+} neutralizes the negative potential at its binding site. More strikingly, the calculation results shown in Figure 3-11b and c clearly indicate that the potential over a large region surrounding the Mg^{2+}-free active site ~20 Å away from the site with Mg^{2+} becomes pronouncedly more negative than it was in the metal-free complex (Figure 3-11a).

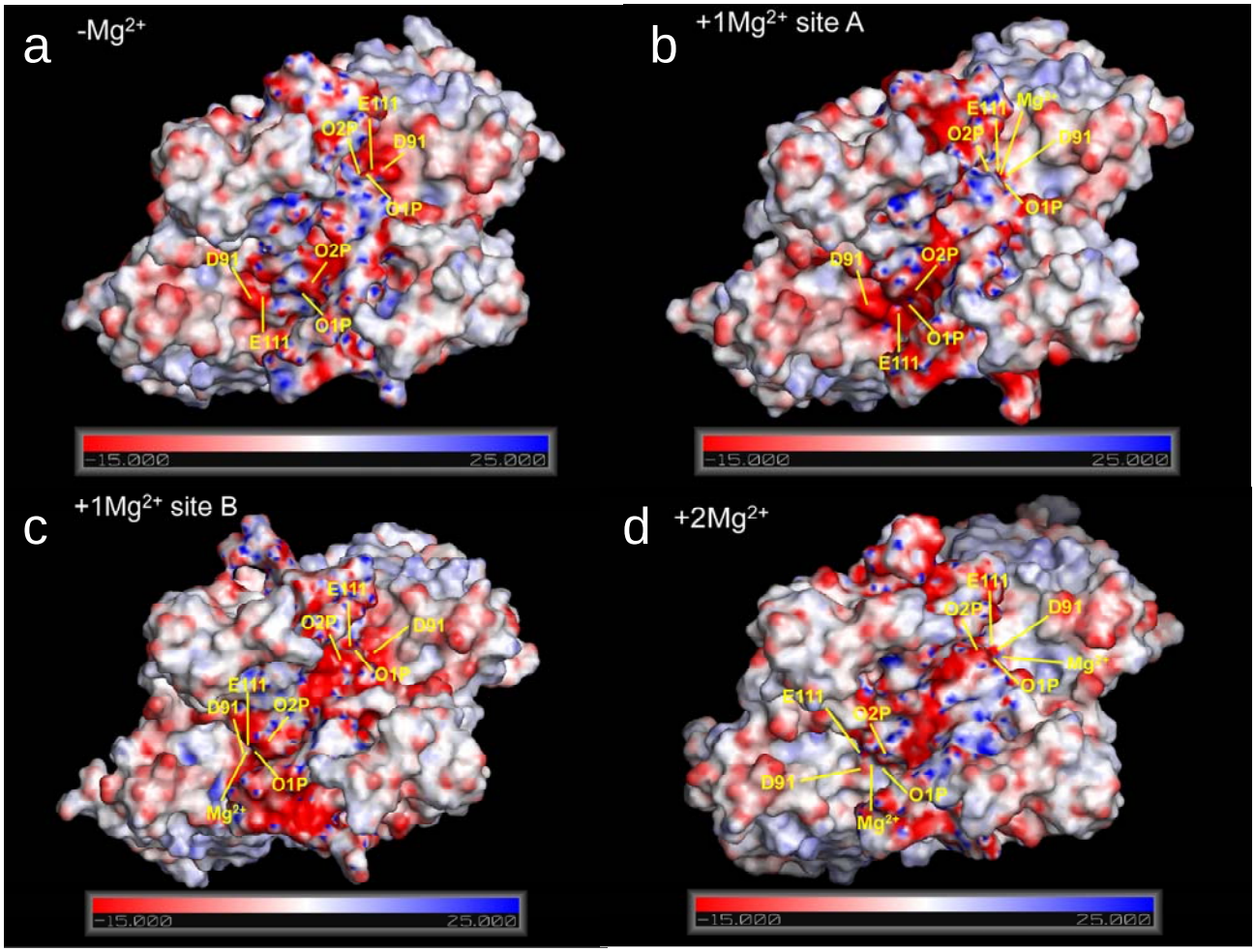

Figure 3-11. Effect of Mg^{2+} in one of two catalytic centers of the EcoRI-DNA complex on surface electrostatic potentials. Electrostatic potentials of structures from snapshots of MD simulations were calculated with the DelPhi program, mapped to the molecular surfaces and visualized in PyMOL for the complex without Mg^{2+} (a), with a Mg^{2+} inserted in only catalytic site (b and c) and two Mg^{2+} inserted in each catalytic site (d). Electrostatic potentials are graded continuously from red (-15 kT/e) to white (0 kT/e) to blue (+25 kT/e). Mg^{2+} is coordinated by D91-OD1/OD2, E111-OE2, O1P-GpAATTC, the attacking nucleophilic water (not shown) and A112-carbonyl and/or a transiently visiting water.

At the Mg^{2+}-free catalytic site (the Mg^{2+} binding position without existence of Mg^{2+}) in the EcoRI-DNA complex with one Mg^{2+} in the catalytic site A, the electrostatic potential changes by about -20 kT/e compared to the case with no Mg^{2+} in the structure (Table 3-1). By placing one Mg^{2+} in the opposite catalytic site, again the Mg^{2+}-free catalytic site shows a more negative electrostatic potential to nearly the same extent as Mg^{2+} in the other active site (Table 3-1). All these observations indicate that binding of the first Mg^{2+} in one catalytic site causes a formation of a negative electrostatic "trap" in the other Mg^{2+}-free site. This negative electrostatic "trap" will enhance binding of the second Mg^{2+} and produce positive cooperativity in the EcoRI-DNA complex, which is consistent with the experimental observations. This positive cooperativity in Mg^{2+} binding would tend to promote double-strand DNA cleavage instead of single strand cleavage, as required for restriction endonucleases to introduce double-strand breaks into foreign DNA.

Table 3-1. Electrostatic potentials in simulated models of the EcoRI-DNA, EcoRI-DNA-$(Mg^{2+})_1$ and EcoRI-DNA-$(Mg^{2+})_2$ complexes

Mg^{2+} in Model	Potential at Site A (kT/e)	Potential at Site B (kT/e)
None	–18	–15
Site A	(Mg^{2+}) -134	–34
Site B	–35	(Mg^{2+}) -149
Both site	(Mg^{2+}) -139	(Mg^{2+}) -137

These data are the means of electrostatic potential values calculated with the finite-difference Poisson-Boltzmann method (DelPhi v.5, see Materials and Methods) using multiple snapshots from parallel MD simulations for each model. The potential is given at a "dummy atom" position corresponding to that which would be occupied by Mg^{2+} if it were present, measured from the alpha carbons of D91 and E111 and the O1P of the phosphate at GpAATTC. The variation in calculated potential between parallel runs was ≤10%. Electrostatic potential values did not change in focusing runs with different final resolution scales (2.0 grids / Å or 3.2 grids / Å).

3.4 SUMMARY

X-band ESR results established that Cu^{2+} ions coordinate to H114 in EcoRI. This is strongly supported by biochemical studies that the H114Y mutation abolished the effect of Cu^{2+} on both DNA binding and cleavage. MD simulations suggest that upon Cu^{2+}-binding at H114, the position of the H114 side is altered. Consequently, critical protein-DNA interactions are disrupted, which possibly leads to inhibition of catalysis. The Mg^{2+}-dependence of EcoRI catalysis shows positive cooperativity. Detailed MD and electrostatic potential calculations suggest this cooperativity arises because the binding of Mg^{2+} at one catalytic site makes the electrostatic potential at the other site more negative. This positive cooperativity helps ensure a double strand DNA cut instead of single strand nicks.

3.5 ACKNOWLEDGEMENT

This work was supported by a National Science Foundation (MCB 0842956) grant and the Center for Simulation and Modeling at the University of Pittsburgh.

4.0 INSIGHTS INTO COPPER COORDINATION IN THE ECORI-DNA COMPLEX BY ESR SPECTROSCOPY

This work, written in collaboration Linda Jen-Jacobson and Sunil Saxena, is in preparation for submission.

4.1 INTRODUCTION

Restriction endonucleases, which are found in bacteria, digest foreign DNA to protect bacterial cells from bacteriophage infection.[147] Type II restriction endonucleases are of great interest because they recognize a very specific DNA sequence and cleave the DNA at this sequence with a very high specificity. As a type II restriction endonuclease, EcoRI is a 62 kDa homodimer. It scans DNA with a scanning rate of ~7×10^6 bp/s,[147] and recognizes and binds to a specific 5'-GAATTC-3' sequence of DNA.[114,116] Upon binding Mg^{2+}, EcoRI cleaves DNA at the scissile phosphate site GpAATTC with an extremely high specificity.[110,111,114] With one base pair difference, the cleavage rate can decrease by as much as 10^6 fold.[110,111,114]

It is of significant interest to determine the number of metal ions involved in catalysis, how the metal ions catalyze the cleavage and whether the binding of metal ions is cooperative, in order to understand the role of metal ions in DNA cleavage by endonucleases.[7,109-111,117,118] The

EcoRI homodimer with its GAATTC DNA site has two catalytic centers.[110,111] In each center, one Mg^{2+} coordinates to carboxylate side chains of E111, D91 and the scissile phosphate of GpAATTC.[110,111] The catalytic rates of different divalent metal ions vary according to the sequence $Mg^{2+} \approx Mn^{2+} > Co^{2+} >> Zn^{2+} >> Cd^{2+} > Ni^{2+}$.[109,117] On the other hand, Ca^{2+} can act as an inhibitor by competing with Mg^{2+}.[111] A possible Mg^{2+} catalytic mechanism has been proposed based on stereospecific phosphate studies and molecular dynamics simulations.[111] In this model, a water relay between a downstream phosphate and the active site, distortion in the conformation of DNA and certain interactions between EcoRI and DNA are critical factors that affect the catalysis.[111]

Cu^{2+} does not catalyze the DNA cleavage by EcoRI. Remarkably, in previous work, we found that Cu^{2+} profoundly inhibits the Mg^{2+}-dependent catalysis. We previously used ESR spectroscopy and Molecular Dynamics (MD) simulations to clarify the functional difference between Cu^{2+} and Mg^{2+}, as well as the structural and electrostatic factors that affect the site-specific catalysis in this enzyme.[7] Based on a novel use of Cu^{2+}-based distance constraints, we identified that Cu^{2+} binds to H114 in the EcoRI-DNA complex.[7] We proposed that this binding disrupts critical protein-DNA interaction and also the water relay, leading to inhibition of Mg^{2+}-catalyzed cleavage.[7] However, in that study, only Cu^{2+}-H114 coordination was confirmed by experimental results. The identity of other ligands was inferred from MD simulations. We also found that Cu^{2+} binds to EcoRI in two distinct components with different g_{zz} and A_{zz} values. Given the important role of Cu^{2+} in modulating the enzyme function, we examine the Cu^{2+} coordination in more detail in this work.

Herein we present the application of W-band Electron Nuclear Double Resonance (ENDOR) spectroscopy, as well as X-band Electron Spin Echo Envelope Modulation (ESEEM)

experiments to clarify further details of Cu^{2+}-coordination in the EcoRI-DNA complex. W-band ENDOR experiments provide the direct evidence of the existence of equatorially coordinated water molecules. The possible structural similarity between the two Cu^{2+} components in this protein-DNA complex is also discussed based on X-band ESEEM results.

4.2 METHODS

Enzyme expression and purification. The EcoRI protein was expressed from a maltose-binding protein-EcoRI (MBP-EcoRI) fusion construct. Details for generation of the fusion gene and expression of the fusion protein are given in supporting information of our previous research.[7] The EcoRI protein was isolated, purified, and characterized as described in reference.[148]

Cu^{2+}-EcoRI–DNA complex preparation. A solution of EcoRI (5 μM) in the presence of fivefold molar excess of TCGCGAATTCGCG was exchanged into 30 mM N-ethylmorpholine (NEM) buffer, which contains 0.3 M NH_4Cl, 10% dioxane, 30% deuterated glycerol (d8), 65% D_2O (pH 8.0) and concentrated. The final concentrations of EcoRI and DNA were 380 μM and 1.5 mM, respectively. Isotopically enriched $^{63}CuCl_2$ (Cambridge Isotope Labs, Inc) was added at a 4:1 molar ratio (Cu^{2+} : protein dimer). The sample was stored at -80°C and flash-frozen before each ESR experiment.

Spectroscopic measurements. X-band ESR experiments were performed on a Bruker Elexsys 580 spectrometer. W-band ESR experiments were performed on a Bruker Elexsys 680 spectrometer. All the pulse experiments were performed at 20 K.

The X-band three pulse ESEEM signals were collected by recording the stimulated electron spin echo intensity as a function of T using the pulse sequence $\pi/2$-τ-$\pi/2$-T-$\pi/2$-τ-echo.

The π/2 pulse length was 16 ns. The interpulse delay τ varied at different magnetic fields in order to suppress the ^{1}H ESEEM signal. The τ values at different magnetic fields are: 166 ns at 2810 G, 154 ns at 3050 G, 152 ns at 3116 G, 148 ns at 3189 G and 140 ns at 3369 G. The initial *T* was incremented from 400 ns with a stepsize of 16 ns, for a total of 1024 points. A four step phase cycle was used to eliminate unwanted signals.[121] The resulting time domain signals were baseline subtracted by using a polynomial fit.

The Davies ENDOR experiments were performed using the pulse sequence π1-T-π/2-τ-π-τ-echo with an rf pulse applied during T. The π1 pulse length was 256 ns, π/2 pulse length was 16 ns and π pulse length was 32 ns, rf pulse length was 10 μs. The interval T was 13 μs, τ was 600 ns. The Mims ENDOR experiment was performed using the pulse sequence π/2-τ-π/2-T-π/2-τ-echo with an rf pulse applied during T. For the Mims ENDOR experiments of Cu^{2+}-EcoRI-DNA sample in H_2O, the length of the π/2 pulse was 28 ns, and the rf was 25 μs. τ = 128 ns, T = 50 μs. For the Mims ENDOR experiments of Cu^{2+}-EcoRI-DNA sample in D_2O, the length of the π/2 pulse was 16 ns, and the rf was 10 μs. τ = 200 ns, T = 13 μs. The frequency scale of the ^{2}H Mims ENDOR spectra was multiplied by a factor 6.5144 ($\gamma^{\mathbf{H}}/\gamma^{\mathbf{D}}$) to allow a direct comparison with the ^{1}H ENDOR spectra. The frequency scale of the ^{1}H ENDOR spectra is shown with respect to the proton Larmor frequency, ν_{RF}-ν_L(^{1}H).

ENDOR spectrum simulation. The ENDOR spectra were simulated by the GENDOR 50 program from Hoffman's group, which is free of charge and can be downloaded at http://chemgroups.northwestern.edu/hoffman/endor_files/simulationprograms.htm.

ESEEM simulations. For computation in the case of Cu^{2+}–^{14}N ESEEM signal, the Hamitonian used to describe the system is:

$$\hat{H} = \beta\vec{B}\cdot\vec{\vec{g}}\cdot\hat{S} - g_n\beta_n B_0\hat{I}_z + \hat{S}\cdot\vec{\vec{A}}\cdot\hat{I} + \hat{I}\cdot\vec{\vec{Q}}\cdot\hat{I} \qquad (4\text{-}1)$$

where β is Bohr magneton, $\hat{S}$ and $\hat{I}$ are the electron spin and nuclear spin operators, $\vec{g}$, $\vec{A}$ and $\vec{Q}$ are the *g*-tensor of electron, hyperfine tensor and nuclear quadrupole tensor. The relative orientation of the *g*-tensor and external magnetic field was described by two angles θ and ϕ. The relative orientation of the principal axis system (PAS) of Cu^{2+} *g*-tensor and the *Q*-tensor, as well as the orientation of the PAS of *g*-tensor and *A*-tensor were described by six Euler angles, ($\alpha 1$,$\beta 1$,$\gamma 1$), ($\alpha 2$,$\beta 2$,$\gamma 2$) (Figure 4-1).

The variables to be optimized in the model are the hyperfine tensor *A*, the nuclear quadrupole tensor *Q*, the Euler angles describing the orientation of the PAS of *g*-tensor and *A*-tensor, as well as the orientation of the PAS of *g*-tensor and *Q*-tensor. The *g*-tensor is obtained from the CW-ESR spectrum, and the nuclear quadrupole tensor can be estimated from the ESEEM data.

The three NQI transitions of ^{14}N in the ESEEM spectrum are given by:[26]

$$\nu_{-} = \frac{e^2qQ(3-\eta)}{4h};\ \nu_0 = \frac{2\eta e^2qQ}{4h};\ \nu_{+} = \frac{e^2qQ(3+\eta)}{4h} \tag{4-2}$$

where *e* is the electron charge, *q* is the electric gradient at the nuclear site, *Q* is the nuclear quadrupole moment, η is the asymmetry parameter, *h* is Planck′s constant. The three principal components of the quadrupole *Q* tensor relate to the asymmetry parameter η and the quadrupole coupling constant e^2Qq/h: $\eta=(Q_x-Q_y)/Q_z$, $e^2Qq/h=2I(2I-1)Q_z$, where I is the nuclear quantum number. Therefore, the three Q-tensor principal values can be estimated from the X-band ESEEM spectra directly.

The principal values of the *A*-tensor were estimated based on literature values.[28,149,150] The robustness of the optimized variables was further tested by fitting ESEEM spectra at five different external magnetic fields.

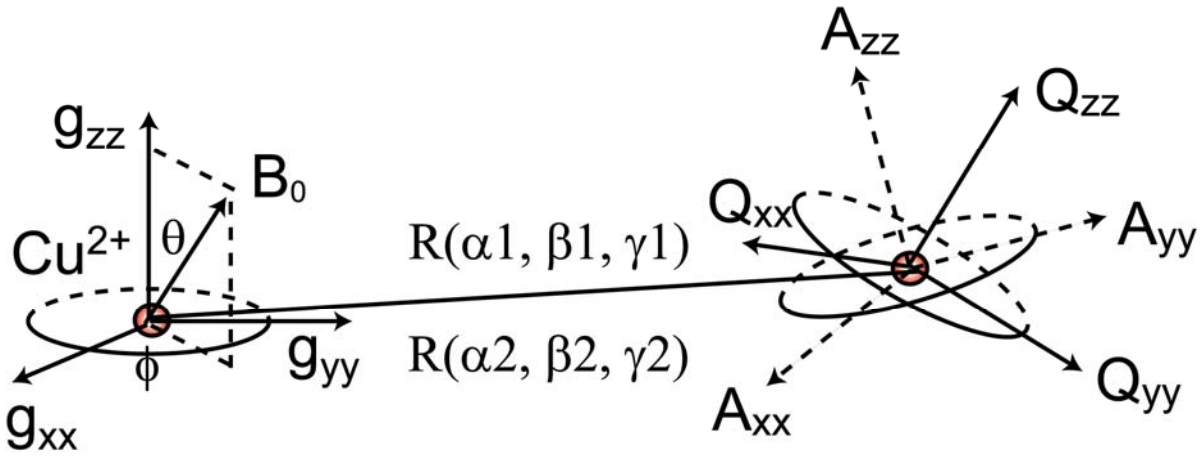

Figure 4-1. The definition of the relative orientation between external magnetic field and PAS of *g*-tensor, PAS of *A*-tensor and *g*-tensor, PAS of *Q*-tensor and *g*-tensor. The relative orientation between external magnetic field and PAS of *g*-tensor is described by θ and ϕ. The relative orientations between the PAS of *Q*-tensor and *g*-tensor, as well as the PAS of *A*-tensor and *g*-tensor are described by two sets of Euler angles ($\alpha 1$,$\beta 1$,$\gamma 1$) and ($\alpha 2$,$\beta 2$,$\gamma 2$), respectively.

4.3 RESULTS AND DISCUSSION

W-band Field-Swept Electron Spin Echo (FS-ESE) Spectrum confirms the existence of the two Cu^{2+} components. Figure 4-2a shows the W-band (~94 GHz) Field-Swept Electron Spin Echo (FS-ESE) spectrum (black solid line) and the simulation result (black dashed line). Two Cu^{2+} components with different g_{zz} and A_{zz} values were observed: component 1 (cp1) with g_{zz} = 2.289, $g_{xx} = g_{yy}$ = 2.055, A_{zz} = 163 G; component 2 (cp2) with g_{zz} = 2.227, g_{xx} = 2.072, g_{yy} = 2.035, A_{zz} = 143 G. In order to clearly distinguish the two components, we also shows the first derivative of the FS-ESE spectrum in Figure 4-2b. The W-band data showed a much higher resolution than the X-band data.[7] The A_{zz} values of cp1 and cp2 are consistent with the results observed at X-band (~9.5 GHz)[7] and within the range of type II Cu^{2+} complex,[17] indicating that both components have four equatorially coordinated ligands. The unequal g_{xx} and g_{yy} values of cp2 may be attributed to the distortion of the planarity of the equatorial coordinated ligands.[7] Since the axially coordinated ligands have a small impact on the *g*-tensor,[20] the difference of the *g*-tensor principal values in the two components suggests either different types of equatorially coordinated ligands or different bond lengths and angles among these ligands and Cu^{2+} center.[20,21]

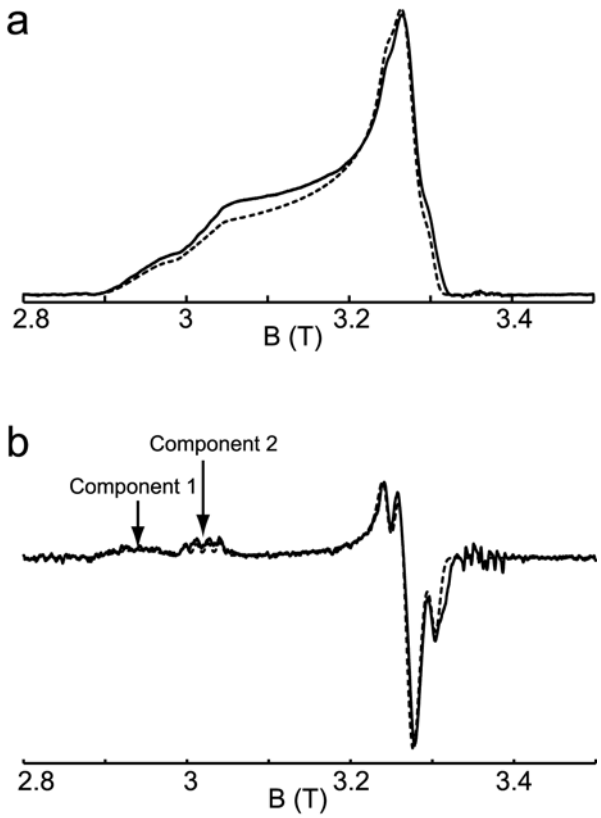

Figure 4-2. (a) The experimental (black solid line) and simulated (black dashed line) W-band (~94 GHz) FS-ESE spectrum of the Cu^{2+}-EcoRI-DNA complex at 20 K; (b) The first derivative of the W-band FS-ESE spectrum in (a). Experimental result is shown by the black solid line and simulated result is shown by the black dashed line. The best-fit simulations were obtained with the following parameters: component 1: $g_{xx} = g_{yy} = 2.055$, $g_{zz} = 2.289$, $A_{xx} = A_{yy} = 20$ G, $A_{zz} = 163$ G and component 2: $g_{xx} = 2.072$, $g_{yy} = 2.035$, $g_{zz} = 2.227$, $A_{xx} = A_{yy} = 20$ G, $A_{zz} = 143$ G. The relative ratio of the two components is close to 1:1.

W-band ENDOR spectra prove the existence of equatorial coordinated water molecule. Based on extensive MD simulations, we had previously postulated that the N_ε from H114, carboxylate oxygen from E170 and E245, oxygen from a water molecule (W_e) form the equatorial coordination plane in component 1, as shown in Figure 4-3a.[7] On the other hand, we had proposed that the N_ε from H114, oxygens from two water molecules (W_{e1} and W_{e2}) form an equatorial coordination plane in component 2, as shown in Figure 4-3b.[7] The two carboxylate oxygens from E170 coordinate to Cu^{2+} at the same time. These two oxygens are not in the plane formed by the other three ligands. This observation may explain the abnormal *g*-tensor of cp2 in the EcoRI-DNA complex. Both proposed coordination environments have two axially coordinated water molecules (W_{a1} and W_{a2}).

In this work, we employ W-band ENDOR spectroscopy to prove the existence of the equatorially and/or axially coordinated water molecules. First, we measured ^1H ENDOR spectra of the Cu^{2+}-EcoRI-DNA complex in H_2O at different magnetic fields. Different types of ^1H atoms with different hyperfine values are observed. These hyperfine interactions give us information on the distance between ^1H atom and the Cu^{2+} center, which can help us identify the possible origin of these ^1H atoms in the protein-DNA complex. Second, we detected the ^1H ENDOR spectra of the Cu^{2+}-EcoRI-DNA complex exchanged with D_2O. The decrease in the intensity of ENDOR signals of solvent exchangeable protons helped in the assignment of peaks observed in ^1H ENDOR. Third, the existence of solvent exchangeable protons was confirmed by the scaled up ^2H ENDOR spectrum of the sample in D_2O.

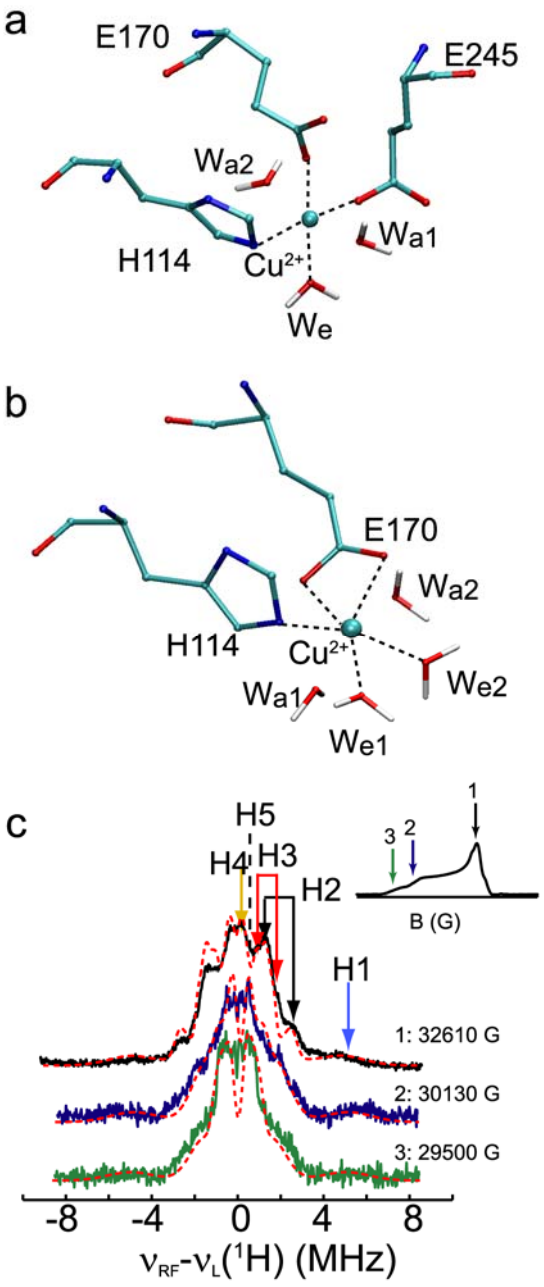

Figure 4-3. a) and b) Two postulated Cu^{2+} coordination environments from MD simulations; c) W-band ^{1}H Davies (32610 G) and Mims ENDOR (30130 G and 29500 G) spectra in H_2O and corresponding simulation spectra (red dashed line). Five types of protons designated as H1 to H5 with different hyperfine interactions are observed. Inset is the W-band field-swept electron spin

echo (FS-ESE) spectrum of the Cu^{2+}-EcoRI-DNA complex. The magnetic fields at which the ENDOR data were collected are indicated by arrows in the inset.

Figure 4-3c shows the W-band ^{1}H Davies and Mims ENDOR obtained at three different magnetic fields: 32625 G, 30130 G, 29500 G (shown by arrows inset) for the Cu^{2+}-EcoRI-DNA complex in H_2O.

At 32625 and 30130 G, both components contribute to the ENDOR signals. At 29500 G, only cp1 contributes to the ENDOR signal. The two spectra at the higher magnetic fields consist of a relatively broad doublet at ~±5.3 MHz and splittings below ~±2.5 MHz centered at the proton Larmor frequency, $\nu_L(^1H)$. Because of the low signal-to-noise ratio at the lowest magnetic field (29500 G), the relatively broad doublet at ~±5.3 MHz is hard to identify.

Simulations of these ^{1}H ENDOR spectra yielded five sets of hyperfine parameters as shown in Table 4-1. These five sets of hyperfine parameters are designated as H1 to H5, respectively, as shown in Figure 4-3b. The H5 signal can only be resolved at 29500 G because of the broadening of signals at the other two magnetic fields. Given the low signal-to-noise ratio, we do not further discuss the signals at 29500 G and 30130 G in the following sections. The isotropic hyperfine coupling constant A_{iso} and anisotropic hyperfine coupling constant T_{dip} are also shown in Table 4-1, which can be calculated based on the following relationship: $A_{xx} = A_{yy} = A_{iso} - T_{dip}$, and $A_{zz} = A_{iso} + 2T_{dip}$.[34]

Table 4-1. Hyperfine parameters of H1 to H5 obtained from the ^{1}H Davies ENDOR spectra.

	H1	H2	H3	H4	H5
A_{xx} (MHz)	-10.5	-3.1	-2.3	-0.7	-1.5
A_{yy} (MHz)	-10.5	-3.1	-2.3	-0.7	-1.5
A_{zz} (MHz)	12.5	5.2	3.5	1.0	2.2
A_{iso} (MHz)	-4.3	-1.0	-1.1	-0.13	-0.8
T_{dip} (MHz)	7.7	2.8	1.9	0.57	1.2

The hyperfine parameters of the strongly coupled H1 are in the expected range for the interaction of Cu^{2+} with the protons of equatorially bound water molecule(s).[151,152] Note that equatorial waters in both sites proposed based on MD simulations (We, Figures 4-3a and b). The hyperfine parameters of H2 and H3 are similar to the couplings of proton from water molecule(s) axially coordinated to the copper center.[28,151] However, protons from protein would also provide hyperfine parameters close to H2 and H3. In order to unambiguously identify the origins of these ^{1}H ENDOR signals, ^{1}H Davies ENDOR of the Cu^{2+}-EcoRI-DNA complex in D_2O was performed. Given the signal-to-noise ratio, we only performed ^{1}H and ^{2}H ENDOR experiments at 32610 G.

Figure 4-4 shows that the broad doublet with the splitting at ~±5.3 MHz disappears when the complex is exchanged in D_2O (blue solid line).

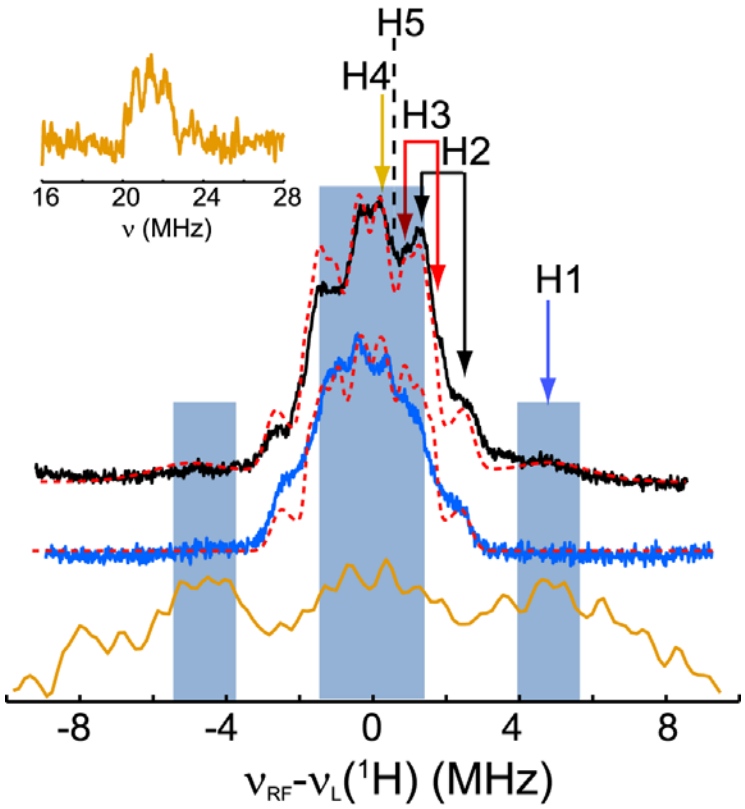

Figure 4-4. ^{1}H Davies ENDOR spectra of the Cu^{2+}-EcoRI-DNA sample in H_2O (black solid line) and D_2O (blue solid line) at 32610 G. The simulated spectra are shown by the red dashed line. The yellow solid line shows the scaled up ^{2}H Mims ENDOR spectrum. The inset is the unscaled ^{2}H Mims ENDOR spectrum.

This observation is unambiguously confirmed by the scaled up ^{2}H Mims ENDOR spectrum, which includes these missing peaks (Figure 4-4, orange solid line). These results verify that the broad doublet with the splitting at ~±5.3 MHz arises from the solvent exchangeable protons. This observation explicitly validates the existence of the equatorial bound water (We) in the Cu^{2+} coordination, since there are no other solvent exchangeable protons from the protein close to the Cu^{2+} center to provide the hyperfine parameters of H1.

Simulation of the ^{1}H ENDOR spectrum in D_2O shows that the relative intensity of the H2 signal decreased by about 45%, and the H4 signal decreased by about 15%, as shown in Figure 4-4. This clearly indicates that both H2 and H4 contain solvent exchangeable as well as non-exchangeable protons. Based on the hyperfine interaction parameters of H2, the solvent exchangeable H atoms that contribute to the H2 signal could originate from the axial coordinated water (Wa) molecule(s). However, based on our X-band ESEEM results (see below), the relatively strong interaction between H114 imidazole N_δ and Cu^{2+} yields a Cu^{2+}- $H(N_\delta)$ distance of ~3.3 Å. At this distance, the N_δ-H could also be the same of the H2 peak. This proton is also solvent exchangeable. Details will be discussed in the following section.

Using the point dipolar approximation, the distance between H4 and the Cu^{2+} center is ~5.2 Å. Thus we assign the exchangeable H4 signal to solvent water. The remaining non-exchangeable signal of H4 must be from the protein backbone. There is no alteration of the relative intensity of the H3 and H5 signals, which indicates the H3 and H5 signals come from the non-exchangeable protons of protein.

X-band ESEEM spectra indicate that both Cu^{2+} components have similar Cu^{2+}-histidine distance: In order to obtain detailed structural information of the two Cu^{2+} components, we employed X-band three pulse ESEEM experiments at different magnetic fields. Based on X-band CW-ESR spectrum,[7] the relative ratio of the two components at different magnetic fields is different. Figure 4-5 shows the ESEEM time domain data and spectrum (black solid line) at 2810 G, where only cp1 contributes to the ESEEM signal. In the spectrum, two sharp peaks at ~0.67 MHz and ~1.5 MHz, a broad shoulder peak at ~ 1.0 MHz, as well as a broad peak at ~3.5 MHz were observed. All these peaks are the characteristic transitions of the Cu^{2+} electron spin interacting with the remote ^{14}N nucleus. The peaks below 2 MHz are the typical nuclear quadrupole interaction (NQI) of the ^{14}N of histidine imidazole.[34,153-155] To obtain the detailed hyperfine and quadrupole interaction information, we simulated the ESEEM spectrum as shown in Figure 4-5 (red dashed lines). The ESEEM data are best-fit with asymmetric parameter $\eta=0.65 \pm 0.01$, the quadrupole coupling constant $e^2Qq/h=1.51 \pm 0.01$ MHz, $A_N=[1.1,1.1,2.5] \pm 0.1$ MHz, $(\alpha 1,\beta 1,\gamma 1) = (90°,30°,30°) \pm 5°$, $(\alpha 2,\beta 2,\gamma 2)=(30°,30°,35°) \pm 5°$, respectively. The ^{14}N-Cu^{2+} distance estimated based on point dipolar approximation from the hyperfine parameters is ~2.4 Å.[34] This distance indicates a relatively strong interaction between Cu^{2+} and the remote ^{14}N of histidine imidazole.

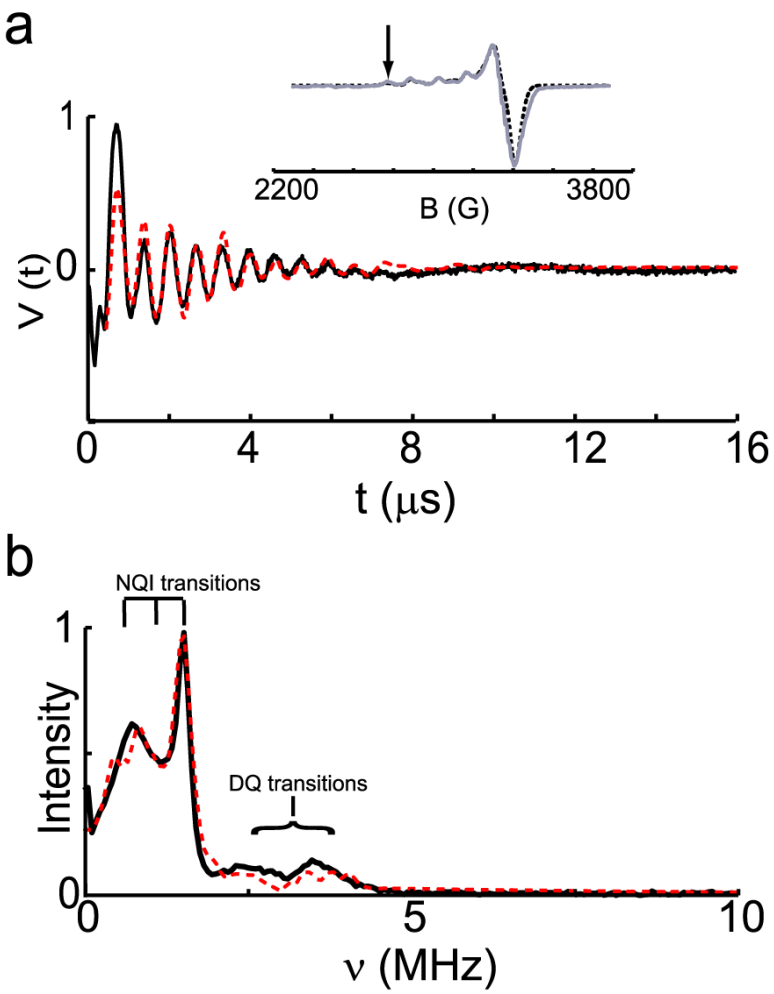

Figure 4-5. The experimental (black solid line) and simulated (red dotted line) three pulse ESEEM time domain data and spectrum of the Cu^{2+}-EcoRI-DNA complex at 2810G.

We have shown that Cu^{2+} coordinates to H114 in the EcoRI-DNA complex.[7] Due to the overlap of the two Cu^{2+} components in the ESR spectrum, we cannot obtain the ESEEM signal purely from Cu^{2+} cp2 at X-band. In order to get the detailed hyperfine and quadrupole parameters of ^{14}N of cp2, we collected ESEEM spectra at the four other magnetic fields, 3369 G, 3189 G, 3116 G and 3050 G, where both components contribute to the ESEEM signals. The ESEEM signal at these fields can be expressed by: $V=AV_1+BV_2$, where V_1 and V_2 are the ESEEM signals of Cu^{2+} cp1 and cp2, respectively. A and B are the relative ratios of the ESEEM signal from the two Cu^{2+} components at a certain external magnetic field. The values of A and B under different external magnetic fields can be estimated based on the CW-ESR spectrum at X-band.

Figures 4-6 a to h show the experimental ESEEM time domain data and spectra (black solid line) at 3369 G, 3189 G, 3116 G and 3050 G. Simulation results are shown as red dashed lines. These ESEEM spectra are best fit with following parameters for cp2: $\eta = 0.73 \pm 0.01$, the quadrupole coupling constant $e^2Qq/h = 1.51 \pm 0.01$ MHz, $A_N = [1.2,1.2,2.4] \pm 0.1$ MHz, $(\alpha 1,\beta 1,\gamma 1) = (85°,62°,85°) \pm 5°$, $(\alpha 2,\beta 2,\gamma 2) = (35°,45°,0°) \pm 5°$. The ^{14}N-Cu^{2+} distance estimated based on point dipolar approximation is ~2.5 Å, which is comparable to the ^{14}N-Cu^{2+} distance in cp1 (~2.4 Å). Poorer quality fits were obtained of only one component was assumed at these four magnetic fields. These simulations are shown in Figures 4-7 and 4-8.

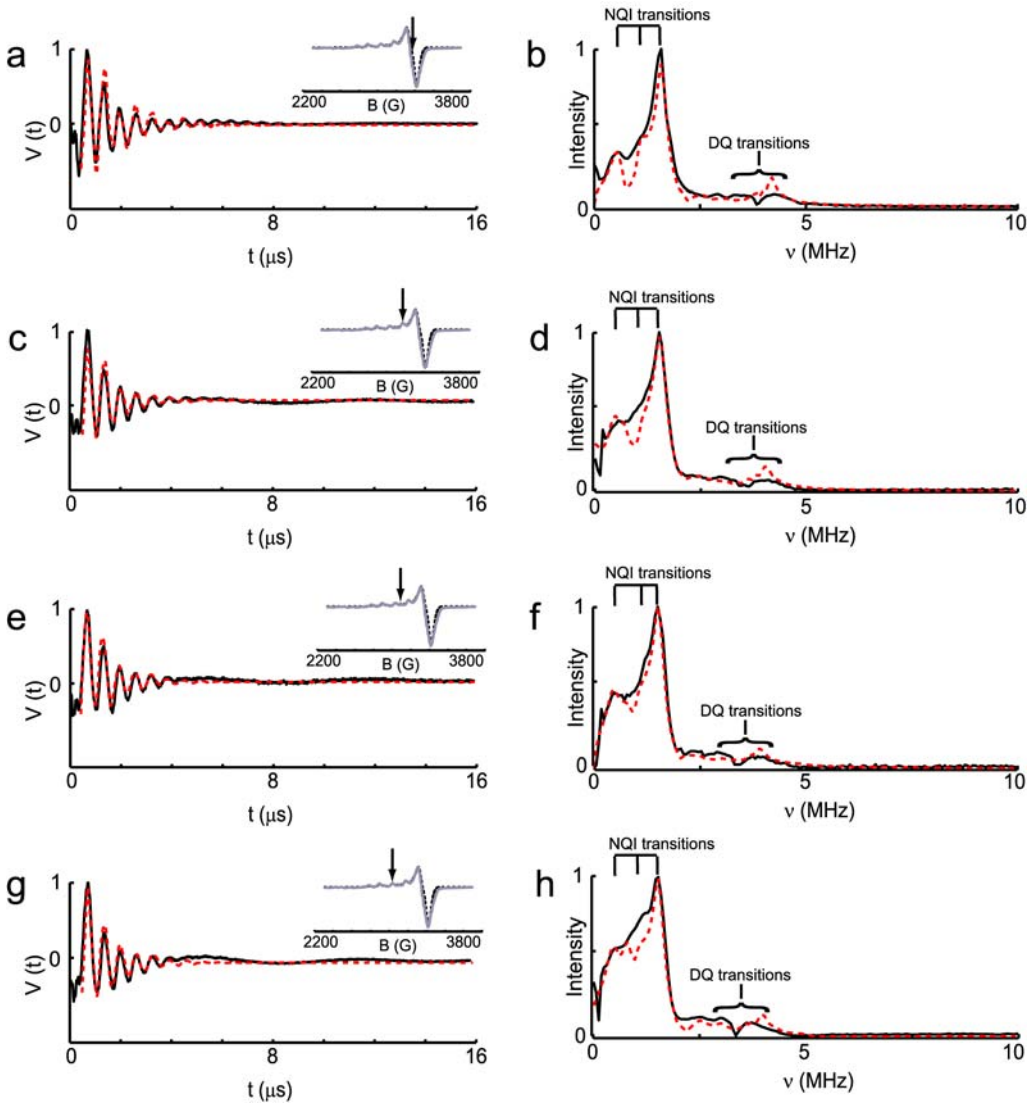

Figure 4-6. The experimental (black solid line) and simulated (red dotted line) three pulse ESEEM time domain data and spectra of the Cu^{2+}-EcoRI-DNA complex at external magnetic field 3369 G (a and b), 3189 G (c and d), 3116 G (e and f), and 3050 G (g and h).

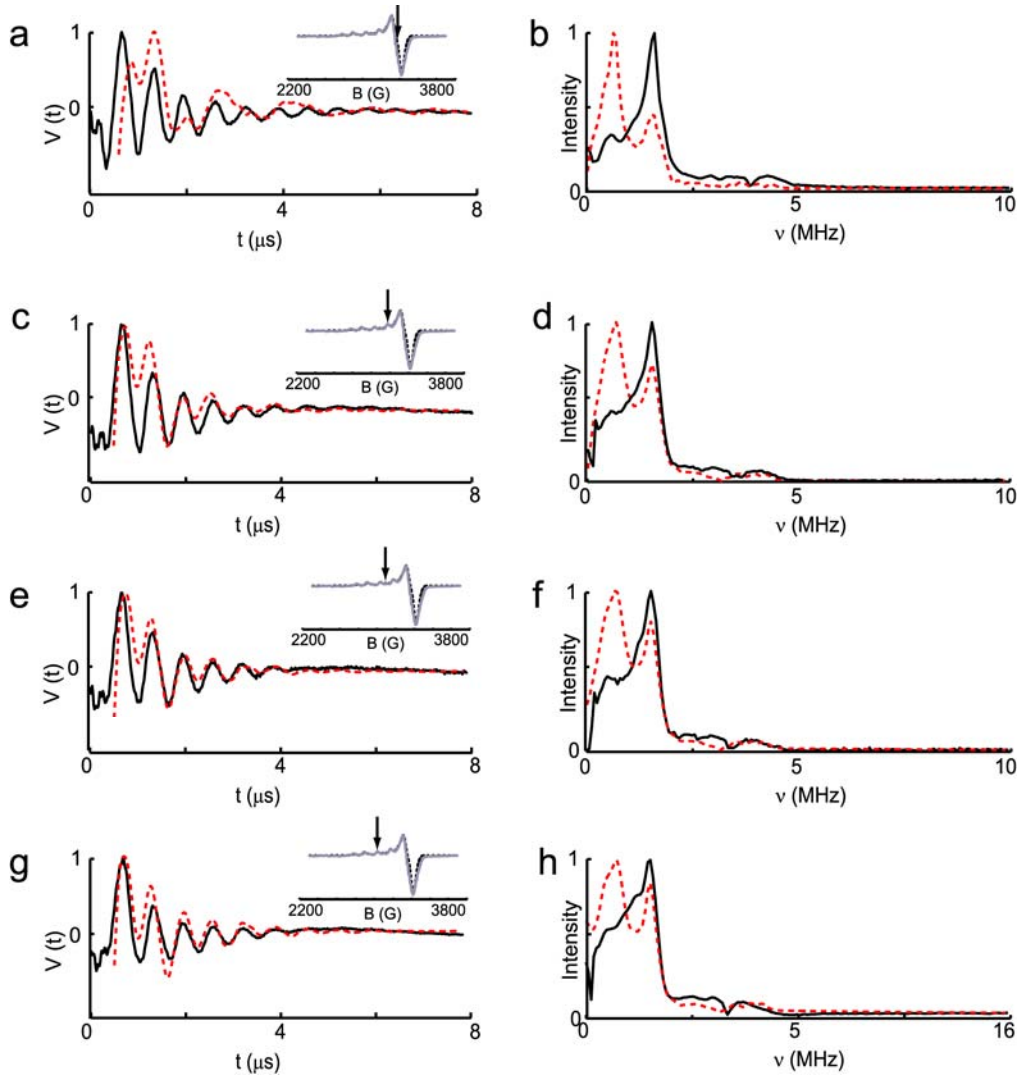

Figure 4-7. The experimental (black solid line) and simulated (red dotted line) three pulse ESEEM time domain data and spectra of the Cu^{2+}-EcoRI-DNA complex at external magnetic field 3369 G (a and b), 3189 G (c and d), 3116 G (e and f), and 3050 G (g and h). In the simulation only signal from cp1 is included.

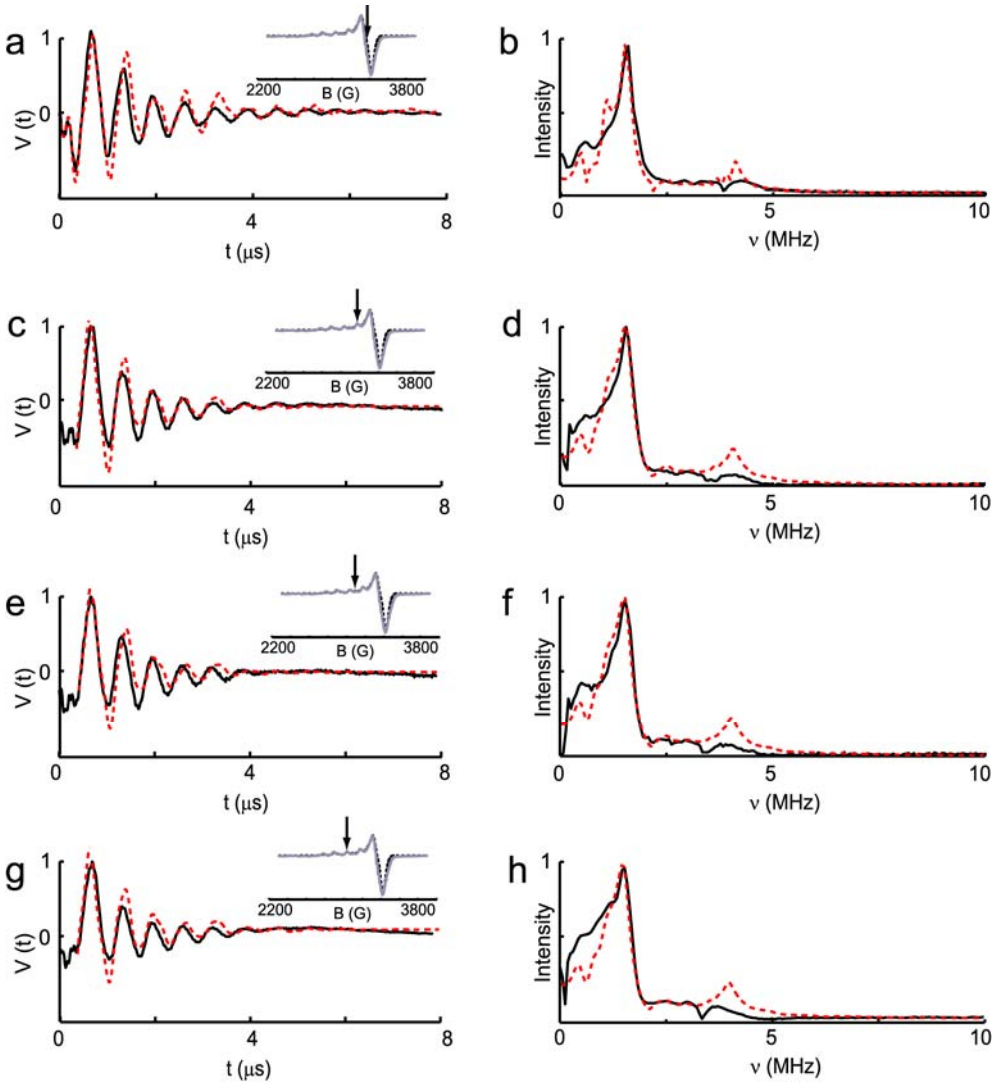

Figure 4-8. The experimental (black solid line) and simulated (red dotted line) three pulse ESEEM time domain data and spectra of the Cu^{2+}-EcoRI-DNA complex at external magnetic field 3369 G (a and b), 3189 G (c and d), 3116 G (e and f), and 3050 G (g and h). In the simulation only signal from cp2 is included.

Based on W-band ENDOR results, the solvent exchangeable protons that provide the H2 signal could originate from the axially coordinated water (Wa) molecule(s). Using the anisotropic hyperfine coupling constant T_{dip} (2.8 MHz) of H2 and point dipolar approximation,[34] the distance between Cu^{2+} and this proton is ~3.0 Å. Since in both components the interaction between Cu^{2+} and remote ^{14}N of H114 is strong (distances are ~2.4 Å and ~ 2.5 Å, respectively), the proton from remote ^{14}N (N_δ), which is also a solvent exchangeable proton, is close to the Cu^{2+} center (~3.3 Å) and can also provide hyperfine interactions that are close to the H2 signal. Therefore, we cannot unambiguously prove the existence of axially coordinated water molecule(s) in these two Cu^{2+} components.

Based on ESEEM results, the principal values of the hyperfine tensor in the two components are close and the distance between the remote ^{14}N of H114 and the Cu^{2+} center of cp2 is similar to cp1. However, the relative orientation between the PAS of the hyperfine *A* tensor and *g*-tensor in the two components are different. This orientational difference strongly affects the X-band ESEEM signals. Figure 4-9 shows that when we interchange the Euler angles, which describe the orientation between hyperfine tensor and *g*-tensor, in the two components, the simulated ESEEM spectra show a large deviation from the experimental data.

Taken together, the ESEEM results provide evidence that the Cu^{2+}-H114 coordination is similar in the two Cu^{2+} complexes, since the distance between the Cu^{2+} and the remote N atom of the H114 imidazole ring is similar. Remarkably, the remote ^{14}N of H114 shows a relatively strong interaction with the Cu^{2+} center.[156]

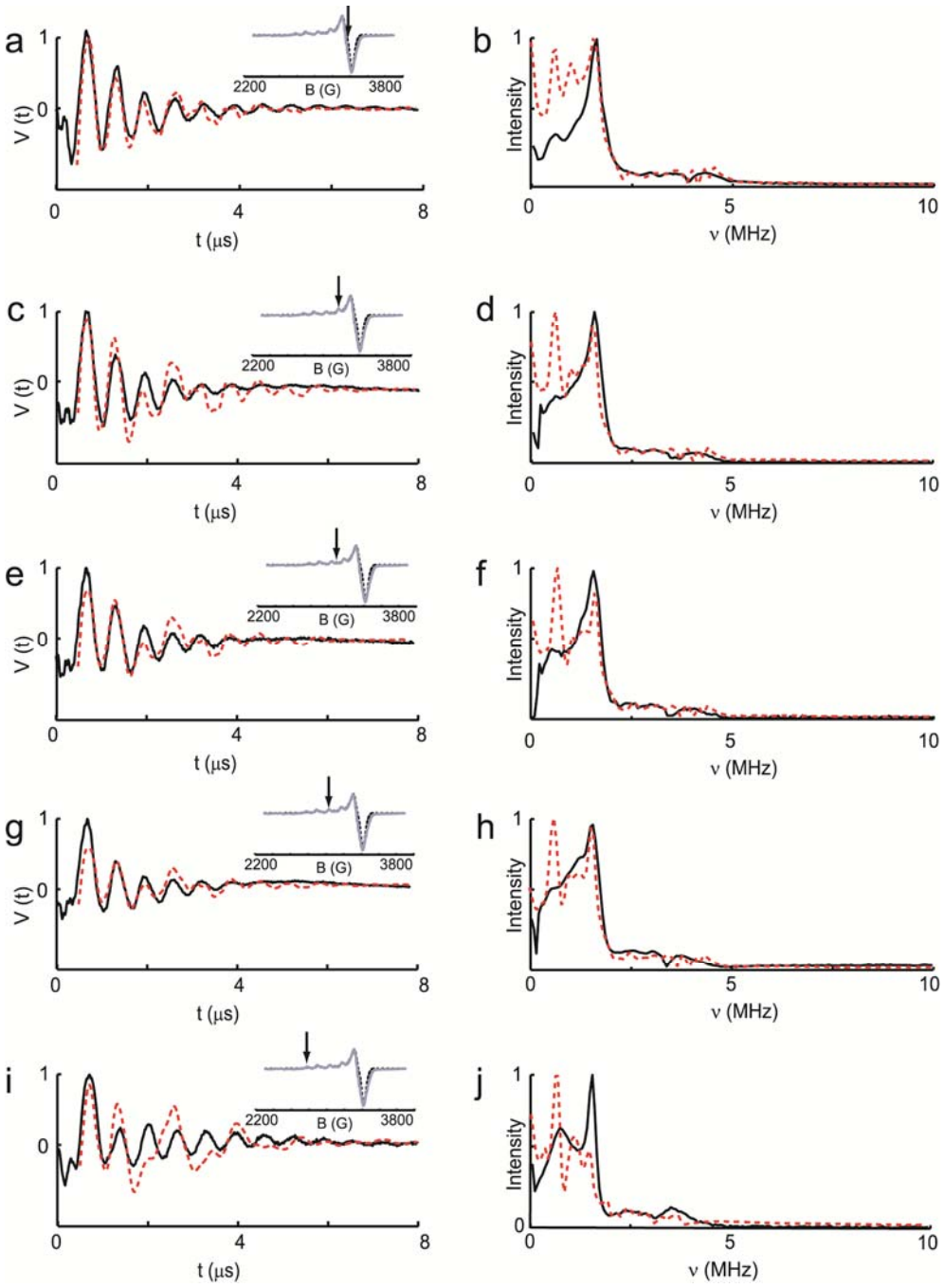

Figure 4-9. The experimental (black solid line) and simulated (red dotted line) three pulse ESEEM time domain data and spectra of the Cu^{2+}-EcoRI-DNA complex at external magnetic field 3369 G (a and b), 3189 G (c and d), 3116 G (e and f), 3050 G (g and h) and 2810 G (i and j). In the simulation we interchange the two sets of Euler angles, which describe the orientation between the hyperfine tensor and *g*-tensor in the two components.

4.4 CONCLUSION

The Cu^{2+}-binding site in the EcoRI-DNA has been examined by pulsed ESR experiments at W- and X-band. The W-band ENDOR spectra provide evidence for the existence of equatorially coordinated water molecules. Based on the X-band ESEEM spectra, the Cu^{2+}-H114 coordination is similar in the two components. Meanwhile, the solvent exchangeable signal of H2 from the W-band ENDOR experiments could originate either from the axially coordinated water molecules or the proton from remote ^{14}N of histidine imidazole.

4.5 ACKNOWLEDGEMENT

This research was supported by National Science Foundation grant MCB 1157712. The Bruker Elexsys E680 spectrometer was purchased with funds from National Institute of Health grant 1S10RR028701.

5.0 SENSITIVE COPPER-COPPER DISTANCE MEASUREMENTS IN A PROTEIN-DNA COMPLEX BY DOUBLE-QUANTUM COHERENCE ESR

This work, written in collaboration with Sharon Ruthstein, Preeti Mehta, Linda Jen-Jacobson, Sunil Saxena, has been published in J. Phys. Chem. B, 2013. Reprinted with permission from JOURNAL OF PHYSICAL CHEMISTRY B, 2013, 117, 6227-6230. Copyright (2013) American Chemical Society. Author contributions: S. S. designed research. S. R. performed DQC experiments; P. M. performed the sample preparation; S. R., M. J. and S. S. analyzed data; S. R., M. J., L. J.-J. and S. S. wrote the paper.

5.1 INTRODUCTION

Herein, we demonstrate a simple way to measure paramagnetic metal ion based nanoscale distances in proteins. The advent of Double Electron Electron Resonance (DEER)[40,44] and Double Quantum Coherence (DQC)[45,157] methods that measure nanometer range interspin distances have had a profound impact on the application of ESR in biological research.[13,158-164] Most of these distance measurements are based on the methanethiolsulfonate nitroxide spin-label, which is chemically attached to the cysteine residue in proteins.[53] The extension of DEER and DQC distance measurements to paramagnetic metal ions can potentially generalize the technique to many proteins that contain endogenous metal ion binding sites. However, DEER

and DQC with metal ions as spin probe are challenging because of large ESR spectral width and low signal to noise ratio (SNR). Nevertheless, our group[49,81] and others[76-79,86,89,91,92,96,165,166] have made tangible progress. In principle DQC can have a high SNR per shot. This provides impetus for further research of DQC. On the other hand, the DQC signal has substantial contributions from electron-nuclear interactions between the electron spin and neighboring ^{14}N as well as ^{1}H nuclear spins that are present in the amino-acid coordination environment. These nuclear modulation[25] effects swamp the modulation due to the electron-electron dipolar (EED) interactions and make it difficult to measure the interspin distance.

EcoRI is a 62 kDa homodimeric protein[110,167] that recognizes and binds to the 5'-GAATTC-3' DNA sequence with high specificity,[114,115,117] even in the absence of metal cofactors. In the presence of Mg^{2+}, EcoRI catalyzes cleavage of both DNA strands at this site. When Mg^{2+} is replaced by other metal ions the cleavage rates decrease according to the series $Mg^{2+} \approx Mn^{2+} > Co^{2+} >> Zn^{2+} >> Cd^{2+} > Ni^{2+}$.[117] Interestingly, Cu^{2+} is a powerful inhibitor of EcoRI catalysis.[7] In order to shed light on the molecular mechanism of catalytic inhibition by Cu^{2+}, we have recently exploited DEER based distance measurements to determine that Cu^{2+} binds to His114 in each subunit of EcoRI,[7] at points 13 Å from the Mg^{2+} positions in the catalytic sites. The positions of the His114 sidechains are consequently altered, and the resulting disruption of critical protein-DNA interactions and water molecules in the catalytic centers leads to inhibition of catalysis.[7]

In this work we present a simple way to minimize the low frequency nuclear peaks in the DQC spectrum and resolve the dipolar interaction between two paramagnetic probes Cu^{2+} with high sensitivity in the complex of restriction endonuclease EcoRI with its cognate DNA.

5.2 EXPERIMENTAL METHODS

Enzyme expression and purification: The EcoRI protein was expressed from a maltose-binding protein-EcoRI (MBP-EcoRI) fusion construct. Details for generation of the fusion gene and expression of the fusion protein are given in supporting information for reference.[7] The complete EcoRI protein without extra amino acids was isolated, purified, and characterized as described in reference.[148]

Cu^{2+}-EcoRI-DNA sample preparation: A solution of EcoRI (5 μM) in the presence of fivefold molar excess of TCGCGAATTCGCG was exchanged into 30 mM N-ethylmorpholine (NEM) buffer, which contains 0.3 M NH_4Cl, 10% dioxane, 30% deuterated glycerol (d8), 65% D_2O (pH 8.0) and concentrated. The final concentrations of EcoRI and DNA were 380 μM and 1.5 mM, respectively. Isotopically enriched $^{63}CuCl_2$ (Cambridge Isotope Labs, Inc) was added at a 4:1 molar ratio (Cu^{2+} : protein dimer). The sample was stored at -80°C and flash-frozen before each ESR experiment.

Electron Spin Resonance Spectroscopy: All of the pulsed ESR experiments were performed on a Bruker Elexsys 580 spectrometer at 20 K, with a MD5 resonator. The six-pulse DQC-ESR was using a $\pi/2\text{-}t_p\text{+dt-}\pi\text{–}t_p\text{+dt-}\pi/2\text{-}t_1\text{-}\pi\text{-}t_1\text{-}\pi/2\text{-}t_2\text{-}\pi$-echo sequence. A 64 step phase cycle was carried out to select the correct coherence pathway and the DQC-echo after the sixth pulse was integrated.[48,49] The $\pi/2$ pulse and π pulse lengths were 8 ns (or 12 ns, 16 ns and 20 ns) and 16 ns (or 24 ns, 32 ns and 40 ns), respectively. The interval t_p was incremented from 80 ns with a stepsize of 8 ns, for a total of 360 points. The interval t_1 was 80 ns and t_2 was 200 ns. The shot repetition time was 5 ms and all the DQC time domain data were averaged for 24 scans. Each

DQC experiment was done at 3350 G where the maximum echo signal was observed. Details of the DEER experiment are given in supporting information and reference.[7]

Simulation of DQC signal after division: To analyze the DQC data, simulations were carried out in MATLAB using the density matrix evolution theory. The Hamiltonian (equation 1) used includes the electron Zeeman interaction of each Cu^{2+} center, and the dipolar interaction between the two Cu^{2+} centers (D tensor).

$$\hat{\mathrm{H}}_0 = \hbar\Omega_1\hat{S}_{z1} + \hbar\Omega_2\hat{S}_{z2} + \vec{D}\hat{S}_{z1}\hat{S}_{z2} \tag{5-1}$$

The orientation of one of the dipolar frame to PAS1 was defined by (α1,β1,0) Euler angles. The orientation of one axial symmetric (PAS1) to another (PAS2) was defined by (0, β2,0) Euler angles. All frames were rotated back to the lab frame by (θ,φ).

$$\hat{H} = \beta\cdot(0 \quad 0 \quad B_0)\cdot R(\theta,\varphi)\cdot R_1\cdot\begin{pmatrix} g_{1xx} & 0 & 0 \\ 0 & g_{1yy} & 0 \\ 0 & 0 & g_{1zz}\end{pmatrix}\cdot R_1^{-1}\cdot R^{-1}(\theta,\varphi)\cdot\begin{pmatrix} S_{1x} \\ S_{1y} \\ S_{1z}\end{pmatrix} +$$

$$+\beta\cdot(0 \quad 0 \quad B_0)\cdot R(\theta,\varphi)\cdot R_1\cdot R_2\cdot\begin{pmatrix} g_{2xx} & 0 & 0 \\ 0 & g_{2yy} & 0 \\ 0 & 0 & g_{2zz}\end{pmatrix}\cdot R_2^{-1}\cdot R_1^{-1}\cdot R^{-1}(\theta,\varphi)\cdot\begin{pmatrix} S_{2x} \\ S_{2y} \\ S_{2z}\end{pmatrix} +$$

$$+\begin{pmatrix} S_{1x} & S_{1y} & S_{1z}\end{pmatrix}\cdot R(\theta,\varphi)\cdot\begin{pmatrix} D_{xx} & 0 & 0 \\ 0 & D_{yy} & 0 \\ 0 & 0 & D_{zz}\end{pmatrix}\cdot R^{-1}(\theta,\varphi)\cdot\begin{pmatrix} S_{2x} \\ S_{2y} \\ S_{2z}\end{pmatrix}$$

$$R_1 = R(\alpha 1 \quad \beta 1 \quad 0),\ R_2 = R(0 \quad \beta 2 \quad 0) \tag{5-2}$$

$$R(\alpha,\beta,\gamma)$$

$$= R_z R_y R_z = \begin{bmatrix} \cos\alpha & -\sin\alpha & 0 \\ \sin\alpha & \cos\alpha & 0 \\ 0 & 0 & 1 \end{bmatrix} \cdot \begin{bmatrix} \cos\beta & 0 & \sin\beta \\ 0 & 1 & 0 \\ -\sin\beta & 0 & \cos\beta \end{bmatrix} \cdot \begin{bmatrix} \cos\gamma & -\sin\gamma & 0 \\ \sin\gamma & \cos\gamma & 0 \\ 0 & 0 & 1 \end{bmatrix} \tag{5-3}$$

$$D = \begin{bmatrix} d_\perp & 0 & 0 \\ 0 & d_\perp & 0 \\ 0 & 0 & d_\parallel \end{bmatrix} \qquad d_\perp = -\frac{d_\parallel}{2} = \frac{\mu_0 g_a g_b \beta_e^2}{4\pi\hbar r^3} \tag{5-4}$$

The Hamiltonian can be written as:

$$\begin{aligned} \hat{H} = & (0 \quad 0 \quad B_0) \cdot \begin{pmatrix} a_{11} & a_{12} & a_{13} \\ a_{21} & a_{22} & a_{23} \\ a_{31} & a_{32} & a_{33} \end{pmatrix} \cdot \begin{pmatrix} S_{1x} \\ S_{1y} \\ S_{1z} \end{pmatrix} + \\ & + (0 \quad 0 \quad B_0) \cdot \begin{pmatrix} b_{11} & b_{12} & b_{13} \\ b_{21} & b_{22} & b_{23} \\ b_{31} & b_{32} & b_{33} \end{pmatrix} \cdot \begin{pmatrix} S_{2x} \\ S_{2y} \\ S_{2z} \end{pmatrix} + \\ & + \begin{pmatrix} S_{1x} & S_{1y} & S_{1z} \end{pmatrix} \cdot \begin{pmatrix} c_{11} & c_{12} & c_{13} \\ c_{21} & c_{22} & c_{23} \\ c_{31} & c_{32} & c_{33} \end{pmatrix} \cdot \begin{pmatrix} S_{2x} \\ S_{2y} \\ S_{2z} \end{pmatrix} \\ = & a_{33} B_0 S_{z1} + b_{33} B_0 S_{z2} + c_{33} S_{z1} S_{z2} + \left(\frac{c_{31} - i c_{32}}{2}\right) S_{z1} S_{+2} + \left(\frac{c_{31} + i c_{32}}{2}\right) S_{z1} S_{-2} \end{aligned} \tag{5-5}$$

Taking into account the high field approximation:

$$\hat{\mathrm{H}}_0 = \hbar\Omega_1 \hat{S}_{z1} + \hbar\Omega_2 \hat{S}_{z2} + \vec{D}\hat{S}_{z1}\hat{S}_{z2} = a_{33} B_0 S_{z1} + b_{33} B_0 S_{z2} + c_{33} S_{z1} S_{z2} \tag{5-6}$$

Then:

$$H_{0\alpha} = \begin{bmatrix} \frac{a_{33}\beta B_0}{2} + \frac{b_{33}\beta B_0}{2} + \frac{c_{33}}{4} & 0 \\ 0 & \frac{a_{33}\beta B_0}{2} - \frac{b_{33}\beta B_0}{2} - \frac{c_{33}}{4} \end{bmatrix}$$
$$H_{0\beta} = \begin{bmatrix} \frac{a_{33}\beta B_0}{2} - \frac{b_{33}\beta B_0}{2} - \frac{c_{33}}{4} & 0 \\ 0 & -\frac{a_{33}\beta B_0}{2} - \frac{b_{33}\beta B_0}{2} + \frac{c_{33}}{4} \end{bmatrix} \quad (5\text{-}7)$$

The four energy values are:

$$E_1 = \frac{a_{33}\beta B_0}{2} + \frac{b_{33}\beta B_0}{2} + \frac{c_{33}}{4}$$
$$E_2 = \frac{a_{33}\beta B_0}{2} - \frac{b_{33}\beta B_0}{2} - \frac{c_{33}}{4}$$
$$E_3 = \frac{a_{33}\beta B_0}{2} - \frac{b_{33}\beta B_0}{2} - \frac{c_{33}}{4} \quad (5\text{-}8)$$
$$E_4 = -\frac{a_{33}\beta B_0}{2} - \frac{b_{33}\beta B_0}{2} + \frac{c_{33}}{4}$$

The time evolution of the spin density, Σ, is described by:

$$\frac{d\sum(t)}{dt} = i[\hat{H}, \sum_0] \quad (5\text{-}9)$$

where Σ_0 is the spin density at t=0.

$$\sum_0 = \begin{vmatrix} \sum_0^{\alpha} & \\ & \sum_0^{\beta} \end{vmatrix} = \begin{bmatrix} 1 & 0 & 0 & 0 \\ 0 & 1 & 0 & 0 \\ 0 & 0 & -1 & 0 \\ 0 & 0 & 0 & -1 \end{bmatrix} \quad (5\text{-}10)$$

The signal, V(t) is given by:

$$V(t) = Tr[\sum(t) S_{\pm}] \quad (5\text{-}11)$$

$$S_{\pm} = \begin{bmatrix} 0 & 1 & 1 & 0 \\ 1 & 0 & 0 & 1 \\ 1 & 0 & 0 & 1 \\ 0 & 1 & 1 & 0 \end{bmatrix}$$

$$\sum(t) = \exp(-i\hat{H}t) \sum_0 \exp(i\hat{H}t) \quad (5\text{-}12)$$

The spin density during the 6-pulses DQC experiment is calculated using the following equation:

$$\sum(t) = R\sum_0 R^{-1}$$
$$R = R_{t_2}R_{6p}R_{t_2}R_{5p}R_{t_1}R_{4p}R_{t_1}R_{3p}R_{t_p+\Delta t}R_{2p}R_{t_p+\Delta t}R_{1p}$$
$$R^{-1} = (R_{t_2}R_{6p}R_{t_2}R_{5p}R_{t_1}R_{4p}R_{t_1}R_{3p}R_{t_p+\Delta t}R_{2p}R_{t_p+\Delta t}R_{1p})^{-1} \quad (5\text{-}13)$$

Where R_t represents the evolution of the spin density during the evolution time t between two pulses. And R_p is the evolution of the spin density during the pulse.

During the evoluation time :

$$\hat{\mathrm{H}} = \hat{\mathrm{H}}_0$$

$$R_t = \begin{bmatrix} \exp(-iE_1t) & 0 & 0 & 0 \\ 0 & \exp(-iE_2t) & 0 & 0 \\ 0 & 0 & \exp(-iE_3t) & 0 \\ 0 & 0 & 0 & \exp(-iE_4t) \end{bmatrix} \quad (5\text{-}14)$$

During the pulse, H is given by:

$$\hat{\mathrm{H}} = \hat{\mathrm{H}}_0 + \hat{\mathrm{H}}_1$$
$$\hat{\mathrm{H}}_1 = \omega_1 S_x$$

$$H_\alpha = \begin{bmatrix} \frac{a_{33}\beta B_0}{2} + \frac{b_{33}\beta B_0}{2} + \frac{c_{33}}{4} & \frac{\omega_1}{2} \\ \frac{\omega_1}{2} & \frac{a_{33}\beta B_0}{2} - \frac{b_{33}\beta B_0}{2} - \frac{c_{33}}{4} \end{bmatrix}$$
$$H_\beta = \begin{bmatrix} \frac{a_{33}\beta B_0}{2} - \frac{b_{33}\beta B_0}{2} - \frac{c_{33}}{4} & -\frac{\omega_1}{2} \\ -\frac{\omega_1}{2} & -\frac{a_{33}\beta B_0}{2} - \frac{b_{33}\beta B_0}{2} + \frac{c_{33}}{4} \end{bmatrix} \quad (5\text{-}15)$$

$H_{\alpha,\beta}$ are not diagonalized. The diagonalized matrice is defined as M. E_a, E_b, E_c, and E_d are the eigenvalues of $H_{\alpha,\beta}$.

$$R_p = \begin{bmatrix} \exp(-iE_a t) & 0 & 0 & 0 \\ 0 & \exp(-iE_b t) & 0 & 0 \\ 0 & 0 & \exp(-iE_c t) & 0 \\ 0 & 0 & 0 & \exp(-iE_d t) \end{bmatrix} \tag{5-16}$$

Since there is a need to transform the pulse frame into the frame of H_0, equation 13 is rewritten as:

$$\begin{aligned} &\Sigma(t) = R \Sigma_0 R^{-1} \\ &R = R_{t_2} M^{-1} R_{6p} R_{t_2} M^{-1} R_{5p} R_{t_1} M^{-1} R_{4p} R_{t_1} M^{-1} R_{3p} R_{t_p+\Delta t} M^{-1} R_{2p} R_{t_p+\Delta t} M^{-1} R_{1p} \end{aligned} \tag{5-17}$$

The simulation finds the best-fit for r, Δr, the Euler angles (α1,β1,β2) and the distribution of angles. The signal is integrated over θ and φ. The phase cycle for this experiment was taking into account as well in the calculations. The best fit was obtained with a mean Cu^{2+}-Cu^{2+} distance of 3.5 nm and a standard deviation of 0.1 nm, (α1,β1,β2)=(90°,0°,30°).

5.3 RESULTS AND DISCUSSION

Figure 5-1 shows the Cu^{2+}-DQC data obtained at the $g_\perp$ position of the Cu^{2+} ESR absorption spectrum. The lengths of the π pulse were 16 ns (black solid line) and 40 ns (grey solid line), respectively (all the DQC data collected by Dr. S. Ruthstein).

The two spectra in Figure 5-1b with different length of π pulse clearly contain peaks that can be attributed to the ^{14}N-nuclear modulations in the 0-5 MHz region[49] as well as the ^{1}H-nuclear peaks at ~14 MHz. For the purpose of nanoscale distance measurements the 0-5 MHz ^{14}N-nuclear peaks are particularly problematic, since the EED interaction is in this region.

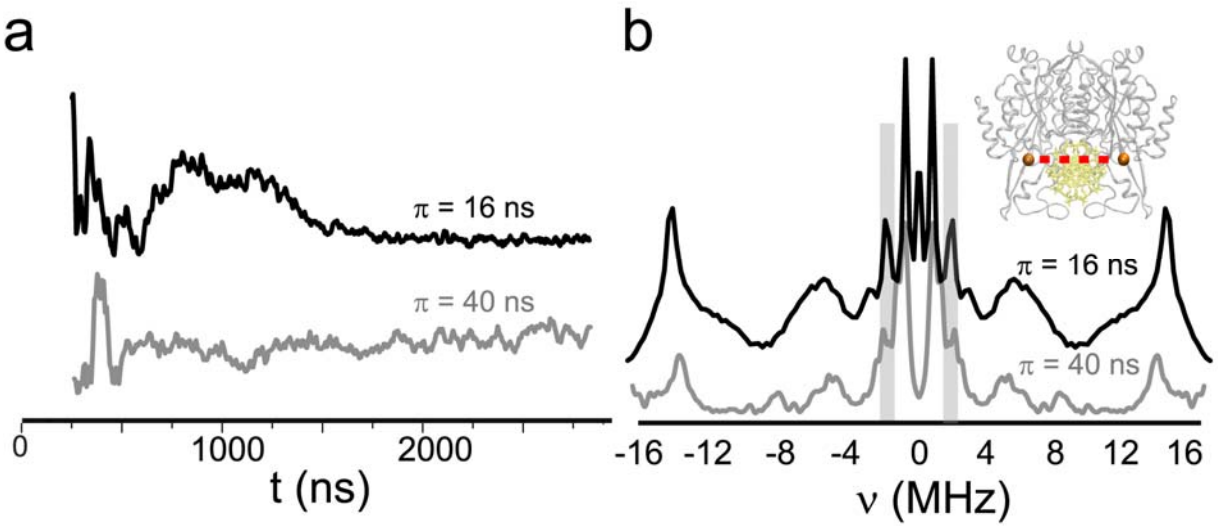

Figure 5-1. The experimental Cu^{2+}-DQC (a) time domain signals and (b) spectra of the EcoRI-DNA complex, measured at two different π pulse lengths: π=16 ns (black solid line) and π=40 ns (grey solid line). The signal to noise ratios for the two traces with π=16 ns and π=40 ns are ~133 and ~120, respectively. The inset present the X-ray structure of the EcoRI-DNA complex: the grey color structure represents EcoRI, and the yellow color structure represents DNA; the orange balls represent Cu^{2+} ions. The protein and DNA structures are from a highly refined version[110,167] of the protein data bank entry 1CKQ. The DNA sequence is TCGCGAATTCGCG.

Interestingly, the intensity of the peak at ~1.46 MHz in the DQC spectrum (Figure 5-1b) with 40 ns π pulse is much lower compared to the spectrum with 16 ns π pulse. With shorter π pulse, e. g., 16 ns, the spectral excitation probability of the DQC EED interaction is about 0.16.[48] With the longer π pulse of 40 ns, the spectral excitation probability of the DQC EED interaction is about 0.04.[48] It is very clear that longer π pulse cannot substantially populate the double quantum coherence of EED interaction. However, the nuclear hyperfine and quadrupole transitions are weakly sensitive to the length of π pulse.[25] This suggests that 1.46 MHz peak might originate from the Cu^{2+}-EED interaction.

Since the experimental DQC signal is a multiplication of the EED and the nuclear signals, division of the π=16 ns DQC data by the π=40 ns DQC data may suppress the nuclear signals and resolve the EED signal.[48,49] Figure 5-2a shows the comparison of the DQC time domain data, after dividing the π=16 ns signal by the π=40 ns signal (black solid line), with the DEER data after subtraction of the homogeneous background (grey solid line).[7] The modulation periods of the two time domain traces are comparable. In this analysis, the DQC signal with 40 ns π pulse was empirically chosen for division – the data with other choices are shown in the Appendix A. The data acquisition time of DQC (including two traces) and DEER are ~50 hrs and ~43 hrs, respectively. The data collection time in DQC can be reduced by implementation of on-board phase cycling.

The DQC spectrum after division, shown in Figure 5-2b (black solid line), clearly resolves the major peak at ~1.46 MHz, which is consistent with the DEER data (Figure 5-2b, grey solid line). Nevertheless, the DQC spectrum is narrower than the DEER spectrum. In the experimental DQC data, there might be some small residual peaks from electron-^{14}N interactions that occur at ~3 MHz.

Figure 5-2 also shows the simulated DQC data (black dotted line). Based on the best fitting of the DQC time domain data shown in Figure 5-2, we obtained a most probable Cu^{2+}-Cu^{2+} distance of ~35 Å with a standard deviation of 1 Å (Figure 5-2b, black solid line inset). This result is consistent with our observation from DEER experiments (Figure 5-2b, red dotted line inset). The simulated DQC spectrum is in accord with the dominant peak obtained in the experiment, although the DQC data is narrower.[7] It is likely that in DQC a narrower range of orientations is selected because the microwave pulses have a finite coverage. Despite this, the signal to noise ratio per shot in DQC is high (cf. figure caption in Figure 5-2 and Appendix A).

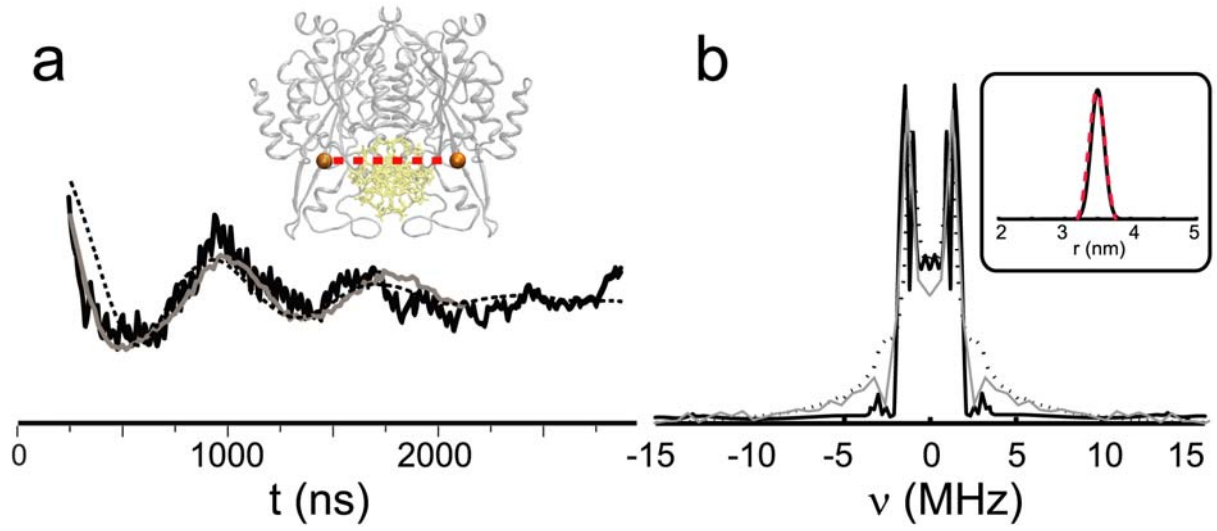

Figure 5-2. The comparison of the Cu^{2+}-DEER data (grey solid line) with the experimental (black solid line) Cu^{2+}-DQC data. The simulated DQC trace is shown as a black dotted line. (a) The time traces are shown. The DQC time domain data is obtained by division of a π=16 ns signal by a π=40 ns signal. The high frequency component in the DQC data is from proton hyperfine interaction and is not noise. The signal to noise ratio for DEER and DQC were 66 and 61, respectively – details are provided in the Appendix B. The number of averages for DEER and DQC were 5760 and 1536, respectively. (b) The DEER and DQC spectra are shown and the distance distribution functions are provided in the inset. The distance distribution functions from DEER (red dotted line) and DQC (black solid line) were obtained from fitting of the experimental time domain data.

5.4 CONCLUSIONS

We have clearly shown here that metal ion based nanometer range distance can be measured by DQC. DEER has a significant advantage due to the ease of implementation on commercial instrument. Nevertheless, the DQC data have high SNR per shot. Further improvements can be made by the use of narrower pulse lengths[48] and by understanding the role of orientational effects in such DQC measurements.[81,168]

5.5 ACKNOWLEDGMENT

This work was supported by a National Science Foundation (MCB 1157712) grant. Protein expression was supported by NIH MERIT (5R37-GM02907) grant to L.J.-J.

6.0 SUMMARY

The type II restriction endonuclease EcoRI is of great interest as a model system because it exhibits an extremely high specificity in DNA binding and catalysis. In this thesis, the paramagnetic metal ion Cu^{2+} is used as a spin probe to understand the cleavage of DNA by EcoRI.

First, we found a hitherto unknown metal ion binding site in this protein-DNA complex. X-band ESR results established that Cu^{2+} ions coordinate to H114 in EcoRI rather than the active site. This result was confirmed by measuring the binding affinity of Cu^{2+} in wild type and H114Y mutant EcoRI. The different binding site of Cu^{2+} versus the natural cofactor Mg^{2+} explains why Cu^{2+} does not catalyze DNA cleavage by EcoRI. MD simulations show that the Cu^{2+}-H114 coordination causes the movement of the H114 side chain. We proposed that this structural change disrupts a critical protein-DNA interaction that is essential for catalysis and leads to inhibition of Mg^{2+}-dependent cleavage.

We also proposed an electrostatic basis for the positive cooperativity of Mg^{2+} association with the EcoRI–DNA complex. The two Mg^{2+} binding sites are approximately 20 Å apart in the EcoRI-DNA complex. The positive cooperativity between these two sites is not obvious based on purely structural considerations. We applied MD simulations as well as electrostatic potential calculations to show that binding of Mg^{2+} at one catalytic site makes the surface electrostatic potential in the distal catalytic site more negative, which enhances the binding of the second

Mg^{2+}. This positive cooperativity helps double-strand cuts of foreign DNA by EcoRI. These observations provide insight into the structural and electrostatic factors that affect site-specificity catalysis by this class of endonucleases.

Second, we refined the Cu^{2+}-coordination in the EcoRI-DNA complex by using W-band ENDOR and X-band ESEEM experiments. The W-band ENDOR spectra provide direct evidence for the existence of equatorially coordinated water molecules. Based on the X-band ESEEM experiments at different magnetic fields, we identified a similar interaction between the Cu^{2+} center and H114 in the two components.

Lastly, we developed a simple method to measure the Cu^{2+}-Cu^{2+} distance in the EcoRI-DNA complex by Double Quantum Coherence (DQC) spectroscopy. The method can easily reduce the contribution of unwanted nuclear hyperfine and quadrupole interactions and resolve the desired electron-electron dipolar interactions. The results provide impetus for further development and application of paramagnetic metal ion-based DQC distance measurements.

APPENDIX A

The choice of the π-pulse length in DQC experiment: Figure A1 presents the DQC data for the Cu^{2+}-EcoRI-DNA complex with various π pulse lengths and the corresponding spectra. The intensity of the peak at 1.46 MHz is decreasing with the increase of pulse length. However, the nuclear effects with different π pulse are still intense. Thus, in principle, division between two DQC signals with different π pulse lengths can result in decreasing the contribution of the nuclear interaction modulations and showing only the electron electron dipolar interaction components. This is presented in Figure A2 for the Cu^{2+}-EcoRI-DNA complex. When the difference of the π pulse length in the two data for division is larger, the 0-5 MHz ^{14}N nuclear frequncy peaks are better suppressed after division and the dipolar peaks are more emphasized, as expected. However, the nuclear modulations from protons do increase, since the longer pulse-length cannot effectively excite these transitions and therefore they are not cancelled upon division.

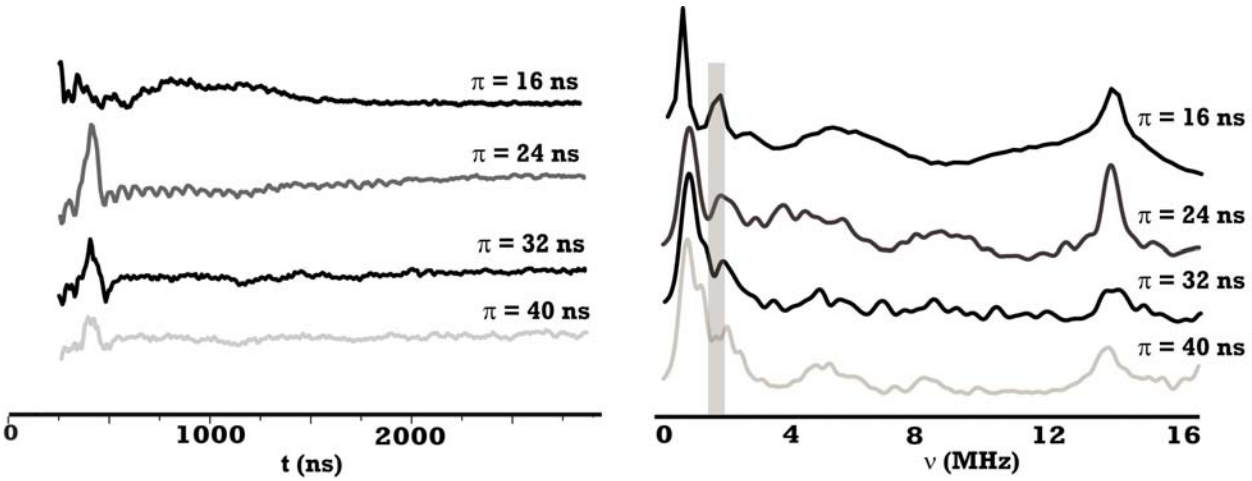

Figure A-1. DQC signals of the Cu^{2+}-EcoRI-DNA complex at various π pulse length and the corresponding spectra.

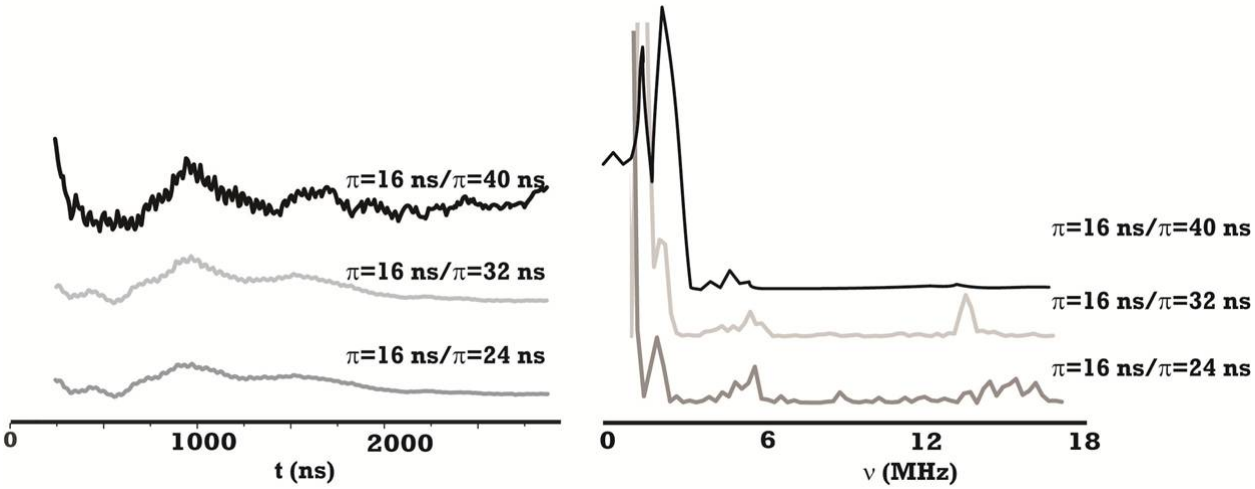

Figure A-2. DQC signals of the Cu^{2+}-EcoRI-DNA complex after dividing the signal of π=16 ns by other signals with different π pulse lengths and the corresponding spectra.

Signal to noise ratio (SNR) calculation of DQC and DEER signals: The SNR was calculated by the ratio between the amplitude of the 1.46 MHz peak and the r.m.s.d. fluctuation in baseline regions in the spectra.

For DQC spectrum after division (without the 20 MHz filtering), the intensity of the peak at ~1.46 MHz is 0.2074, and the r.m.s.d. ($\sqrt{\sum_{i=1}^{n}(x-\bar{x})^2/n}$) fluctuation in the baseline region (from ~30 MHz to ~62 MHz) is 0.0034 (Figure S2A). The SNR of DQC signal equals to 0.2074/0.0034 = 61. The number of scans is 24, and the number of phase cycle steps is 64. The total number of averages is 24 × 64 = 1536.

For DEER spectrum, the intensity of the peak at ~1.46 MHz is 0.1674, and the r.m.s.d. fluctuation in the baseline region (from ~5 MHz to ~30 MHz) is 0.0025 (Figure S2B). The SNR of DEER signal equals to 0.1674/0.0025 = 66. The number of scans is 720. Each scan was averaged by adding traces at four different τ_1 values (SI, part E). And the number of phase cycle steps is 2. The total number of averages is 720 × 4 × 2 = 5760. Taking into account the square root of number of averages (SNR ∝ square root of number of averages), SNR(per shot, DQC)/SNR(per shot, DEER) = [61 × $(5760)^{1/2}$]/ [61 × $(1536)^{1/2}$] = 1.8.

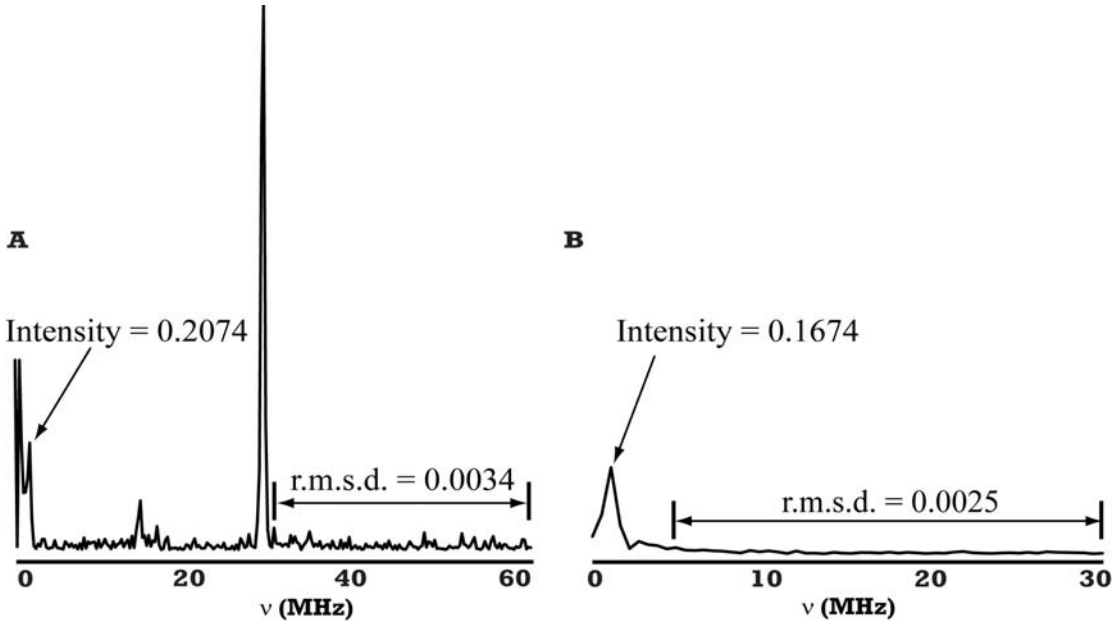

Figure A-3. (a) Spectrum of DQC signal without 20 MHz filtering. (b) Spectrum of DEER signal.

BIBLIOGRAPHY

(1) Zavoisky, Y. *J. Phys. USSR* **1945**, *9*, 211.

(2) Shin, B.-k.; Saxena, S. Insight into Potential Cu(II)-Binding Motifs in the Four Pseudorepeats of Tau Protein. *J. Phys. Chem. B* **2011**, *115*, 15067-15078.

(3) Steinhoff, H.-J. Inter- and intra-molecular distances determined by EPR spectroscopy and site-directed spin labeling reveal protein-protein and protein-oligonucleotide interaction. *Biol. Chem.* **2005**, *385*, 913-920.

(4) Schiemanna, O.; Prisner, T. F. Long-range distance determinations in biomacromolecules by EPR spectroscopy. *Q. Rev. Biophys.* **2007**, *40*, 1-53.

(5) Tsvetkov, Y. D.; Milov, A. D.; Maryasov, A. G. Pulsed Electron-Electron Double Resonance (PELDOR) as EPR Spectroscopy in Nanometer range *Russ. Chem. Rev.* **2008**, *77*, 487-520.

(6) Jeschke, G. DEER Distance Measurements on Proteins. *Annu. Rev. Phys. Chem.* **2012**, *63*, 419-446.

(7) Yang, Z.; Kurpiewski, M. R.; Ji, M.; Townsend, J. E.; Mehta, P.; Jen-Jacobson, L.; Saxena, S. ESR spectroscopy identifies inhibitory Cu^{2+} sites in a DNA-modifying enzyme to reveal determinants of catalytic specificity. *Proc. Natl. Acad. Sci. USA* **2012**, *109*, E993-E1000.

(8) Shin, B.-k.; Saxena, S. Direct Evidence That All Three Histidine Residues Coordinate to Cu(II) in Amyloid-β_{1-16}. *Biochemistry* **2008**, *47*, 9117-9123.

(9) Shin, B.-k.; Saxena, S. Substantial Contribution of the Two Imidazole Rings of the His13−His14 Dyad to Cu(II) Binding in Amyloid-β(1−16) at Physiological pH and Its Significance. *J. Phys. Chem. A* **2011**, *115*, 9590-9602.

(10) Silva, K. I.; Saxena, S. Zn(II) Ions Substantially Perturb Cu(II) Ion Coordination in Amyloid-β at Physiological pH. *J. Phys. Chem. B* **2013**, *117*, 9386-9394.

(11) Ruthstein, S.; Stone, K. M.; Cunningham, T. F.; Ji, M.; Cascio, M.; Saxena, S. Pulsed ESR Resolves the Coordination Site of Cu(II) Ions in α1-Glycine Receptor. *Biophys. J.* **2010**, *99*, 2497-2506.

(12) Jun, S.; Gillespie, J. R.; Saxena, B.-k. S. a. S. The Second Cu(II)-Binding Site in a Proton-Rich Environment Interferes with the Aggregation of Amyloid-β(1−40) into Amyloid Fibrils. *Biochemistry* **2009**, *48*, 10724-10732.

(13) Stone, K.; Townsend, J. E.; Sarver, J.; Sapienza, P. J.; Saxena, S.; Jen-Jacobson, L. Electron spin resonance shows common structural features for different classes of EcoRI-DNA complexes. *Angew. Chem. Int. Ed. Engl.* **2008**, *47*, 10192-10194.

(14) Jun, S.; Saxena, S. The Aggregated State of Amyloid-β Peptide In Vitro Depends on Cu^{2+} Ion Concentration. *Angew. Chem. Int. Ed. Engl.* **2007**, *46*, 3959-3961.

(15) Meng, R.; Becker, J.; Lin, F.-T.; Saxena, S.; Weber, S. G. Binding of Copper(II) to Thyrotropin-Releasing Hormone (TRH) and Its Analogs. *Inorg. Chim. Acta* **2005**, *358*, 2933-2942.

(16) Hubbell, W. L.; Lopez, C. J.; Altenbach, C.; Yang, Z. Technological Advances in Site-Directed Spin Labeling of Proteins. *Curr. Opin. Struct. Biol.* **2013**, *23*, 1-9.

(17) Savelieff, M. G.; Wilson, T. D.; Elias, Y.; Nilges, M. J.; Garner, D. K.; Lu, Y. Experimental Evidence for a Link among Cupredoxins: Red, Blue, and Purple Copper Transformations in Nitrous Oxide Reductase. *Proc. Natl. Acad. Sci. USA* **2008**, *105*, 7919-7924.

(18) Slichter, C. P. *Principles of Magnetic Resonance*; 3 ed.; Springer-Verlag: New York, 1989.

(19) Weil, J. A.; Bolton, J. R.; Weitz, J. E. *Electron Paramagnetic Resonance*; John Wiley & Sons, Inc.: New York, 1993.

(20) Peisch, J.; Blumberg, W. E. Structural Implications Derived from the Analysis of Electron Paramagnetic Resonance Spectra of Natural and Artificial Copper Proteins. *Arch. Biochem.Biophys.* **1974**, *165*, 691-708.

(21) Weil, J. A.; Bolton, J. R.; Weitz, J. E. *Electron Paramagnetic Resonance*; John Wiley & Sons, Inc.: New York, 1994.

(22) Mims, W. B. Envelope Modulation in Spin-Echo Experiments. *Phys. Rev. B* **1972**, *5*, 2409-2419.

(23) Mims, W. B.; Peisach, J. The Nuclear Modulation Effect in Electron Spin Echoes for Complexes of Cu^{2+} and Imidazole with ^{14}N and ^{15}N. *J. Chem. Phys.* **1978**, *69*, 4921-4930.

(24) Mims, W. B.; Davis, J. L. Proton Modulation of the Electron Spin Echo Envelope in a Nd^{3+}: Aquo Glass. *J. Chem. Phys.* **1976**, *64*, 4836-4846.

(25) Schweiger, A.; Jeschke, G. *Principles of pulse electron paramagnetic resonance*; Oxford University Press: New York, 2001.

(26) Lee, H.-I.; Doan, P. E.; Hoffman, B. M. General Analysis of ^{14}N (I=1) Electron Spin Echo Envelope Modulation. *J. Magn. Reson.* **1999**, *140*, 91-107.

(27) Flanagan, H. L.; Singel, D. J. Analysis of ^{14}N ESEEM Patterns of Randomly Oriented Solids. *J. Chem. Phys.* **1987**, *87*, 5606-5616.

(28) Burns, C. S.; Aronoff-Spencer, E.; Dunham, C. M.; Lario, P.; Avdievich, N. I.; Antholine, W. E.; Olmstead, M. M.; Vrielink, A.; Gerfen, G. J.; Peisach, J.; Scott, W. G.; Millhauser, G. L. Molecular Features of the Copper Binding Sites in the Octarepeat Domain of the Prion Protein. *Biochemistry* **2002**, *41*, 3991-4001.

(29) Kosman, D. J.; Peisach, J.; Mims, W. B. Pulsed Electron Paramagnetic Resonance Studies of the Copper(II) Site in Galactose Oxidase. *Biochemistry* **1980**, *19*, 1304-1308.

(30) McCracken, J.; Pember, S.; Benkovic, S. J.; Villafranca, J. J.; Miller, R. J.; Peisach, J. Electron Spin-Echo Studies of the Copper Binding Site in Phenylalanine Hydroxylase from Chromobacterium Violaceum. *J. Am. Chem. Soc.* **1988**, *110*, 1069-1074.

(31) McCracken, J.; Desai, P. R.; Papadopoulos, N. J.; Villafranca, J. J.; Peisach, J. Electron Spin-Echo Studies of the Copper(II) Binding Sites in Dopamine β-Hydroxylase. *Biochemistry* **1988**, *27*, 4133-4137.

(32) Jiang, F.; McCracken, J.; Peisach, J. Nuclear Quadrupole Interactions in Copper(II)-Diethylenetriamine-Substituted Imidazole Complexes and in Copper(II) Proteins. *J. Am. Chem. Soc.* **1990**, *112*, 9035-9044.

(33) McCracken, J.; Peisach, J.; Cote, C. E.; McGuirl, M. A.; Dooley, D. M. Pulsed EPR Studies of the Semiquinone State of Copper-Containing Amine Oxidases. *J. Am. Chem. Soc.* **1992**, *114*, 3715-3720.

(34) McCracken, J.; Peisach, J.; Dooley, D. M. Cu(II) Coordination Chemistry of Amine Oxidases. Pulsed EPR Studies of Histidine Imidazole, Water, and Exogenous Ligand Coordination. *J. Am. Chem. Soc.* **1987**, *109*, 4064-4072.

(35) Huffman, D. L.; Huyett, J.; Outten, F. W.; Doan, P. E.; Finney, L. A.; Hoffman, B. M.; O'Halloran, T. V. Spectroscopy of Cu(II)-PcoC and the Multicopper Oxidase Function of PcoA, Two Essential Components of Escherichia Coli Pco Copper Resistance Operon. *Biochemistry* **2002**, *41*, 10046-10055.

(36) Liboiron, B. D. In *High Resolution EPR: Applications to Metalloenzymes and Metals in Medicine*; Hanson, G., Berliner, L., Eds.; Springer: New York, 2009; Vol. 28; pp 507-549.

(37) Höfer, P.; Grupp, A.; Nebenführ, H.; Mehring, M. Hyperfine Sublevel Correlation (HYSCORE) Spectroscopy: A 2D ESR Investigation of the Squaric Acid Radical. *Chem. Phys. Lett.* **1986**, *132*, 279-282.

(38) Kulik, L.; Lubitz, W. Electron-Nuclear Double Resonance. *Photosynth. Res.* **2009**, *102*, 390-401.

(39) Gromov, I.; Krymov, V.; Manikandan, P.; D.Arieli; Goldfarb, D. A W-band Pulsed ENDOR Spectrometer Set-up and Applications to Transition Metals Centers. *J. Magn. Reson.* **1999**, *139*, 8-17.

(40) Milov, A. D.; Ponomarev, A. B.; Tsvetkov, Y. D. Electron-electron double resonance in electron spin echo: Model biradical systems and the sensitized photolysis of decalin. *Chem. Phys. Lett.* **1984**, *110*, 67-72.

(41) Larsen, R. G.; Singel, D. J. Double electron–electron resonance spin–echo modulation: Spectroscopic measurement of electron spin pair separations in orientationally disordered solids. *J. Chem. Phys.* **1993**, *98*, 5134-5146.

(42) Milov, A. D.; Maryasov, A. G.; Tsvetkov, Y. D. Pulsed Electron Double Resonance (PELDOR) and Its applications in Free-Radical Research. *Appl. Magn. Reson.* **1998**, *15*, 107-143.

(43) Martin, R. E.; Pannier, M.; Diederich, F.; Gramlich, V.; Hubrich, M.; Spiess, H. W. Determination of End-to-End Distances in a Series of TEMPO Diradicals of up to 2.8 nm Length with a New Four-Pulse Double Electron Electron Resonance Experiment. *Angew. Chem. Int. Ed. Engl.* **1998**, *37*, 2833-2837.

(44) Pannier, M.; Veit, S.; Godt, A.; Jeschke, G.; Spiess, H. W. Dead-Time Free Measurement of Dipole–Dipole Interactions between Electron Spins. *J. Magn. Reson.* **2000**, *142*, 331-340.

(45) Borbat, P. P.; Freed, J. H. Multiple-Quantum ESR and Distance Measurements. *Chem. Phys. Lett.* **1999**, *313*, 145-154.

(46) Saxena, S.; Freed, J. H. Theory of double quantum two-dimensional electron spin resonance with application to distance measurements. *J. Chem. Phys.* **1997**, *107*, 1317-1340.

(47) Eaton, S. S.; More, K. M.; Swant, B. M.; Eaton, G. R. Use of the EPR Half-Field Transition to Determine the Interspin Distance and the Orientation of the Interspin Vector in Systems with Two Unpaired Electrons. *J. Am. Chem. Soc.* **1983**, *105*, 6560-6567.

(48) Borbat, P. P.; Freed, J. H. In *Distance Measurements in Biological Systems by EPR*; Kluwer Academic/Plenum Publisher, New York, 2000; Vol. 19, Chapter 9.

(49) Becker, J. S.; Saxena, S. Double quantum coherence electron spin resonance on coupled Cu(II)–Cu(II) electron spins. *Chem. Phys. Lett.* **2005**, *414*, 248-252.

(50) Eaton, S. S.; Eaton, G. R. In *Distance Measurements in Biological Systems by EPR*; Berliner, L. J., Eaton, S. S., Eaton, G. R., Eds.; Kluwer Academic/Plenum Publisher: New York, 2000; Vol. 19; pp 19-154.

(51) Jeschke, G.; Panek, G.; Godt, A.; Bender, A.; Paulsen, H. Data analysis procedures for pulse ELDOR measurements of broad distance distributions. *Appl. Magn. Reson.* **2004**, *26*, 223-244.

(52) Chiang, Y.-W.; Borbat, P. P.; Freed, J. H. The Determination of Pair Distance Distributions by Pulsed ESR Using Tikhonov Regularization. *J. Magn. Reson.* **2005**, *172*, 279-295.

(53) Hubbell, W. L.; Altenbach, C. Investigation of structure and dynamics in membrane proteins using site-directed spin labeling. *Curr. Opin. Struct. Biol.* **1994**, *4*, 566-573.

(54) Polyhach, Y.; Bordignon, E.; Jeschke, G. Rotamer Libraries of Spin Labelled Cysteines for Protein Studies. *Phys. Chem. Chem. Phys.* **2011**, *13*, 2356-2366.

(55) Hatmal, M. M.; Li, Y.; Hegde, B. G.; Hegde, P. B.; Jao, C. C.; Langen, R.; Haworth, I. S. Computer Modeling of Nitroxide Spin Labels on Proteins. *Biopolymers* **2011**, *97*, 35-44.

(56) Klose, D.; Klare, J. P.; Grohmann, D.; Kay, C. W.; Werner, F.; Steinhoff, H. J. Simulation vs. Reality: A Comparison of in silico Distance predictions with DEER and FRET Measurements. *PLoS ONE* **2012**, *7*, e39492.

(57) Hagelueken, G.; Ward, R.; Naismith, J. H.; Schiemann, O. MtsslWizard: In Silico Spin-Labeling and Generation of Distance Distributions in PyMOL. *Appl. Magn. Reson.* **2012**, *42*, 377-391.

(58) Mamonov, A. B.; Lettieri, S.; Ding, Y.; Sarver, J. L.; Palli, R.; Cunningham, T. F.; Saxena, S.; Zuckerman, D. M. Tunable, Mixed-Resolution Modeling Using Library-Based Monte Carlo and Graphics Processing Units. *J. Chem. Theory Comput.* **2012**, *8*, 2921-2929.

(59) Sarver, J. L.; Townsend, J. E.; Rajapakse, G.; Jen-Jacobson, L.; Saxena, S. Simulating the dynamics and orientations of spin labeled side chains in a protein-DNA complex. *J. Phys. Chem. B* **2012**, *116*, 4024-'4033.

(60) Roux, B.; Islam, S. M. Restrained-Ensemble Molecular Dynamics Simulations Based on Distance Histograms from Double Electron−Electron Resonance Spectroscopy. *J. Phys. Chem. B* **2013**, *117*, 4733-4739.

(61) Cai, Q.; Kusnetzow, A. K.; Hideg, K.; Price, E. A.; Haworth, I. S.; Qin, P. Z. Nanometer Distance Measurements in RNA Using Site-Directed Spin Labeling. *Biophys. J.* **2007**, *93*, 2110-2117.

(62) Malkin, R.; Bearden, A. J. Primary reactions of photosynthesis: photoreduction of a bound chloroplast ferredoxin at low temperature as detected by EPR spectroscopy. *Proc. Natl. Acad. Sci. USA* **1971**, *68*, 16-19.

(63) Bolton, J. R.; Cammack, R. Primary electron acceptor complex of Photosystem I in spinach chloroplasts. *Nature* **1975**, *256*, 668-670.

(64) Rouault, T. A.; Stout, C. D.; Kapatin, S.; Harford, J. B.; Klausner, R. D. Structural relationship between an iron-regulated RNA-binding protein (IRE-BP) and aconitase: functional implications. *Cell* **1991**, *64*, 881-883.

(65) Hentze, M. W.; Argos, P. Homology between IRE-BP, a regulatory RNA-binding protein, aconitase, and isopropylmalate isomerase. *Nucleic Acids Res.* **1991**, *19*, 1739-1740.

(66) Enemark, J. H.; Young, C. G. Bioinorganic chemistry of protein-containing molybdenum and tungsten enzymes. *Adv. Inorg. Chem.* **1993**, *40*, 1-88.

(67) Reczkowski, R. S.; Ash, D. E. EPR evidence for binuclear manganese(II) centers in rat liver arginase. *J. Am. Chem. Soc.* **1992**, *114*, 10992-10994.

(68) Khangulov, S. V.; Pessiki, P. J.; Barynin, V. V.; Ash, D. E.; Dismukes, G. C. Determination of the metal ion separation and energies of the three lowest electronic states of dimanganese(II,II) complexes and enzymes: Catalase and liver Arginase. *Biochemistry* **1995**, *34*, 2015-2025.

(69) Shi, O.; Morris, S. M., Jr.; Zoghbi, H.; Porter, C. W.; O'Brien, W. E. Generation of a mouse model for Arginase II deficiency by targeted disruption of the Arginase II gene *Mol. Cell. Biol.* **2001**, *21*, 811-813.

(70) Lovell, M. A.; Robertson, J. D.; Teesdale, W. J.; Campbell, J. L.; Markesbery, W. R. Copper, iron and zinc in Alzheimer's disease senile plaques. *J. Neurol. Sci.* **1998**, *158*, 47-52.

(71) Huang, X.; Cuajungco, M.; Atwood, C. G.; Hartshorn, M. A.; Tyndall, J. D. A.; Hanson, G. R.; Stokes, K. C.; Leopold, M.; Multhaup, G.; Goldstein, L. E.; Scarpa, R. C.; Saunders, A. J.; Lom, J.; Moir, R. D.; Glabe, C.; Bowden, E. F.; Masters, C. L.; Fairlie, D. P.; Tanzi, R. E.; Bush, A. I. Cu(II) potentiation of Alzhermer Aβ neurotoxicity. *J. Biol. Chem.* **1999**, *274*, 37111-37116.

(72) Bush, A. I. Metal complexing agents and therapies for Alzheimer's disease. *Neurobiol. Aging* **2002**, *23*, 1031-1038.

(73) Kirkitadze, M. D.; Bitan, G.; Teplow, D. B. Paradigm shifts in Alzhermer's disease and other neurodegenerative disorders: The emerging role of oligomeric assemblies. *J. Neurosci. Res.* **2002**, *69*, 567-577.

(74) Miller, L. M.; Wang, Q.; Telivala, T. P.; Smith, R. J.; Lanzirotti, A.; Miklossy, J. Synchrotron-based infrared and X-ray imaging shows focalized accumulation of Cu and Zn co-localized with β-Amyloid deposits in Alzheimer's disease. *J. Struct. Biol.* **2006**, *155*, 30-37.

(75) Waldron, K. J.; Rutherford, J. C.; Ford, D.; Robinson, N. J. Metalloproteins and Metal Sensing. *Nature* **2009**, *460*, 823-830.

(76) van Amsterdam, I. M. C.; Ubbink, M.; Canters, G. W.; Huber, M. Measurement of a Cu-Cu distance of 26 A by a pulsed EPR method. *Angew. Chem. Int. Ed. Engl.* **2003**, *42*, 62-64.

(77) Narr, E.; Godt, A.; Jeschke, G. Selective measurements of a nitroxide-nitroxide separation of 5 nm and a nitroxide-copper separation of 2.5 nm in a terpyridine-based copper(II) complex by pulse EPR spectroscopy. *Angew. Chem. Int. Ed. Engl.* **2002**, *41*, 3907-3910.

(78) Kay, C. W. M.; Mkami, H. E.; Cammack, R.; Evans, R. W. Pulsed ELDOR determination of the intramolecular distance between the metal binding sites in dicupric human serum transferrin and lactoferrin. *J. Am. Chem. Soc.* **2007**, *129*, 4868-4869.

(79) Bode, B. E.; Plackmeyer, J.; Prisner, T. F.; Schiemann, O. PELDOR measurements on a nitroxide-labeled Cu(II) porphyrin: orientation selection, spin-density distribution, and conformational flexibility. *J. Phys. Chem. A* **2008**, *112*, 5064-5073.

(80) Bode, B. E.; Plackmeyer, J.; Bolte, M.; Prisner, T. F.; Schiemann, O. PELDOR on An Exchange Coupled Nitroxide Copper(II) Spin Pair. *J. Organomet. Chem.* **2009**, *694*, 1172-1179.

(81) Yang, Z.; Kise, D.; Saxena, S. An approach towards the measurement of nanometer range distances based on Cu^{2+} ions and ESR. *J. Phys. Chem. B* **2010**, *114*, 6165-6174.

(82) van Wonderen, J.; Kostrz, D. N.; Dennison, C.; MacMillan, F. Refined Distances Between Paramagnetic Centers of a Multi-Copper Nitrite Reductase Determined by Pulsed EPR (iDEER) Spectroscopy. *Angew. Chem. Int. Ed. Engl.* **2013**, *52*, 1990-1993.

(83) Elsaesser, C.; Brecht, M.; Bittl, R. Pulsed electron-electron double resonance on multinuclear metal clusters:Assignment of spin projection factors based on the dipolar interaction. *J. Am. Chem. Soc.* **2002**, *124*, 12606-12611.

(84) Elsaesser, C.; Brecht, M.; Bittl, R. Treatment of spin-coupled metal centres in pulsed electron-electron double-resonance experiments. *Biochem. Soc. Trans.* **2005**, *33*, 15-19.

(85) Roessler, M. M.; King, M. S.; Robinson, A. J.; Armstrong, F. A.; Harmer, J.; Hirst, J. Direct Assignment of EPR Spectra to Structurally Defined Iron-Sulfur Clusters in Complex I by Double Electron–Electron Resonance *Proc. Natl. Acad. Sci. USA* **2010**, *107*, 1930-1935.

(86) Raitsimring, A. M.; Gunanathan, C.; Potapov, A.; Efremenko, I.; Martin, J. M.; Milstein, D.; Goldfarb, D. Gd^{3+} complexes as potential spin labels for high field pulsed EPR distance measurements. *J. Am. Chem. Soc.* **2007**, *129*, 14138-14139.

(87) Lueders, P.; Jeschke, G.; Yulikov, M. Double electron-electron resonance measured between Gd^{3+} ions and nitroxide radicals. *J. Phys. Chem. Lett.* **2011**, *2*, 604-609.

(88) Kaminker, I.; Yagi, H.; Huber, T.; Feintuch, A.; Otting, G.; Goldfarb, D. Spectroscopic selection of distance measurements in a protein dimer with mixed nitroxide and Gd^{3+} spin labels. *Phys. Chem. Chem. Phys.* **2012**, *14*, 4355-4358.

(89) Potapov, A.; Yagi, H.; Huber, T.; Jergic, S.; Dixon, N. E.; Otting, G.; Goldfarb, D. Nanometer-scale distance measurements in proteins using Gd^{3+} spin labeling. *J. Am. Chem. Soc.* **2010**, *132*, 9040-9048.

(90) Song, Y.; Meade, T. J.; Astashkin, A. V.; Klein, E. L.; Enemark, J. H.; Raitsimring, A. Pulsed dipolar spectroscopy distance measurements in biomacromolecules labeled with Gd(III) markers. *J. Magn. Reson.* **2011**, *210*, 59-68.

(91) Potapov, A.; Song, Y.; Meade, T. J.; Goldfarb, D.; Astashkin, A. V.; Raitsimring, A. Distance Measurements in Model Bis-Gd(III) Complexes with Flexible "bridge". Emulation of Biological Molecules having Flexible Structure with Gd(III) Labels Attached. *J. Magn. Reson.* **2010**, *205*, 38-49.

(92) Yagi, H.; Banerjee, D.; Graham, B.; Huber, T.; Goldfarb, D.; Otting, G. Gadolinium Tagging for High-Precision Measurements of 6 nm Distances in Protein Assemblies by EPR. *J. Am. Chem. Soc.* **2011**, *133*, 10418-10421.

(93) Kaminker, I.; Tkach, I.; Manukovsky, N.; Huber, T.; Yagi, H.; Otting, G.; Bennati, M.; Goldfarb, D. W-band Orientation Selective DEER Measurements on a Gd^{3+}/Nitroxide Mixed-Labeled Protein Dimer with a Dual Mode Cavity. *J. Magn. Reson.* **2013**, *227*, 66-71.

(94) Yulikov, M.; Lueders, P.; Warsi, M. F.; Chechik, V.; Jeschke, G. Distance Measurements in Au Nanoparticles Functionalized with Nitroxide Radicals and Gd^{3+}–DTPA Chelate Complexes. *Phys. Chem. Chem. Phys.* **2012**, *14*, 10732-10746.

(95) Matalon, E.; Huber, T.; Hagelueken, G.; Graham, B.; Frydman, V.; Feintuch, A.; Otting, G.; Goldfarb, D. Gadolinium(III) Spin Labels for High-Sensitivity Distance Measurements in Transmembrane Helices. *Angew. Chem. Int. Ed. Engl.* **2013**, *52*, 1-5.

(96) Banerjee, D.; Yagi, H.; Huber, T.; Otting, G.; Goldfarb, D. Nanometer-range distance measurement in a protein using Mn^{2+} tags. *J. Phys. Chem. Lett.* **2012**, *3*, 157-160.

(97) Goldfarb, D. *Metal-Based Spin Labeling for Distance Determination*; Springer Berlin Heidelberg, 2012.

(98) Maryasov, A. G.; Tsvetkov, Y. D.; Raap, J. Weakly coupled radical pairs in solids: ELDOR in ESE structure studies. *Appl. Magn. Reson.* **1998**, *14*, 101-113.

(99) Milov, A. D.; Tsvetkov, Y. D.; Formaggio, F.; Crisma, M.; Toniolo, C.; Raap, J. The Secondary Structure of a Membrane-Modifying Peptide in a Supramolecular Assembly Studied by PELDOR and CW-ESR Spectroscopies. *J. Am. Chem. Soc.* **2001**, *123*, 3784-3789.

(100) Salikhov, K. M.; Dzuba, S. A.; Raitsimring, A. M. The theory of electron spin-echo signal decay resulting from dipole-dipole interactions between paramagnetic centers in solids. *J. Magn. Reson.* **1981**, *42*, 255-276.

(101) Jeschke, G.; Polyhach, Y. Distance measurements on spin-labelled biomacromolecules by pulsed electron paramagnetic resonance. *Phys. Chem. Chem. Phys.* **2007**, *9*, 1895-1910.

(102) Yang, Z.; Ji, M.; Saxena, S. Practical Aspects of copper-ion based DEER distance measurements. *Appl. Magn. Reson.* **2010**, *39*, 487-500.

(103) Ruthstein, S.; Ji, M.; Mehta, P.; Jen-Jacobson, L.; Saxena, S. Sensitive Cu^{2+}-Cu^{2+} Distance Measurements in A Protein-DNA Complex by DQC-ESR. *J. Phys. Chem. B* **2013**, *117*, 6227-6230.

(104) Yang, Z.; Becker, J.; Saxena, S. On Cu(II)–Cu(II) distance measurements using pulsed electron electron double resonance. *J. Magn. Reson.* **2007**, *188*, 337-343.

(105) Lovett, J. E.; Bowen, A. M.; Timmel, C. R.; Jones, M. W.; Dilworth, J. R.; Caprotti, D.; Bell, S. G.; Wong, L. L.; Harmer, J. Structural information from orientationally selective DEER spectroscopy. *Phys. Chem. Chem. Phys.* **2009**, *11*, 6840-6848.

(106) Godt, A.; Schulte, M.; Zimmermann, H.; Jeschke, G. How flexible are poly(paraphenyleneethynylene)s? *Angew. Chem. Int. Ed. Engl.* **2006**, *45*, 7560-7564.

(107) Kaminker, I.; Florent, M.; Epel, B.; Goldfarb, D. Simultaneous acquisition of pulse EPR orientation selective spectra *J. Magn. Reson.* **2011**, *208*, 95-102.

(108) Marko, A.; Margraf, D.; Yu, H.; Mu, Y.; Stock, G.; Prisner, T. F. Molecular orientation studies by pulsed electron-electron double resonance experiments. *J. Chem. Phys.* **2009**, *130*, 064102-1-064102-9.

(109) Woodhead, J. L.; Bhave, N.; Malcolm, A. D. B. Cation dependence of restriction endonuclease EcoRI activity. *Eur. J. Biochem.* **1981**, *115*, 293-296.

(110) Grigorescu, A.; Horvath, M.; Wilkosz, P.; Chandrasekhar, K.; Rosenberg, J. In *Restriction Endonucleases*; Springer-Verlag, Heidelberg, 2004; pp 137-177.

(111) Kurpiewski, M. R.; Engler, L. E.; Wozniak, L. A.; Kobylanska, A.; Koziolkiewicz, M.; Stec, W. J.; Jen-Jacobson, L. Mechanism of coupling between DNA recognition specificity and catalysis in EcoRI endonuclease. *Structure* **2004**, *12*, 1775-1788.

(112) Jeschke, G.; Chechik, V.; Ionita, P.; Godt, A.; Zimmermann, H.; Banham, J.; Timmel, C. R.; Hilger, D.; Jung, H. DeerAnalysis2006—a comprehensive software package for analyzing pulsed ELDOR data. *Appl. Magn. Reson.* **2006**, *30*, 473-498.

(113) Sengupta, I.; Nadaud, P. S.; Jaroniec, C. P. Protein Structure Determination with Paramagnetic Solid-State NMR Spectroscopy. *Acc. Chem. Res.* **2013**, *46*, 2117-2126.

(114) Lesser, D. R.; Kurpiewski, M. R.; Jen-Jacobson, L. The energetic basis of specificity in the Eco RI endonuclease-DNA interaction. *Science* **1990**, *250*, 776-786.

(115) Pingoud, A.; Fuxreiter, M.; Pingoud, V.; Wende, W. Type II restriction endonucleases: structure and mechanism. *Cell Mol. Life Sci.* **2005**, *62*, 685-707.

(116) Sapienza, P. J.; dela Torre, C. A.; H., M. W.; Jana, S. V.; Jen-Jacobson, L. Thermodynamic and kinetic basis for the relaxed DNA sequence specificity of "promiscuous" mutant EcoRI endonucleases. *J. Mol. Biol.* **2005**, *348*, 307-324.

(117) Vipond, I. B.; Baldwin, G. S.; Halford, S. E. Divalent metal ions at the active sites of the EcoRV and EcoRI restriction endonucleases. *Biochemistry* **1995**, *34*, 697-704.

(118) Pingoud, V.; Wende, W.; Friedhoff, P.; Reuter, M.; Alves, J.; Jeltsch, A.; Mones, L.; Fuxreiter, M.; Pingoud, A. On the Divalent Metal Ion Dependence of DNA Cleavage by Restriction Endonucleases of the EcoRI Family. *J. Mol. Biol.* **2009**, *393*, 140-160.

(119) Shannon, R. D. Revised Effective Ionic Radii and Systematic Studies of Interatomic Distances in Halides and Chalcogenides. *Acta Cryst.* **1976**, *A32*, 751-767.

(120) Heitman, J.; Zinder, N. D.; Model, P. Repair of the *Esche-richia coli* Chromosome after *in vivo* Scission by the EcoRI endonuclease *Proc. Natl. Acad. Sci. USA* **1989**, *86*, 2281-2285.

(121) Fauth, J.-M.; Schweiger, A.; Braunschweiler, L.; Forrer, J.; Ernst, R. R. Elimination of Unwanted Echoes and Reduction of Dead Time in Three-Pulse Electron Spin-Echo Spectroscop. *J. Magn. Reson.* **1986**, *66*, 74-85.

(122) Gemperle, C.; Aebli, G.; Schweiger, A.; Ernst, R. R. Phase Cycling in Pulse EPR. *J. Magn. Reson.* **1990**, *88*, 241-256.

(123) Gullingsrud, J.; Saam, J.; J. Phillips, e. *psfgen User's Guide*; Theoretical and Computational Biophysics Group, University of Illinois and Beckman Institute, 2011.

(124) A. D. Mackerell, J.; Feig, M.; Brooks, C. L. Extending the treatment of backbone energetics in protein force fields: Limitations of gas-phase quantum mechanics in reproducing protein conformational distributions in molecular dynamics simulations. *J. Comput. Chem.* **2004**, *25*, 1400-1415.

(125) Foloppe, N.; A. D. MacKerell, J. All-atom empirical force field for nucleic acids: I. Parameter optimization based on small molecule and condensed phase macromolecular target data. *J. Comput. Chem.* **2000**, *21*, 86-104.

(126) A. D. MacKerell, J.; Banavali, N. K. All-atom empirical force field for nucleic acids: II. Application to molecular dynamics simulations of DNA and RNA in solution. *J. Comput. Chem.* **2000**, *21*, 105-120.

(127) Jorgensen, W. L. Quantum and statistical mechanical studies of liquids. 10. Transferable intermolecular potential functions for water, alcohols, and ethers. Application to liquid water. *J. Am. Chem. Soc.* **1981**, *103*, 335-340.

(128) Ryckaert, J.-P.; Ciccotti, G.; Berendsen, H. J. C. Numerical integration of the Cartesian equations of motion of a system with constraints: molecular dynamics of n-Alkanes. *J. Comput. Phys.* **1977**, *23*, 327-341.

(129) de Leeuw, S. W.; Perram, J. W.; Smith, E. R. Simulation of electrostatic systems in periodic boundary conditions. I. Lattice sums and dielectric constants. *Proc. R. Soc. Lond. A* **1980**, *373*, 27-56.

(130) Phillips, J. C.; Braun, R.; Wang, W.; Gumbart, J.; Tajkhorshid, E.; Villa, E.; Chipot, C.; Skeel, R. D.; Kale, L.; Schulten, K. Scalable molecular dynamics with NAMD. *J. Comput. Chem.* **2005**, *26*, 1781-1802.

(131) Rocchia, W.; Alexov, E.; Honig, B. Extending the applicability of the nonlinear poisson−boltzmann equation:□Multiple dielectric constants and multivalent Ions. *J Phys Chem B* **2001**, *105*, 6507-6514.

(132) Rocchia, W.; Sridharan, S.; Nicholls, A.; Alexov, E.; Chiabrera, A.; Honig, B. Rapid grid-based construction of the molecular surface and the use of induced surface charge to calculate reaction field energies: applications to the molecular systems and geometric objects. *J Comput Chem* **2002**, *23*, 128-137.

(133) Fogolari, F.; Brigo, A.; Molinari, H. The Poisson-Boltzmann Equation for Biomolecular Eletrostatics: A Tool for structural Biology. *J. Mol. Recognit.* **2002**, *15*, 377-392.

(134) DeLano, W. L. T. The PyMOL molecular graphics system. DeLano Scientific, San Carlos, CA, USA**2002**.

(135) Bertini, I.; Canti, G.; Grassi, R.; Scozzafava, A. Effects of Planar and Tetrahedral Distortions on the ESR Parameters of Bis(salicylaldiminato)copper(II) Complexes. *Inorg. Chem.* **1980**, *19*, 2198-2200.

(136) Singh, V.; Zhu, Z.; Davidson, V. L.; McCracken, J. Characterization of the Tryptophan Tryptophyl-Semiquinone Catalytic Intermediate of Methylamine Dehydrogenase by Electron Spin-Echo Envelope Modulation Spectroscopy. *J. Am. Chem. Soc.* **2000**, *122*, 931-938.

(137) Yang, Z. Copper Ion-Based Electron Spin Resonance Spectroscopic Rulers. Ph.D. Thesis, University of Pittsburgh, 2010.

(138) Hancock, S. P.; Hiller, D. A.; Perona, J. J.; Jen-Jacobson, L. The Energetic Contribution of Induced Electrostatic Asymmetry to DNA Bending by a Site-Specific Protein. *J. Mol. Biol.* **2011**, *406*, 285-312.

(139) Engler, L. E.; Sapienza, P.; Dorner, L. F.; Kucera, R.; Schildkraut, I.; Jen-Jacobson, L. The Energetics of the Interaction of BamHI Endonuclease with Its Recognition Site GGATCC. *J. Mol. Biol.* **2001**, *307*, 619-636.

(140) Sapienza, P. J.; dela Torre, C. A.; McCoy IV, W. H.; Jana, S. V.; Jen-Jacobson, L. Thermodynamic and kinetic basis for the relaxed DNA sequence specificity of "Promiscuous" mutant EcoRI endonucleases. *J Mol Biol* **2005**, *348*, 307-324.

(141) Mesu, J. G.; Visser, T.; Soulimani, F.; van Faassen, E. E.; de Peinder, P.; Beale, A. M.; Weckhuysen, B. M. New Insights into the Coordination Chemistry and Molecular Structure of Copper(II) Histidine Complexes in Aqueous Solutions. *Inorg. Chem.* **2006**, *45*, 1960-1971.

(142) Bruice, T. C.; Benkovic, S. J. Chemical Basis for Enzyme Catalysis. *Biochemistry* **2000**, *39*, 6267-6274.

(143) Warshela, A.; Russell, S. T. Calculations of electrostatic interactions in biological systems and in solutions. *Q. Rev. Biophys.* **1984**, *17*, 283-422.

(144) Matthew, J. B. Electrostatic effects in proteins. *Annu. Rev. Biophys. Biophys. Chem.* **1985**, *14*, 387-417.

(145) Honig, B. H.; Hubbell, W. L.; Flewelling, R. F. Electrostatic interactions in membranes and proteins. *Annu. Rev. Biophys. Biophys. Chem.* **1986**, *15*, 163-193.

(146) Chin, K.; Sharp, K. A.; Honig, B.; Pyle, A. M. Calculating the electrostatic properties of RNA provides new insights into molecular interactions and function. *Nat Struct Biol* **1999**, *6*, 1055-1061.

(147) Pingoud, A.; Jeltsch, A. Recognition and Cleavage of DNA by Type-II Restriction Endonucleases. *Eur. J. Biochem.* **1997**, *246*, 1-22.

(148) Dylla-Spears, R.; Townsend, J. E.; Sohn, L. L.; Jen-Jacobson, L.; Muller, S. J. Fluorescent Marker for Direct Detection of Specific dsDNA Sequences. *Anal. Chem.* **2009**, *81*, 10049-10054.

(149) Ruthstein, S.; Stone, K. M.; Cunningham, T. F.; Ji, M.; Cascio, M.; Saxena, S. Pulsed Electron Spin Resonance Resolves the Coordination Site of Cu^{2+} Ions in α1-Glycine Receptor. *Biophysical Journal* **2010**, *99*, 2497-2506.

(150) Colaneri, M. J.; Vitali, J.; Peisach, J. Electron Spin-Echo Envelope Modulation Study of Multicrystalline Cu^{2+}-Insulin: Effects of Cd^{2+} on the Nuclear Quadrupole Interaction of the Cu^{2+}-Coordinated Imidazole Remote Nitrogen. *Biochemistry* **2000**, *39*, 584-591.

(151) Athertona, N. M.; Horsewilla, A. J. Proton ENDOR of $Cu(H_2O)_6^{2+}$ in $Mg(NH_4)_2(SO_2)_4$•$6H_2O$. *Mol. Phys.* **1979**, *37*, 1349-1361.

(152) Kim, D.; Kim, N. H.; Kim, S. H. 34 GHz Pulsed ENDOR Characterization of the Copper Coordination of an Amyloid b Peptide Relevant to Alzheimer's Disease. *Angew. Chem. Int. Ed. Engl.* **2013**, *52*, 1139-1142.

(153) Zhang, J.; Carl, P. J.; Zimmermann, H.; Goldfarb, D. Investigation of the Formation of MCM-41 by Electron Spin-Echo Envelope Modulation Spectroscopy. *J. Phys. Chem. B* **2002**, *106*, 5382-5389.

(154) Magliozzo, R. S.; Bubacco, L.; McCracken, J.; Jiang, F.; Beltramini, M.; Salvato, B.; Peisach, J. Cu(II) Coordination in Arthropod and Mollusk Green Half-Methemocyanins Analyzed by Electron Spin-Echo Envelope Modulation Spectroscopy. *Biochemistry* **1995**, *34*, 1513-1523.

(155) Cornelius, J. B.; McCracken, J.; Clarkson, R. B.; Belford, R. L.; Peisach, J. Electron Spin Echo Envelope Modulation Angle Selection Studies of Axial Pyridine Coordination to Copper(II) Benzoylacetonate. *J. Phys. Chem.* **1990**, *94*, 6977-6982.

(156) Rubino, J. T.; Franz, K. J. Coordination Chemistry of Copper Proteins: How Nature Handles a Toxic Cargo for Essential Function. *J. Inorg. Biochem.* **2012**, *107*, 129-143.

(157) Freed, J. H. New technologies in electron spin resonance. *Annu. Rev. Phys. Chem.* **2000**, *51*, 655-689.

(158) Park, S.-Y.; Borbat, P. P.; Gonzalez-Bonet, G.; Bhatnagar, J.; Pollard, A. M.; Freed, J. H.; Bilwes, A. M.; Crane, B. R. Reconstruction of the chemotaxis receptor–kinase assembly. *Nat. Struct. Mol. Bio.* **2006**, *13*, 400-407.

(159) Altenbach, C.; Kusnetzow, A. K.; Ernst, O. P.; Hofmann, K. P.; Hubbell, W. L. From the Cover: High-resolution distance mapping in rhodopsin reveals the pattern of helix movement due to activation. *Proc. Natl. Acad. Sci. USA* **2008**, *105*, 7439-7444.

(160) Bleicken, S.; Classen, M.; Padmavathi, P. V. L.; Ishikawa, T.; Zeth, K.; Steinhoff, H.-J.; Bordignon, E. Protein Structure and Folding. *J. Biol. Chem.* **2010**, *285*, 6636-6647.

(161) Dockter, C.; Volkov, A.; Bauer, C.; Polyhach, Y.; Joly-Lopez, Z.; Jeschke, G.; Paulsen, H. Refolding of the integral membrane protein light-harvesting complex II monitored by pulse EPR. *Proc. Natl. Acad. Sci. USA* **2009**, *106*, 18485-18490.

(162) Kear, J. L.; Blackburn, M. E.; Veloro, A. M.; Dunn, B. M.; Fanucci, G. E. Subtype Polymorphisms Among HIV-1 Protease Variants Confer Altered Flap Conformations and Flexibility. *J. Am. Chem. Soc.* **2009**, *131*, 14650-14651.

(163) Sugata, K.; Song, L.; Nakamura, M.; Ueki, S.; Fajer, P. G.; Arata, T. Nucleotide-Induced Flexibility Change in Neck Linkers of Dimeric Kinesin as Detected by Distance Measurements Using Spin-Labeling EPR. *J. Mol. Biol.* **2009**, *386*, 626-636.

(164) Zou, P.; Bortolus, M.; Mchaourab, H. S. Conformational Cycle of the ABC Transporter MsbA in Liposomes: Detailed Analysis Using Double Electron–Electron Resonance Spectroscopy. *J. Mol. Biol.* **2009**, *393*, 586-597.

(165) Elsässer, C.; Brecht, M.; Bittl, R. Pulsed electron-electron double resonance on multinuclear metal clusters:Assignment of spin projection factors based on the dipolar interaction. *J. Am. Chem. Soc.* **2002**, *124*, 12606-12611.

(166) Gordon-Grossman, M.; Kaminker, I.; Gofman, Y.; Shai, Y.; Goldfarb, D. W-Band pulse EPR distance measurements in peptides using Gd3+-dipicolinic acid derivatives as spin labels. *Phys. Chem. Chem. Phys.* **2011**, *13*, 10771-10780.

(167) Kim, Y. C.; Grable, J. C.; Love, R.; Greene, P. J.; Rosenberg, J. M. Refinement of Eco RI endonuclease crystal structure: a revised protein chain tracing. *Science* **1990**, *249*, 1307-1309.

(168) Misra, S. K.; Borbat, P. P.; Freed, J. H. Calculation of Double-Quantum-Coherence Two-dimensional Spectra: Distance Measurements and Orientational Correlations. *Appl. Magn. Reson.* **2009**, *36*, 237-258.